THESIS FOR THE DEGREE OF DOCTOR OF PHILOSOPHY

Optics for Earth Observation Instruments

ARVID HAMMAR

Terahertz and Millimetre Wave Laboratory
Department of Microtechnology and Nanoscience - MC2
CHALMERS UNIVERSITY OF TECHNOLOGY
Gothenburg, Sweden 2019

Optics for Earth Observation Instruments
ARVID HAMMAR
orcid.org/0000-0001-5576-2553

ISBN: 978-91-7905-102-0

Series number: 4569
in the series Doktorsavhandlingar vid Chalmers tekniska högskola.
Ny serie (ISSN0346-718X)

Technical Report MC2-408
ISSN 1652-0769

Chalmers University of Technology
Department of Microtechnology and Nanoscience - MC2
Terahertz and Millimetre Wave Laboratory
SE-412 96 Gothenburg, Sweden
Phone: +46 (0)31-772 10 00

Front cover image: First light of the MATS limb instrument breadboard model. Light from a USAF 1951 target was projected onto a sticky note before installing a proper image sensor.

Printed by Reproservice, Chalmers
Gothenburg, Sweden, March 2019

Abstract

The optical system is an essential part of every remote sensing instrument used for detecting electromagnetic waves. Careful design, fabrication and characterization is therefore crucial, especially for satellite-borne missions where the possibility of post-launch repairs is highly limited. This thesis presents contributions to a new type of reflector optics and horn antennas for three instruments for Earth observation, which operate at wavelengths between the UV and millimeter-wave regions: Mesospheric Airglow/Aerosol Tomography Spectroscopy (MATS), International Submillimetre Airborne Radiometer (ISMAR) and Stratosphere-Troposphere Exchange And climate Monitor Radiometer (STEAMR).

A free-form three-mirror off-axis telescope was developed for the limb instrument on board the MATS satellite. The $f/7.3$ (D = 35 mm) design achieved diffraction-limited performance (at 270-772 nm) over a wide field ($5.67° \times 0.91°$) by applying a new design method that corrects for linear astigmatism. Single point diamond turning was used to fabricate the free-form mirrors, which resulted in a telescope with a modulation transfer function of 0.45 at 20 lp/mm. Simulations and measurements were used to assess stray light rejection of the limb instrument. Measurements of a breadboard front baffle with a new type of extremely black coating showed a point source transmittance down to 10^{-6}, which was in excellent agreement with simulations. Detailed modeling predicted a stray light rejection of 10^{-10}-10^{-4} in the most critical region below the nominal field of view.

Two 874 GHz Schottky mixer receivers with integrated low noise amplifiers, spline horns and low-loss dielectric lenses were developed for ISMAR, which exhibited record-low receiver noise temperatures of 2260-2770 K. Radiation patterns were measured between 868.7-880.0 GHz in a setup capable of resolving side lobes down to 25-30 dB below the main peak. The main beam full-width-half-maximum was in good agreement with simulations and well below the required 5°. Spline horn antennas at frequencies 120-340 GHz were also developed. An efficient optimization algorithm based on mode matching in circular waveguides was used for all designs, which exhibited Gaussicity values of 98% over bandwidths up to 19%. Far field radiation patterns were measured using a setup for spherical and planar scanning geometries.

A mechanical tolerance analysis was performed for the optical system of STEAMR, which consists of two polarization-separated focal plane arrays, a four-reflector anastigmatic relay optics chain and an off-axis Ritchey-Chretien telescope. Using Monte-Carlo simulations based on ray-tracing and physical optics, an overall reflector alignment accuracy requirement of 100 µm was obtained. Surface distortion analyses of the 1.6 m × 0.8 m primary reflector highlighted the need for an optical system with small mechanical variations in orbit (< 30 µm). A relay optics demonstrator showed that alignment accuracies down to 50 µm could be obtained.

In conclusion, the methods for design, manufacturing and characterization presented in this thesis can be used to develop new instruments for Earth observation and related fields.

Keywords: reflector optics, off-axis, spline horns, telescopes, scientific instruments, measurements, free-form mirrors, satellites, THz, stray light, tolerancing, diamond turning.

List of publications

This thesis is based on the following papers:

[A] **A. Hammar**, W. Park, S. Chang, S. Pak, A. Emrich and J. Stake, ”Wide-field off-axis telescope for the Mesospheric Airglow/Aerosol Tomography Spectroscopy satellite,” in *OSA Applied Optics*, Vol. 58, No. 6, pp. 1393-1399, January 2019. DOI: 10.1364/AO.58.001393

[B] **A. Hammar**, O.M. Christensen, W. Park, S. Pak, A. Emrich and J. Stake, ”Stray Light Suppression of a Compact Off-Axis Telescope for a Satellite-Borne Instrument for Atmospheric Research,” in *SPIE/COS Photonics Asia*, Optical Design and Testing VIII, Vol. 10815, p. 108150F, Beijing, China, October 2018. DOI: 10.1117/12.2500555

[C] **A. Hammar**, P. Sobis, V. Drakinskiy, A. Emrich, N. Wadefalk, J. Schleeh and J. Stake, ”Low noise 874 GHz receivers for the international submillimetre airborne radiometer (ISMAR),” in *AIP Review of Scientific Instruments*, Vol. 89, No. 5, 055104, May 2018. DOI: 10.1063/1.5017583

[D] Y. Karandikar, **A. Hammar**, P. Sobis, P. Forsberg, A. Emrich and J. Stake, ”A 874 GHz mixer block integrated spline horn and lens antenna for the ISMAR instrument,” in *9th European Conference on Antennas and Propagation (EuCAP), 2015*, pp. 1-5, Lisbon, Portugal, May 2015.

[E] **A. Hammar**, N. Nyberg, Y. Karandikar, P. Sobis, O. Tropp, P. Forsberg, S. McCallion, A. Emrich and J. Stake, ”THz Smooth-Walled Spline Horn Antennas: Design, Manufacturing and Measurements,” in *IEEE International Symposium on Antennas and Propagation (APSURSI)*, pp. 1341-1342, Fajardo, Puerto Rico, June-July 2016. DOI: 10.1109/APS.2016.7696378

[F] **A. Hammar**, M. Whale, P. Forsberg, A. Murk, A. Emrich and J. Stake, ”Optical Tolerance Analysis of the Multi-Beam Limb Viewing Instrument STEAMR,” in *IEEE Transactions on Terahertz Science and Technology,* vol. 4, no 6, pp. 714-721, November 2014. DOI: 10.1109/TTHZ.2014.2361616

The following papers are not included since the content overlaps or is beyond the scope of this thesis:

[a] **A. Hammar**, S. Cherednichenko, S. Bevilacqua, V. Drakinskiy and J. Stake, "Terahertz Direct Detection in $YBa_2Cu_3O_7$ Microbolometers," in *IEEE Transactions on Terahertz Science and Technology,* vol. 1, no. 2, pp. 390-394, November 2011. DOI: 10.1109/TTHZ.2011.2161050

[b] S. Cherednichenko, **A. Hammar**, S. Bevilacqua, V. Drakinskiy, J. Stake and A. Kalabukhov, "A Room Temperature Bolometer for Terahertz Coherent and Incoherent Detection," in *IEEE Transactions on Terahertz Science and Technology,*, vol. 1, no. 2, pp. 395-402, November 2011. DOI: 10.1109/TTHZ.2011.2164654

[c] **A. Hammar**, P. Sobis, V. Drakinskiy, H. Zhao, A. Emrich and J. Stake, "A 600 GHz Orthomode Transducer based on a Waveguide Integrated Wire Grid Polarizer," *23rd International Symposium on Space and Terahertz Technology*, Tokyo, Japan, April 2012

[d] **A. Hammar**, P. Forsberg, A. Emrich, M. Whale, A. Murk and J. Stake, "Optical Tolerance Analysis for the STEAMR Instrument," in *24th International Symposium on Space and Terahertz Technology*, Groningen, the Netherlands, April 2013

[e] J. Gumbel, L. Megner, O.M. Christensen, S. Chang, J. Dillner, T. Ekebrand, G. Giono, **A. Hammar**, J. Hedin, N. Ivchenko, B. Karlsson, M. Krus, A. Li, S. McCallion, D.P. Murtagh, G.Olentsenko, S. Pak, W. Park, J. Rouse, J. Stegman, G. Witt, "The MATS Satellite Mission - Gravity Waves Studies by Mesospheric Airglow/Aerosol Tomography and Spectroscopy," in *Atmospheric Chemistry and Physics Discusssions*, December 2018. DOI: 10.5194/acp-2018-1162

[f] P. Sobis, V. Drakinskiy, N. Wadefalk, Y. Karandikhar, **A. Hammar**, A. Emrich, H. Zhao, T. Bryllert, A-T. Tang, P-A. Nilsson, J. Schleeh, H. Kim, K. Jacob, A. Murk, J. Grahn and J. Stake, "Low noise GaAs Schottky TMIC and InP Hemt MMIC based receivers for the ISMAR and SWI instruments," in *Proc. ESAESTEC Micro-and Millimetre Wave Technol. Techn. Workshop*, Noordwijk, the Netherlands, November 2014.

[g] S. Bevilacqua, S. Cherednichenko, V. Drakinskiy, H. Shibata, **A. Hammar** and J. Stake, "Investigation of MgB 2 HEB mixer gain bandwidth," in *36th International Conference on Infrared, Millimeter and Terahertz Waves (IRMMW-THz)*, pp. 1-2, Houston, Texas USA, October 2011. DOI: 10.1109/irmmw-THz.2011.6104835

[h] **A. Hammar**, Y. Karandikar, P. Forsberg, A. Emrich and J. Stake, "A 340 GHz High Gaussicity Smooth Spline Horn Antenna for the STEAMR Instrument," in *IEEE Antennas and Propagation Society International Symposium (APSURSI)*, pp. 649-650, Memphis, USA, July 2014. DOI: 10.1109/APS.2014.6904655

[i] A. Emrich, U. Frisk, P. Sobis, **A. Hammar**, E. Ryman and K. Kempe, ”Radiometer instruments for space applications,” in *39th International Conference on Infrared, Millimeter, and Terahertz waves (IRMMW-THz)*, pp. 1-2, Tucson, Arizona USA, August 2014. DOI: 10.1109/IRMMW-THz.2014.6956007

[j] G. Giono, G. Olentsenko, N. Ivchenko, O.M. Christensen, J. Gumbel, U. Frisk, **A. Hammar**, I. Davies and L. Megner ”Characterisation of the analogue read-out chain for the CCDs onboard the Mesospheric Airglow/Aerosol Tomography and Spectroscopy (MATS),” in *SPIE Space Telescopes and Instrumentation 2018: Optical, Infrared, and Millimeter Wave*, Vol. 10698, p. 106984Y Austin, USA, July 2018. DOI: 10.1117/12.2313732

[k] S. Cherednichenko, **A. Hammar**, S. Bevilacqua, V. Drakinskiy and J. Stake ”Wideband THz detectors based on YBCO thin films at 77K and at room temperature,” in *6th ESA Workshop on Millimetre-Wave Technology and Applications*, Espoo, Finland, August 2011.

[l] **A. Hammar**, A. Emrich, D. McCarthy, A. Murphy, N. Trappe and J. Stake ”Optical Designs for a Multi-Beam 340 and 625/640 GHz Spaceborne Climate Research Instrument,” in *26th International Symposium on Space Terahertz Technology*, Cambridge, USA, March 2015.

Notations and acronyms

λ	wavelength
ν	frequency
σ	RMS surface roughness
ϕ_0	Gouy phase shift
ω	angular frequency
Ω	solid angle
c	speed of light
f	focal length
f_{eff}	effective focal length
h	Planck's constant
k	wavenumber
k_B	the Boltzmann constant
m	magnification
n	refractive index
w	beam width
w_0	beam waist
z_c	confocal distance
f/D	f-number
D	aperture diameter
$\mathbf{E}$	electric field
G	gain
$\mathbf{H}$	magnetic field
I	intensity
P	power
T	temperature
AUT	Antenna Under Test
BRDF	Bidirectional Reflectance Distribution Function
CATR	Compact Antenna Test Range
CCD	Charge Coupled Device
CMM	Coordinate Measuring Machine
DSB	Double sideband
FDTD	Finite-difference time-domain
FEM	Finite Element Method

FFT	Fast Fourier Transform
FoV	Field of View
FWHM	Full Width Half Maximum
ICI	Ice Cloud Imager
IR	Infrared
ISMAR	International Submillimetre Airborne Radiometer
LEO	Low Earth Orbit
LO	Local Oscillator
MATS	Mesospheric Airglow/Aerosol Tomography and Spectroscopy
MLT	Mesosphere and Lower Thermosphere
MoM	Method of Moments
MTF	Modulation Transfer Function
NIR	Near infrared
PO	Physical Optics
PV	Peak to Valley
PSF	Point Spread Function
PTD	Physical Theory of Diffraction
SNR	Signal-to-noise ratio
SPDT	Single Point Diamond Turning
SSB	Single sideband
STEAMR	Stratosphere-Troposphere Exchange And climate Monitor Radiometer
TMA	Three-Mirror Anastigmat
UTLS	Upper Troposphere Lower Stratosphere
UV	Ultraviolet
VIS	Visible light

Contents

Abstract i

List of publications iii

Notations and acronyms vi

1 Introduction 1

2 Background 5
2.1 Transmission through the atmosphere . . . 5
2.2 Optical system . . . 7
2.3 Horn antennas . . . 11
2.4 Detectors and noise . . . 14

3 Instruments for Earth observation 23
3.1 MATS . . . 23
3.2 ISMAR . . . 26
3.3 STEAMR . . . 27

4 Analysis methods 31
4.1 Geometrical optics . . . 31
4.2 Physical optics . . . 42
4.3 Mode matching in circular waveguides . . . 47

5 Implementation and characterization 51
5.1 MATS optics . . . 51
5.1.1 Nadir camera . . . 51
5.1.2 Limb telescope . . . 53
5.1.3 Stray light rejection . . . 61
5.2 Horn antennas . . . 63
5.2.1 Manufacturing methods . . . 63
5.2.2 Radiation pattern measurements . . . 64
5.3 Noise temperature measurements . . . 69

6 Conclusion **71**

7 Summary of appended papers **73**

Acknowledgements **76**

References **79**

Chapter 1

Introduction

Since the formation of Earth some 4.5 billion years ago, the atmosphere has been in constant change and has thereby had an essential impact for life on Earth [1]. Its composition and dynamics affect weather, climate, air quality, natural disasters, freshwater supply, energy harvest, etc. To expand the understanding of the atmosphere's current and future behavior is therefore an all-important task, especially when recognizing the human impact on the environment [2]. It is crucial that researchers get access to reliable and long-term measurement data sets, which serve as input to models for describing the atmosphere.

Earth observation is a collective term for scientific disciplines, which rely on remote-sensing for collecting data to construct advanced models to more accurately describe natural processes on Earth and in its atmosphere [3]. Remote sensing instruments used for this purpose constitute a large class of detectors, which measure electromagnetic radiation over a vast range of wavelengths and can be stationed on the ground, in an airborne vehicle or in space (see Figure 1.1). Depending on the application, these can be very different in appearance, size, mass, power usage, detector technology, etc [4].

Many remote sensing instruments are used for imaging, but the techniques used to obtain the pictures can vary significantly. In the ultraviolet (100-390 nm), visible (390-700 nm) and infrared (700-15000 nm) parts of the electromagnetic spectrum, instruments commonly use focusing optics to form an image, which is captured by a multi-pixel image sensor. Each pixel detects the amplitude, but cannot be used to directly measure the phase of the incoming signals. Such instruments have found many applications in Earth observation, such as monitoring of land mass [6] and vegetation [7], measure aerosols, clouds and atmospheric temperature [8] as well as mapping of natural resources, agriculture and forests [9, 10]. These instruments are usually passive, meaning that electromagnetic radiation from natural sources (e.g. scattered light from the sun or spectral lines from molecular emissions) is measured directly. Active instruments on the other hand transmit a signal, which is scattered in the atmosphere before being detected. Such instruments often have just one or possibly a few pixels. Images are formed by combining several data sets, which can be obtained by changing the direction of the instrument for each exposure [11]. This implies limitations in temporal resolution.

For Earth observation applications, one particular region of interest in the electromag-

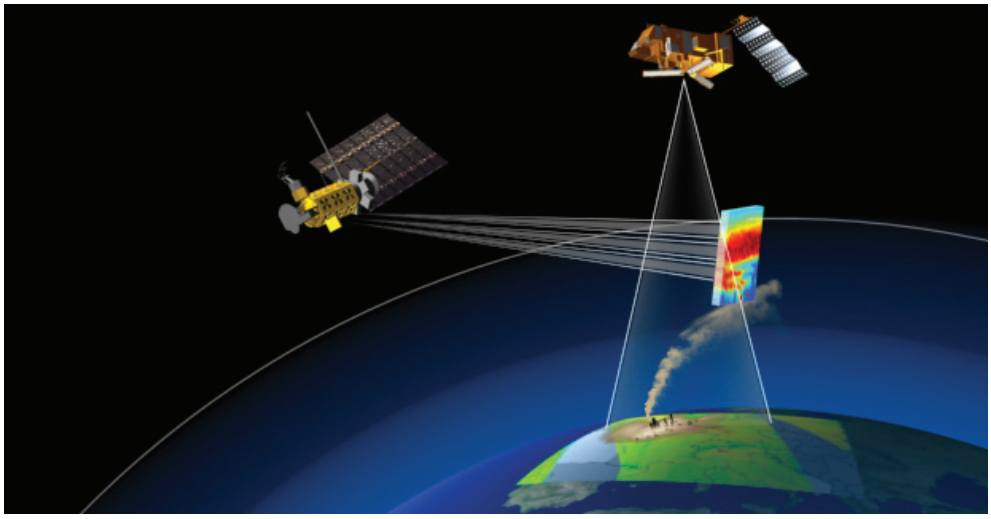

Figure 1.1: Satellites operating in limb (left) and nadir (right) configurations. Edited picture from [5].

netic spectrum is the THz waves, often defined to cover 300-3000 GHz (1-0.1 mm) [12]. Numerous molecular absorption and emission lines limit transmission in the atmosphere at these wavelengths (see Figure 1.2), but at the same time enable spectroscopic measurements to identify and quantify its chemical constituents (e.g. O_2, O_3, H_2O, HNO_3, HCN). Passive radiometers use reflectors to focus the radiation towards its detectors and have been used for several satellite-borne missions throughout the years [13–16]. Heterodyne detectors are often used to measure the phase of a signal through real-time sampling, which gives a high spectral resolution.

An alternative way of constructing images in the THz regions is through aperture synthesis. Instead of a single large focusing reflector, this technique relies on a number of smaller receivers. The recorded phase differences of (plane) waves reaching the receivers of the instrument at different angles of incidence are used in a post-processing algorithm to obtain images. Such systems are currently used for ground-based astronomy [18], but are also planned for future Earth observation missions [19, 20].

Thesis outline

The thesis summarizes the author's contributions to three new instruments for Earth observation: Mesospheric Airglow/Aerosol Tomography Spectroscopy (MATS), International Submillimetre Airborne Radiometer (ISMAR) and Stratosphere-Troposphere Exchange And climate Monitor Radiometer (STEAMR) – see chapter 3. The main focus is on the optical sub-systems of all three instruments, although aspects of the overall system performance are also discussed in connection to the optics. Design and analysis of new kinds of reflective optical systems covering wavelengths from 270 nm-1 mm are presented. The design and optimization of spline horn antennas at 120-874 GHz are also discussed. Special attention is

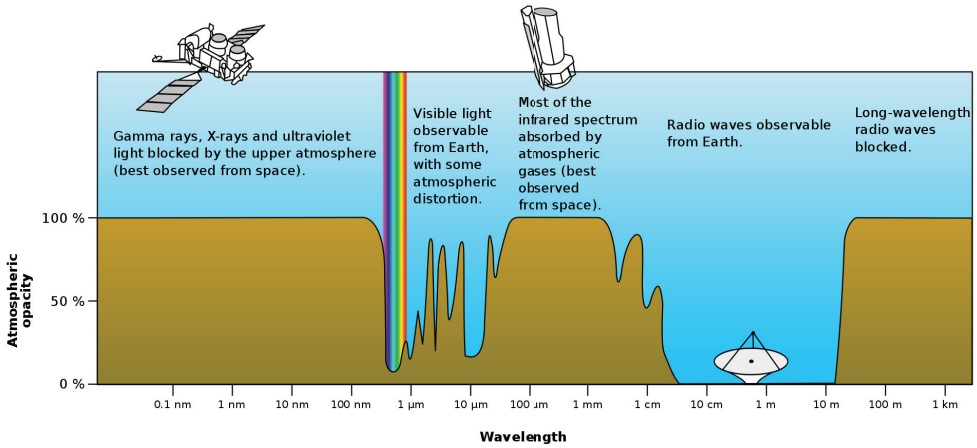

Figure 1.2: Atmospheric opacity versus wavelength. Picture from [17].

given to methods for fabrication and characterization for all these technologies.

In paper A, a reflective telescope for the main instrument on board the MATS satellite is presented. A new design methodology based on the correction of linear astigmatism was applied and tested for the first time. The three-mirror $f/7.3$ (D = 35 mm) telescope used a network of beamsplitters and filters to accommodate six detection imaging channels between 270-772 nm. The telescope had an MTF of 0.45 at 20 lp/mm over a field of view (FoV) of $5.67° \times 0.91°$. This was achieved by using free form aluminum mirrors, which were fabricated using single point diamond turning (SPDT). These had surface figure errors of 34-62 nm (RMS)/193-497 nm (PV). The corresponding roughness values were 2.8-3.5 nm (RMS).

In paper B, stray light rejection and instrument performance of the MATS instrument was analyzed using detailed non-sequential ray-tracing analysis. This was coupled to experimental testing of a baffle prototype coated with a new type of extremely black coating based on vertically aligned carbon nanotubes. The tests showed that a point source transmittance (PST) down to 10^{-6} could be measured with a new stray light facility built for this purpose.

Two complete heterodyne receivers at 874 GHz with record-low noise performance for the ISMAR instrument are presented in paper C. These had a mean double sideband (DSB) noise temperature of 3300 K (minimum 2770 K, maximum 3400 K) at an operation temperature of 40°. This was achieved by carefully considering every part of the receiver, which used state-of-the-art front-end electronics (Schottky mixer diodes and low noise amplifiers (LNA)) while minimizing input losses by integrating a spline horn antenna and low-loss dielectric lens in the same receiver split block. Removing the lens resulted in a DSB noise temperature of 2260 K. Far field radiation patterns from the horn and lens were measured at 869-880 GHz and achieved a main lobe with a full-width half maximum (FWHM) below 5°, which was in good agreement with simulations. The horn and lens were also analyzed using time-domain reflectivity measurements, which showed that the largest reflections come from

the rectangular waveguide interface between the horn and the frequency extender used for the measurements.

Details on the design of the integrated horns and lenses for the ISMAR receivers are presented in paper D. A mode matching code was controlled by an external optimization algorithm to obtain the profile of the spline horn, which resulted in a Gaussicity of 98-99% at 860-890 GHz. Fundamental Gaussian beam mode analysis was used to design a dielectric lens, which was used to make the beam FWHM smaller than 5°. The full horn-lens design was verified using a full-wave solver.

Paper E summarizes fabricated spline horns, which were designed based on the methods outlined in paper D. Two different methods for making the horns based on numerical milling and lathing combined with broaching are presented, as are results from far field radiation patterns measurements between 175-868 GHz. In addition, a horn design at 120 GHz showed that broadband operation of 19% (defined as Gaussicity > 98%) can be achieved with this design method.

An extensive tolerance analysis for the optical system of STEAMR is presented in paper F. Both geometrical- and physical optics methods were used to investigate the manufacturing tolerances of the highly complex optical system, which consisted of six off-axis reflectors and a dual-reflector focal plane array with faceted surfaces for 14 receivers. Relative pointing between the 14 beams and various beam quality (side lobes, beam efficiency etc.) were investigated. The results showed that an overall mounting accuracy of 100 μm was needed to fulfill the scientific requirements. Distortions up to 100 μm of the primary 1.6 m × 0.8 m primary reflector could be accepted. A carbon-fiber mounting structure with two off-axis reflectors and a focal plane unit was built to test alignment and manufacturing methods. Mechanical measurements showed that the reflectors could be mounted to an accuracy better than 50 μm.

Chapter 2 gives a general background of remote sensing systems, its constituents and important figures of merit. Summaries of the MATS, ISMAR and STEAMR instruments are given in chapter 3. Tools for optical design and analysis are provided in Chapter 4, whereas chapter 5 describes methods for characterization. Finally, a closing section with conclusions is given in chapter 6.

Chapter 2

Background

This chapter gives a short overview of the big field of passive optical remote sensing systems, how these detect electromagnetic radiation, its constituents and how uncertainties and limitations influence the performance. Focus is on optical sub-systems and, to some extent, front-end detectors and noise performance.

In scientific and technical literature, the word *optics* is for the most part used when describing a device (an *optic*) that interacts with electromagnetic waves to form the image of an object located at some distance from the optic itself. It is customary to talk about optics for devices that operate at wavelengths in either the UV, VIS or IR. Instead of *electromagnetic radiation/waves*, the word *light* is normally used in this context. For mm/sub-mm waves, other terms such as *aperture antennas, reflector antennas* and *quasi-optics* are frequently used. Although the interaction with its surroundings can be very different, there is no fundamental difference between electromagnetic waves at different wavelengths. In this thesis, the word *optics* is used extensively and regardless of the wavelength of the light. An optical system/optic is hereby defined as *a device that intercepts and transforms/focuses the wavefront of an unguided electromagnetic wave to facilitate detection by a sensor*. It is the aim here to introduce a few important concepts of optical systems and discuss terminology of the different wavelength regions in parallel.

2.1 Transmission through the atmosphere

Following radiation from the source to the instrument and through its sub-systems gives an overview of the steps towards obtaining measurement data. Figure 2.1 shows these steps, which are all associated with uncertainties that will influence the results. In this context, measurement uncertainty can be thought of as any type of systematic or random error that causes unwanted/uncontrolled changes to the magnitude of the data. For an instrument to make a detection, the signal-to-noise ratio needs to be large enough to produce a result with sufficient statistical significance. Hence, reducing measurement uncertainties by minimizing systematic errors and intrinsic noise can be seen as the ultimate goal when developing scientific instruments.

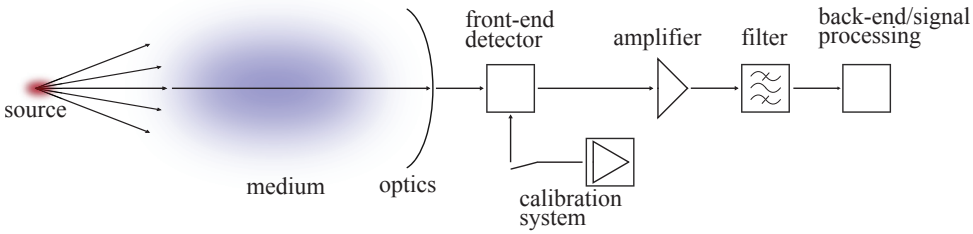

Figure 2.1: Example configuration of a passive optical remote sensing instrument.

However, measurement uncertainties do not only come from flaws in the instruments, but can be a fundamental property of the measured entity itself (electromagnetic radiation in this case). Photons from any source arrive at the input of the instrument randomly, a process that follows a Poisson distribution. The probability p that the number of measured photons N equals k over a time period t is given by [21]:

$$p(N = k) = \frac{e^{-nt}\,(nt)^k}{k!}, \tag{2.1}$$

where n is the expected number of photons per unit of time (proportional to power). For reasonably large values of k, the Poisson distribution can be well approximated by a normal distribution with a mean $\mu = nt$ and standard deviation $s = \sqrt{nt}$. This random arrival of photons gives rise to noise with a signal-to-noise ratio that increases as the square-root of nt:

$$SNR = \sqrt{nt}. \tag{2.2}$$

The flow of photons/energy from the source is often expressed as radiance, which has units of power per unit of solid angle per area ($\mathrm{W \cdot sr^{-1} \cdot m^{-2}}$ in SI units). Denoting the radiance from a source L_ν (or L_λ[1]), the flux through a surface area da from a source in the direction θ (angle between the surface normal and the direction of the flux) is given by [21]

$$\begin{aligned} dP &= L_\nu \cos\theta \, da \, d\nu \, d\Omega \\ &= L_\lambda \cos\theta \, da \, d\lambda \, d\Omega, \end{aligned} \tag{2.3}$$

where $d\nu$ the frequency bandwidth and $d\Omega$ the solid angle subtended by the source.

For Earth observation, the atmosphere can be both the transmission medium and the observation target. As such, it causes wavelength-dependent attenuation and wavefront distortions of all signals (c.f. 1.2). Radiative transfer along a path s in the atmosphere is described by [22]:

$$\frac{dL_\nu}{ds} = -L_\nu \alpha + J_\nu, \tag{2.4}$$

where α and J_ν denote attenuation (extinction) and sources along the path, respectively. This equation can be modified to include scattering, which is often more prominent at shorter

[1] $L_\nu d\nu = L_\lambda d\lambda \rightarrow L_\lambda = c/\lambda^2 L_\nu$

wavelengths. Perhaps the most obvious interaction between the atmosphere and electromagnetic waves from the sun is Rayleigh scattering, which causes light from a clear sky during daytime to appear blue due to a $1/\lambda^4$-dependence of the scattering probability. Rayleigh scattering occurs when light scatters off particles that are much smaller than the wavelength of the light, whereas wavelength-independent (approximately) Mie scattering occurs when light interacts with particles that are of approximately the same size or larger than the wavelength. Molecular vibrational- and rotational modes can cause strong signal attenuation at well-defined wavelengths, but also emit radiation. Measuring emission- and absorption spectra in different regions of the atmosphere can provide information about chemical composition, wind patterns, temperature, pressure, etc., c.f. Figure 2.2

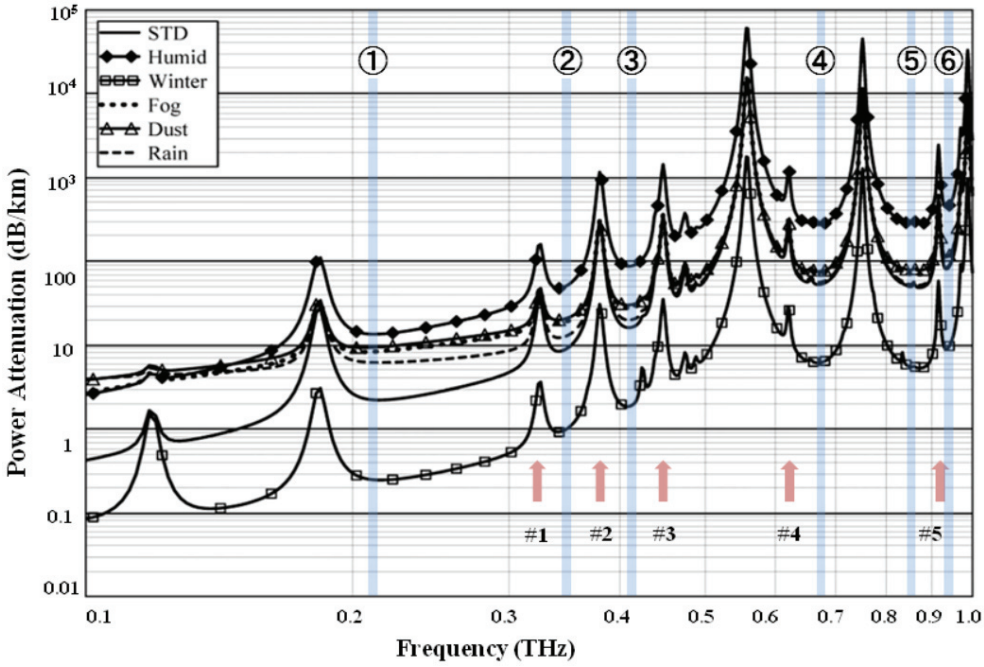

Figure 2.2: Absorption in the atmosphere versus frequency at different humidity levels. Image from [23].

2.2 Optical system

The basic function of any optical system is to intercept incoming electromagnetic waves from within a certain region (the field of view, FoV) and manipulate the wavefronts to achieve an image of the object at the focal plane. The optical systems considered here have large distances to the observation object so that the incoming wavefronts can be considered plane. In fact, from a design point-of-view, the distance is considered infinite so that each field point

in the object plane is specified using two angular coordinates.

The system's ability to resolve fine details is fundamentally limited by the size D of the optic, its focal length f and the operating wavelength λ. For a geometrically perfect optic that focuses rays from one point in the object plane to a single point in the focal plane, diffraction causes energy to distribute in the focal plane according to the Airy function – see Figure 2.3. The circle that defines first minimum of the Airy function is called the Airy disk and can be used as a figure to compare the resolution of different optical systems. Its diameter is given by:

$$D_{Airy} = 2.44\,\lambda f/D. \tag{2.5}$$

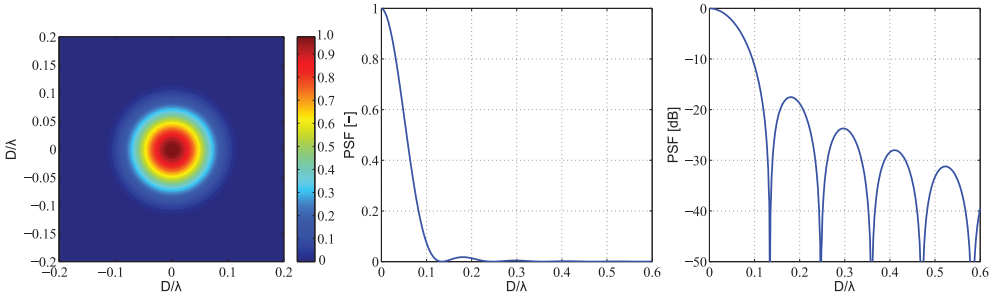

Figure 2.3: PSF from an ideal optic (Airy function).

The precise meaning of f and D come from geometrical optics, where light is described in terms of rays rather than waves and, consequently, diffraction effects are neglected. The focal length f is defined in terms of the system's cardinal points[2] [24] with an object at infinite distance. Two rays, the marginal ray and the chief ray, are shown in Figure 2.4 and are used to define the entrance pupil. The marginal ray starts from the object at zero field height and travels through the optical system where it passes the edge of the aperture stop. The location of the aperture stop is given by where the chief ray passes the optical axis. This ray starts at the top of the object. The entrance pupil is then defined as the image of the aperture stop when viewed from the object side. Similarly, the exit pupil is defined as the image of the aperture stop when viewed from the image side.

The coupling of energy from different field points to the image plane is an $\mathbb{R}^2 \rightarrow \mathbb{R}^2$ mapping, which can be described with a set of distribution functions:

$$G_{i,j} = G(x_i, y_j, \theta, \varphi), \tag{2.6}$$

where (x_i, y_j) are image plane coordinates (with indices for each detector/pixel), whereas (θ, φ) are object plane coordinates. Reciprocity is assumed, meaning that optical systems can be analyzed as either receiving or radiating energy.

In the UV/VIS/IR regions, $G_{i,j}$ can be interpreted as point spread functions (PSF) [24], which describe the intensity distribution in the image plane for a given angle of incidence of

[2]Cardinal points are strictly only defined for axially symmetric systems.

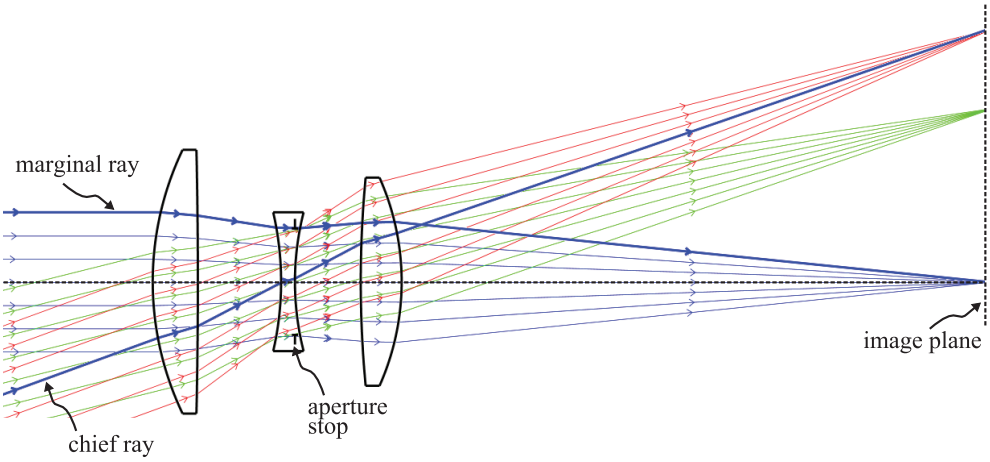

Figure 2.4: The marginal- and chief rays for an axial three-lens system with an object at infinite distance.

the light. With optical components typically being relatively large in terms of the operating wavelengths, the resolution of such systems is often limited by aberrations[24], which can be thought of as the inability to geometrically map each point in the object plane to precisely one point in the image plane. Such limitations can come from the optical design itself or from imperfect and/or misaligned optical components. Besides causing blurring of the image (in some cases wavelength-dependent), aberrations can also make the mapping from object to image plane non-rectilinear and thereby warping/distorting the image.

At mm/sub-mm wavelengths, the $G_{i,j}$ functions are normally referred to as the (antenna) directivity, which describes how much power is raditated/received by the antenna from each direction. With typical apertures not larger than a couple of thousands of wavelengths and small focal planes (often just one single detector), these systems tend to be dominated by diffraction. The directivity is a dimensionless quantity which is written as [25]

$$D(\theta, \phi) = \frac{U(\theta, \phi)}{U_0}, \tag{2.7}$$

where U is the radiation intensity and U_0 the radiation intensity of an ideal isotropic source. Losses in the antenna naturally decrease the amount of power coupled to the focal plane. Collecting all such losses into an efficiency term called radiation efficiency, η_{rad}, the antenna gain G can be written as

$$G(\theta, \phi) = \eta_{rad} D(\theta, \phi). \tag{2.8}$$

The space around a radiating (reflector) antenna where diffraction effects dominate are often divided into three regions:

$$\begin{aligned} \text{Reactive near-field:} \quad & 0.62\sqrt{D^3/\lambda} < r \\ \text{Radiative near-field (Frensel diffraction):} \quad & 0.62\sqrt{D^3/\lambda} < r < 2D^2/\lambda \\ \text{Far field (Fraunhofer diffraction):} \quad & 2D^2/\lambda > r \end{aligned} \tag{2.9}$$

The gain/radiation pattern is normally given in the far field, where it can be expected to have little or no variation with distance.

Losses naturally exist in any optical component. Absorption occurs in both reflective and refractive components, where the latter often exhibit a relatively strong wavelength-dependency (dispersion). Many metals (aluminium, gold, copper etc.) have reflectivities close to 1 at sub-mm wavelengths [26]. However, at wavelengths below ~500 nm, the reflectivity numbers tend to decrease. Whereas large-scale errors primarily distorts the wavefront, features that are in the same order of magnitude as the wavelengths (roughness) tend to scatter light instead. Numerous theoretical and semi-empirical scattering models exist [27], all with different advantages and shortcomings. The distribution of scattered light depends on the surface statistics of the roughness profile. For a random roughness profile, the total integrated scatter (TIS) is given by [28]:

$$TIS = \left(\frac{2\pi \Delta n \, \sigma}{\lambda} \right)^2, \tag{2.10}$$

where Δn is the difference in refractive index across the surface and σ is the RMS surface roughness. For a mirror in air or vacuum, Δn becomes 2, whereas the corresponding number for a typical optical glass becomes approximately 0.5. Hence, for a given surface roughness, mirrors are more prone to scattering than lenses. Scattering is often described in terms of a bidirectional reflectance distribution function (BRDF), which is defined as the ratio of reflected radiance from an opaque surface to the incident intensity on the same surface:

$$BRDF(\theta_i, \varphi_i, \theta_r, \varphi_r) = \frac{dL_r(\theta_r, \varphi_r)}{dI_i(\theta_i, \varphi_i)}, \tag{2.11}$$

where angles with indices i and r denote the angle between the incident direction and the surface normal, and angle between the scattered direction and the normal, respectively. For a Lambertian source, the BRDF function is constant and equal to the reflectivity of the surface divided by π.

For any optic, vignetting will cause an intensity roll-off in the image plane that increases with distance from the center due to a partial or complete blocking of the light passing through the system. Under-sized components or structures blocking the light path can cause vignetting, but so-called *natural vignetting* always occurs in every optical system [29]. This is also referred to as the cos^4 *law* since the intensity in the image plane decreases as cosine to the fourth of the field angle.

In addition to field-dependent roll-off, blocking of the optical path will also cause diffraction effects, which can be avoided by the use of off-axis optical designs. Figure 2.5 shows two dual-reflector telescopes in on- and off-axis configurations. Employing an off-axis configuration practically eliminates diffracted light from the secondary/sub reflector. On the other hand, such designs are generally more difficult to build and can lead to increased aberrations as well as cross polarization.

Sources located outside the FoV (stray light) can couple to the image plane through unwanted reflections/scattering occurring inside or in the vicinity of the instrument. For a given point source outside the FoV, part of the incoming radiation will be distributed across the entire image plane. Stray light rejection is often characterized in terms of point-source transmittance (PST), which is defined as the ratio of the irradiance E_{in} at the input of the instrument

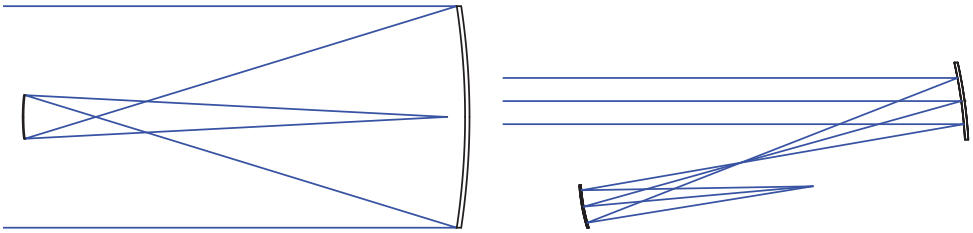

Figure 2.5: On- and off axis Gregorian telescope designs.

to the irradiance E_{image} in the image plane for a given angle of incidence:

$$PST(\theta, \varphi) = \frac{E_{image}}{E_{in}}. \tag{2.12}$$

Analyzing the stray light rejection of the instrument is highly important, especially for Earth observation where disturbing sources such as albedo, scattered light from the sun or light from cities are often close to the observation targets. Using baffle structures, eliminating critical light paths, employing low-reflectance coating etc. are all parts of common measures that are taken to minimize stray light problems [30].

2.3 Horn antennas

Coupling radiation to a sensor in the focal plane is especially challenging for sub-mm systems where the wavelengths involved are much longer than the components used for the actual detection. To tackle this problem, different kinds of antennas can be used to intercept the signals and guide them to the detector. For instance, this can be achieved using a combination of lenses and planar antennas [31], or horn antennas [25]. Like reflector antennas, horn antennas are usually defined as aperture antennas and act as intermediaries between the optical system (where waves propagate in free space) and the front-end detectors (guided waves). As with any other antenna, horn antennas (feed horns or simply horns) are characterized in terms of radiation pattern/gain that becomes an integral part of the overall performance. Physically, a horn antenna is a hollow metal structure that is tapered down from the aperture to the waveguide connection of the receiver. Some examples of designs that have been used over the years are pyramidal, E-plane, H-plane, conical and exponential horns [32]. Three rotationally symmetric horns (Potter-, corrugated- and spline horns) are described in terms of basic geometry and performance below.

Potter horn

A Potter horn antenna [33] (or a dual mode horn) is circularly symmetric and consists of piecewise linearly tapered sections, cf. figure 2.6. In designing this type of horn, both dominant modes of a circularly symmetric waveguide, i.e. the TE_{11} and TM_{11}, are excited and

appropriately balanced in phase and amplitude to achieve a highly symmetrical main beam with side lobes at levels 30 dB below the maximum. It has a coupling to the fundamental Gaussian beam mode (Gaussicity, see Section 4.2) and cross polar levels are approximately 96.3% and 1.4% [34]. Moreover, a Potter horn has a 10% bandwidth in terms of -20 dB cross polarization level.

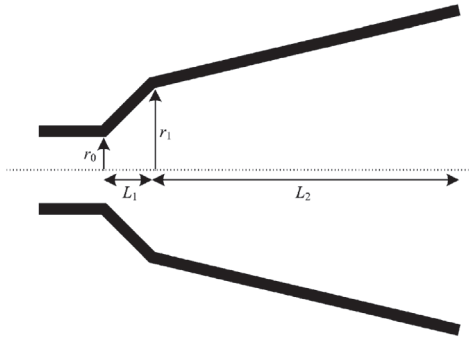

Figure 2.6: Potter horn. Image from [35].

Having a profile radius that is monotonically increasing, the Potter horn is relatively easy to fabricate with good precision and is hence a good option as a feed for many systems, especially at high frequencies [36].

Corrugated horn

By adding grooves to a smooth conical horn, a corrugated horn (scalar horn) antenna is obtained. The depths of the corrugations are increased from $\lambda/2$ at the back of the horn, referred to commonly as the throat section, and then readily tapered to $\lambda/4$ which is then maintained as far as the aperture, cf. figure 2.7. Having a groove depth of $\lambda/4$ will cause the ϕ components (in cylindrical coordinates) of the E and H fields to have infinite reactances and hence, $E_\phi = H_\phi = 0$. This gives the so-called balanced hybrid mode condition which results in a highly uniform field distribution across the aperture, which in turn gives low side lobes, axial symmetry of the beam and high Gaussicity (98.1%). For these reasons, the corrugated horn has been used extensively over the years for radio telescopes.

It is possible to predict the size and position of the Gaussian beam waist using the following design equations [38]:

$$w_o = \frac{0.644a}{1 + [\pi(0.644a)^2/(\lambda R_h)]^2} \tag{2.13}$$

$$z = \frac{R_h}{1 + [\lambda R_h/(\pi(0.644a)^2)]^2} \tag{2.14}$$

Here a is the aperture radius of the feed and $R_h = \frac{l_s + l_f}{\cos\alpha}$ is the slant length from the aperture to the center of curvature, cf. figure 2.7.

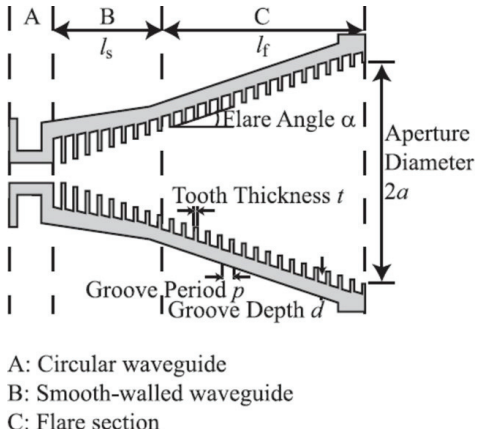

Figure 2.7: Profile of a corrugated horn. Image from [37].

Spline horn

Even though corrugated horns have excellent performance in terms of many important figures of merit, the manufacturing process becomes a serious issue at THz frequencies due to the fine details in the interior of the horns. For instance, at 300 GHz, the desired depth of the corrugations ($\lambda/4$) is 250 µm . It has been shown that a smooth horn having an optimized, non-linear profile can give similar or better performance compared to the corrugated feed horn [39]. This is achieved at the cost of having a feed that is approximately 50% longer than the corrugated one, cf. figure 2.8.

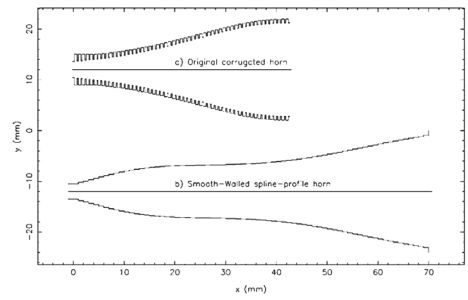

Figure 2.8: Corrugated horn (a) and spline horn (b) at 80-120 GHz with similar performance. Image from [39].

2.4 Detectors and noise

Countless types of detectors have been invented throughout the years. A few common types used for applications in Earth observation are summarized in Table 2.1. The principles of detection and the types of technologies used differ considerably, especially when comparing detectors in different regions of the electromagnetic spectrum. Detectors for sub-mm/THz waves generally utilize the wave-nature of electromagnetic radiation, meaning that the oscillations of the waves can be sampled at rates that allow time-resolved signals. The photon energies at 100-1000 μm (3000-300 GHz) vary between 1.24-12.4 meV, which is far below the band gaps of common semiconductors/semiconductor compounds (Si, GaAs, InP, etc.) that are in the order of one to a few eV. However, at shorter wavelengths in or around the visible range, the opposite is true. Photon energies are high enough to directly excite electrons to the conduction band, which is utilized to detect electromagnetic radiation incident on the semiconductor. This type of detector exploits the quantum nature of light and can be thought of as a photon counter.

Name	Technology	Wavelengths [μm]
CCD [40]	photoconductor	0.25-1.1
CMOS [41]	photoconductor	0.25-1.1
HEB [12]	bolometer	> 60
Schottky mixer [12]	varistor diode	> 60
SIS [12]	Josephson junction	> 240
HEMT (LNA) [42]	transistor	> 300

Table 2.1: Examples of detectors used in the UV, VIS, NIR and sub-mm wavelength regions.

Any type of detector will generate noise intrinsically, which unavoidably decreases the signal-to-noise ratio of a given measurement. Electrons inside all electronic components are affected by the random thermal jitter of atoms. This causes thermal noise (Johnson noise [43]), which scales linearly with temperature:

$$P_{Johnson} = 4k_{\mathrm{B}}T\Delta\nu, \tag{2.15}$$

where $\Delta\nu$ is the bandwidth at which the noise is measured. Hence, detectors at all wavelengths are often cooled (actively or passively) to decrease thermal noise.

Heterodyne detection

Detector systems capable of measuring both the amplitude and phase of the incoming signals are commonly referred to as heterodyne detectors, whereas those that only measure amplitude are known as direct detectors. Heterodyne detectors can be configured in many different ways, but all contain a non-linear electronic component that acts as a frequency mixer. Figure 2.9 shows the basic principle for this type of detector, where the RF signal from the source and a local oscillator (LO) signal are input to the mixer that outputs a series of harmonics.

The desired output signal has a frequency given by

$$\nu_{IF} = |\nu_{RF} - \nu_{LO}| \tag{2.16}$$

and is called the intermediate frequency (IF). Typically, the down-converted IF signal has a frequency between 1-20 GHz where amplification and analog-to-digital (A/D) conversion in the back-end detector can be made efficiently. Since ν_{IF} is given by the absolute difference between the RF- and LO frequencies, signals with frequencies $\nu_{RF} - \nu_{LO}$ ($\nu_{RF} > \nu_{LO}$) and $\nu_{LO} - \nu_{RF}$ ($\nu_{LO} > \nu_{RF}$) are overlayed. This defines the upper- and lower sidebands. Most mixers cannot distinguish between the two sidebands and are known as double sideband (DSB) mixers. Conversely, those that are able to detect one sideband at a time are called single sideband (SSB) mixers.

Although heterodyne systems can be used to extract more information about the observation targets by providing spectrally resolved signals, the generation of the LO signal often becomes a problem. Since few practical fundamental sources exist, many systems therefore rely on solid-state frequency multipliers to generate the LO signal. However, the available output power of such sources tend to have a minimum around 1 THz [44]. Different laser technologies are more common for LO generation at higher frequencies. Much effort is being made to solve the problem of lack of sources around 1 THz, which is often called the "THz gap". Low power efficiency for cascaded solid-state multipliers together with difficulties of distributing the LO power becomes a great challenge when building heterodyne multi-detector systems. Hence, such systems have historically been limited to one or a few receivers.

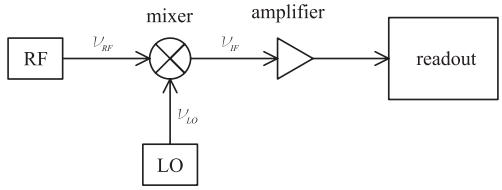

Figure 2.9: Basic principle for heterodyne detection, where the frequency of the IF signal (ν_{IF}) is given by the difference in frequency between the RF (ν_{RF})and LO (ν_{LO}) signals.

For Earth observation instruments, detectors based on Schottky mixer receivers and/or HEMT technology are far more common than HEB and SIS, which require cryogenic cooling to function. The Schottky diode itself is a two-terminal rectifying device that consists of a metal-semiconductor junction, where an electric potential barrier is created due to the difference in electron affinity between the two materials. A depletion region is formed in the semiconductor close to the metal contact, which gives rise to non-linear current-voltage and capacitance-voltage characteristics. When an LO signal is applied, the incoming RF signal $v_{RF}(t)$ becomes modulated by the time-varying conductance g_{LO} and an IF signal is produced:

$$i_{IF}(t) = g_{LO}(t) \cdot v_{RF}(t). \tag{2.17}$$

Schottky diodes can either be made as discrete components or monolithically integrated on circuits. These are housed inside metallic blocks, where waveguide structures with suspended

microstrip probes are used to couple signals from the horn to the device. The IF signal is normally filtered and amplified by at least one low noise amplifier (LNA) stage before reaching the back-end electronics.

The intrinsic noise of systems operating at sub-mm wavelengths are often expressed in terms of temperature. This concept is connected to the radiation from black body sources, which are Lambertian (radiance is independent of solid angle) and have a temperature-dependent radiance given by Planck's law:

$$\begin{aligned} L_\nu(T,\nu) &= \frac{2h\nu^3}{c^2}\frac{1}{e^{\frac{h\nu}{k_\mathrm{B}T}}-1} \\ L_\lambda(T,\lambda) &= \frac{2hc^2}{\lambda^5}\frac{1}{e^{\frac{hc}{\lambda k_\mathrm{B}T}}-1}, \end{aligned} \tag{2.18}$$

where h is the Planck constant, c the speed of light, k_B the Boltzmann constant and T the physical temperature of the black body. In the Rayleigh-Jeans approximation, it is assumed that $h\nu \ll k_\mathrm{B}T$ and a Taylor expansion can be used to re-write equations 2.18 as

$$\begin{aligned} L_\nu(T,\nu) &\simeq \frac{2\nu^2 k_\mathrm{B}T}{c^2} \\ L_\lambda(T,\lambda) &\simeq \frac{2ck_\mathrm{B}T}{\lambda^4} \end{aligned} \tag{2.19}$$

Assuming atmospheric target temperatures in the range 100-350 K, it is clear from Figure 2.10, that the Rayleigh-Jeans approximation is indeed valid at sub-mm wavelengths.

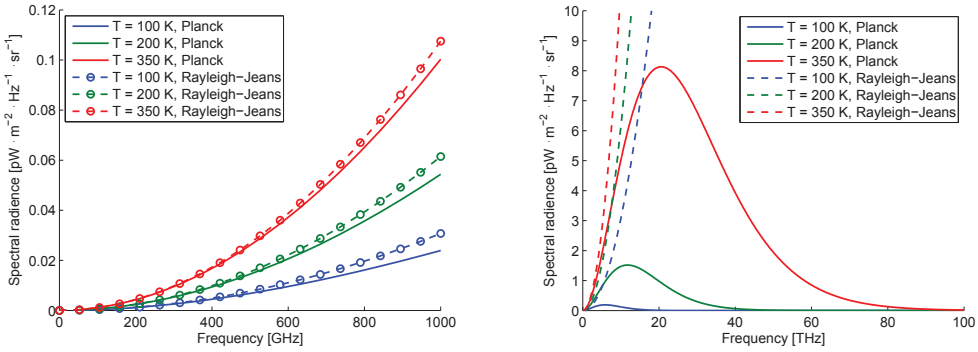

Figure 2.10: Comparison of spectral radiance as calculated using Planck's law and the Rayleigh-Jeans approximation at 100, 200 and 350 K.

For a linearly polarized receiver in the sub-mm wavelength region, the received spectral

power is obtained by integrating the radiance over the aperture and solid angle:

$$\begin{aligned} P_\nu &= \frac{1}{2} \iint_{4\pi} A_e \, \frac{2\nu^2 k_\mathrm{B} T_{src}}{c^2} \, d\Omega \\ &= \frac{\nu^2 k_\mathrm{B} T_{src}}{c^2} \iint_{4\pi} A_e \, d\Omega, \end{aligned} \tag{2.20}$$

where A_e is the effective area and T_{src} the temperature of the source. The factor $\frac{1}{2}$ comes from the assumption that the detector is linearly polarized. Integrating over the system bandwidth and using the antenna theorem [45], which states that $\iint_{4\pi} A_e d\Omega = \lambda^2 = c^2/\nu^2$ for a single-mode antenna, equation 2.20 can be expressed as

$$P = k_\mathrm{B} \Delta\nu T_{src}, \tag{2.21}$$

where $\Delta\nu$ is the bandwidth of the system. Hence, the detected power can conveniently be expressed in terms of temperature. This is used to define the antenna temperature, which describes the amount of noise an antenna produces in a given environment. The antenna temperature is thus not determined by the physical temperature of the antenna, but by the gain and the temperature "seen" by the antenna:

$$T_A = \frac{\iint_{4\pi} T_{src}(\theta, \varphi) \, G(\theta, \varphi) \, d\Omega}{\iint_{4\pi} T_{src}(\theta, \varphi) \, d\Omega}, \tag{2.22}$$

where $G(\theta, \phi)$ is the gain of the antenna. For an isotropic source (i.e. $T_{src}(\theta, \varphi) = T_{src}$), the antenna temperature therefore equals the source temperature. Noise contributions from the components within the system are often also defined using temperatures. Equation 2.21 can then be used to to express the detected signal:

$$P_{det} = k_\mathrm{B} \, \Delta\nu \, T_{sys} \, G = k_\mathrm{B} \, \Delta\nu \, (T_A + T_{rec}) \, G_{rec}, \tag{2.23}$$

where T_{sys} denotes the noise temperature of the system and T_{rec} the intrinsic noise contribution from the receiver. The factor G_{rec} denotes the gain of the receiver. A DSB mixer receiver that overlays the two sidebands receives more power and is generally more sensitive, given that a continuum is measured.

The receiver noise T_{rec} is not a simple constant that can simply be measured and subtracted, but instead depends on a multitude of factors (e.g. temperature and frequency) and is statistical in its nature.

State-of-the-art receivers operating at room temperature at frequencies between 100-1000 GHz achieve noise temperatures between a couple of hundreds to few thousands of Kelvin (c.f. Figure 2.11). With typical source temperatures at some hundreds of Kelvin, it becomes necessary to increase the antenna temperature relative to the intrinsic noise to enable

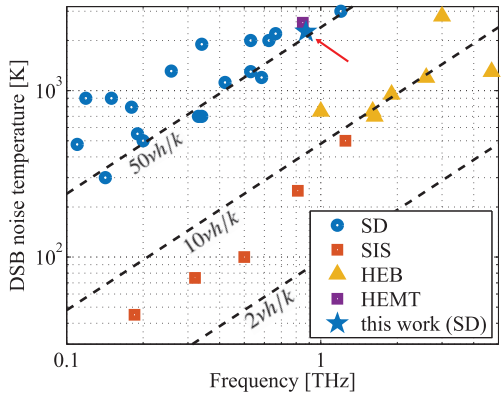

Figure 2.11: State-of-the-art DSB noise temperatures of receivers based on Schottky diodes (SD) [46–56], SIS [57–60], HEB [61–66] and HEMT [67] technology. Noise performance from paper C is indicated with a blue star.

detection. Assuming that the noise in each measured sample is statistically independent, it follows that the RMS fluctuations can be written as

$$\Delta T_{RMS} = \frac{T_{sys}}{\sqrt{N}}, \tag{2.24}$$

where N is the number of independent sample points. Hence, the number of sample points needs to increase in order to decrease the the noise fluctuations. This can be done by using more receivers or by integrating for a longer time and thereby sample the signal over more cycles. For a system with no gain fluctuations, the RMS fluctuations can be written as

$$\Delta T_{RMS} = \frac{T_{sys}}{\sqrt{\Delta\nu\,\tau}}, \tag{2.25}$$

where τ is the integration time. The corresponding signal-to-noise ratio becomes

$$SNR = \frac{T_{src}}{T_{sys}}\sqrt{\Delta\nu\,\tau}, \tag{2.26}$$

Hence, for uncorrelated (white) noise, the system noise decreases with integration time and bandwidth. However, as the integration time increases, low-frequency noise components start to become more significant. This type of noise is often referred to as $1/f$ noise[3] or pink noise. When pink noise dominates, ΔT_{RMS} will stay constant regardless of how long the integration time is. Yet another limitation is often set by the instability of the system itself over time. This can be modeled as fluctuations in gain, which modifies equation 2.27 to:

$$\Delta T_{RMS} = T_{sys}\sqrt{\frac{1}{\Delta\nu\,\tau} + \left(\frac{\Delta G}{G}\right)^2}. \tag{2.27}$$

[3]The symbol f denotes focal length in this thesis – not frequency. This is the only exception.

The absolute radiometric accuracy of a heterodyne detectors at THz frequencies can often be much improved by incorporating temperature-controlled black body calibration targets inside the instrument. A moving mirror that cuts into the beam path and steers radiation from the calibration target to the receiver(s) is often used for this purpose – see Figure 2.12. At frequencies $\lesssim$50 GHz, noise diodes that are coupled to the detector using electronic switching are sometimes used, although these may suffer from long-term stability issues [68].

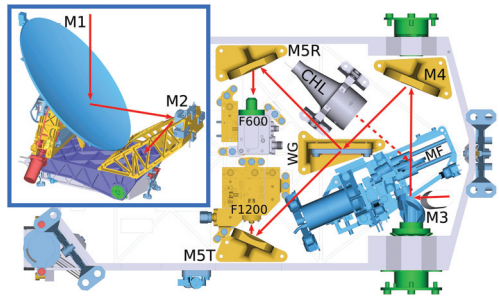

Figure 2.12: Optical design for SWI. The calibration target and rotating mirror are labeled CHL and MF, respectively. Image from [69].

Each part of a receiver system consisting of cascaded components has a noise temperature contribution and a gain (or loss). If the source temperature and the noise temperature and gain of all components are known, T_{sys} can be computed using Friis formula [70]:

$$T_{sys} = T_A + T_1 + \frac{T_2}{G_1} + \frac{T_3}{G_1 G_2} + ... + \frac{T_n}{G_1 G_2 ... G_{n-1}}, \tag{2.28}$$

To minimize the noise contribution from the receiver, it is crucial to minimize the losses (or maximize the gain) of the first components in the chain. With a Schottky mixer receiver as the first component, this means that the conversion loss (RF to IF) and noise temperature should be minimized. For the same reason, it is equally important to minimize losses in the optics, horn antenna and waveguides that precede the mixer.

Direct detection

Direct detectors measure power, but cannot be used to extract phase information from the signal. With different detector technologies, a vast range of wavelengths can be detected. Systems based on Schottky diodes exist up to 850-900 GHz [71, 72] and typically include one or a few detectors in the image plane. Integrated image sensors with millions of pixels based on CCD and CMOS technologies are commonly used for the UV up to NIR wavelengths. Even though CMOS technology has improved greatly in the past decades and dominate the market for consumer products [73], CCDs are still often the best choice for applications requiring high dynamic range and low noise [74].

A CCD image sensor is based on a silicon substrate with a *p* doped epitaxial layer on top. Photons with sufficient energy that strike the surface of the sensor can be absorbed

and knock up electrons in the epitaxial layer to the conduction band and thereby create an electron-hole pair. To prevent spontaneous recombination, a positive voltage is applied to a gate electrode (electrically insulated from the epitaxial layer) in each pixel. This voltage is maintained during the exposure to allow for excited electrons to accumulate. After the exposure, a readout process begins where the electrons in each row are shifted down to the adjacent row by changing the gate voltages in order to make the electrons move in the desired direction. Electrons in the bottom row are shifted into a readout register, where the electrons are shifted sideways pixel-by-pixel to an on-chip amplifier, which produces a signal that scales with the number of electrons in the pixel.

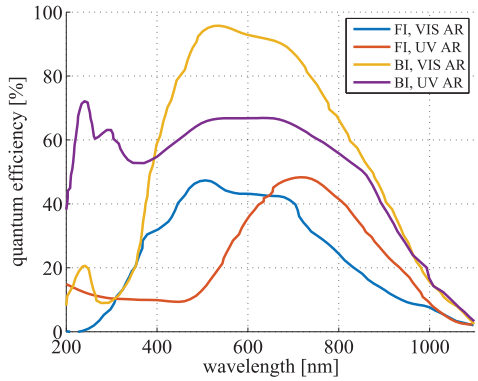

Figure 2.13: Comparison of typical quantum efficiencies between front illuminated (FI) and back illuminated (BI) CCDs with anti-reflection coatings (AR) optimized for the VIS and UV regions. Data from [75].

The ratio of number of incident photons to the number of electrons in the condition band is called quantum efficiency. To excite an electron to the conduction band of the silicon, a minimum photon energy of 1.1 eV (1127 nm) is required. At shorter wavelengths, the reflectance of the silicon increases and causes a cutoff in the UV – see Figure 2.13. The peak quantum efficiency and bandwidth of a CCD is improved significantly for back-illuminated designs [74]. In this case, light is incident on the back of device and will not interfere with gate electrodes and wiring. To further improve the quantum efficiency, the bulk silicon is thinned down. Anti-reflection coatings are applied on top of the silicon substrate to improve the transport of photons to the epitaxial layer and can be optimized for performance in a selected wavelength band.

During exposure and readout, electrons in a CCD can be excited to the conduction band without any illumination of the sensor. This process is called dark current and happens spontaneously in different parts of the CCD due to electrons being thermally excited [76]. The obvious way to tackle this problem is through cooling, which reduces dark currents non-linearly. Operating temperatures of approximately -20° are often sufficient to ensure that dark currents do not dominate in terms of noise. Each pixel of the CCD is somewhat unique in terms performance and although dark currents are inherently random in nature, the dark

current distribution across a frame is to some extent deterministic. Hence, for a given exposure time, the signal-to-noise ratio in an image can be improved by subtracting a dark frame from the main exposure. The same is true for the bias frame, which represents an offset contribution to the total signal. It is essentially a zero-length exposure and by averaging over a few such frames, the signal-to-noise ratio can be increased and the resulting frame can be used to correct for biasing offsets.

Another important contributor to the noise of the final image is caused by the conversion of discrete charges to voltage and by the final analog-to-digital conversion. This gives rise to readout noise that is typically dominated by the on-chip amplifier. Since the same amplifier is used for all pixels during the readout, almost the same excess noise signal is added to each pixel. Readout noise is dependent on the frequency at which the readout occurs. For low readout frequencies, $1/f$ noise is typically more troublesome, whereas white noise (frequency-independent) tends to dominate at high frequencies [74].

The signal-to-noise ratio in each pixel of a CCD can be expressed in terms of the RMS number of electrons n per second. Since the noise contributions are uncorrelated, these can be added as the sum the squares. Using equation 2.1 and noting that the number of electrons in a pixel is proportional to the square root of the power associated an incoming photon, the signal-to-noise ratio can be written as

$$SNR = \frac{\Phi_{sig}(\lambda)\,\epsilon_q(\lambda)\,\tau}{\sqrt{(\Phi_{sig}(\lambda) + \Phi_{stray}(\lambda))\,\epsilon_q(\lambda)\,\tau + DC\,\tau + n_{read}^2}}, \tag{2.29}$$

where $\Phi_{sig}(\lambda)$ is the flux of photons, $\epsilon_q(\lambda)$ the quantum efficiency, τ the exposure time, $\Phi_{stray}(\lambda)$ unwanted stray light photon flux, DC the dark current and n_{read} the excess electrons due to readout noise. The total signal-to-noise ratio is obtained by integrating over wavelength.

Unlike a diffraction-dominated single-mode system observing an extended black body source, the detected signal of an optical instrument at short wavelengths will increase as the entrance pupil diameter is increased. Hence, both spatial resolution and sensitivity of the instrument can be increased with larger optical apertures. Another way of increasing the signal is to employ on-chip binning, where the signal from two or more physical pixels are combined on the CCD chip and read out as a single pixel. The detected power then scales with the number of binned pixels at the expense of reduced resolution in the image plane.

In order to use the optical instrument for quantitative measurements, it is necessary to perform a calibration against some well-defined standard. In essence, this means that a source with known spectral radiance that covers the FoV is imaged [77]. This process is known as flat fielding. The sources are sometimes referred to as full-field or flood sources and can be used to characterize non-uniform responses from the detector, vignetting in the optical system, linearity, absolute response of the instrument, etc. Such targets can also be implemented inside an instrument to allow for calibration during operation and thereby decreasing measurement uncertainties further [78].

Chapter 3

Instruments for Earth observation

This chapter provides a background to the three instruments for Earth observation on which this thesis is based: MATS, ISMAR and STEAMR. A brief overview of the scientific goals of the projects are given, as are the basic instrument requirements and technical solutions.

3.1 MATS

At the time of writing, a new low-earth-orbit (LEO) satellite for the atmospheric research called Mesospheric Airglow/Aerosol Tomography Spectroscopy (MATS) is being built and tested [79]. This is a Swedish microsatellite with launch planned for the end of 2019. The scientific aim of MATS is to study gravity waves[1] [79] in the mesosphere. These are upward-traveling air-pressure waves that are formed at the surface of the Earth when e.g. strong winds sweep over large obstacles such as mountains or frontal systems. As the atmospheric pressure decreases at higher altitudes, the gravity waves expand and finally break apart, primarily in the mesosphere and lower thermosphere (MLT) at altitudes 50-130 km. This is similar to the waves in water of the oceans, which are also affected by the topography at the bottom. Gravity waves transfer momentum and energy in the atmosphere and are responsible for phenomena at both small and large scales, from local turbulence to large-scale circulation [81].

Physical simulation of large-scale gravity waves is done today, whereas the models are tuned to produce realistic output for small-scale waves [79]. New models therefore aim to describe the entire physical process of the gravity wave spectrum, from the formation at low altitudes, through the atmosphere and up to the MLT. For successful modeling, it is crucial to have reliable observational data. However, there is currently a gap in existing data of gravity waves, especially in the MLT. Besides investigating the gravity wave spectra, such data is also important for three-dimensional modeling of the waves themselves. Historically, different groups in the field have focused on separate parts of the atmosphere, where the

[1] Not to be confused with *gravitational waves* [80]

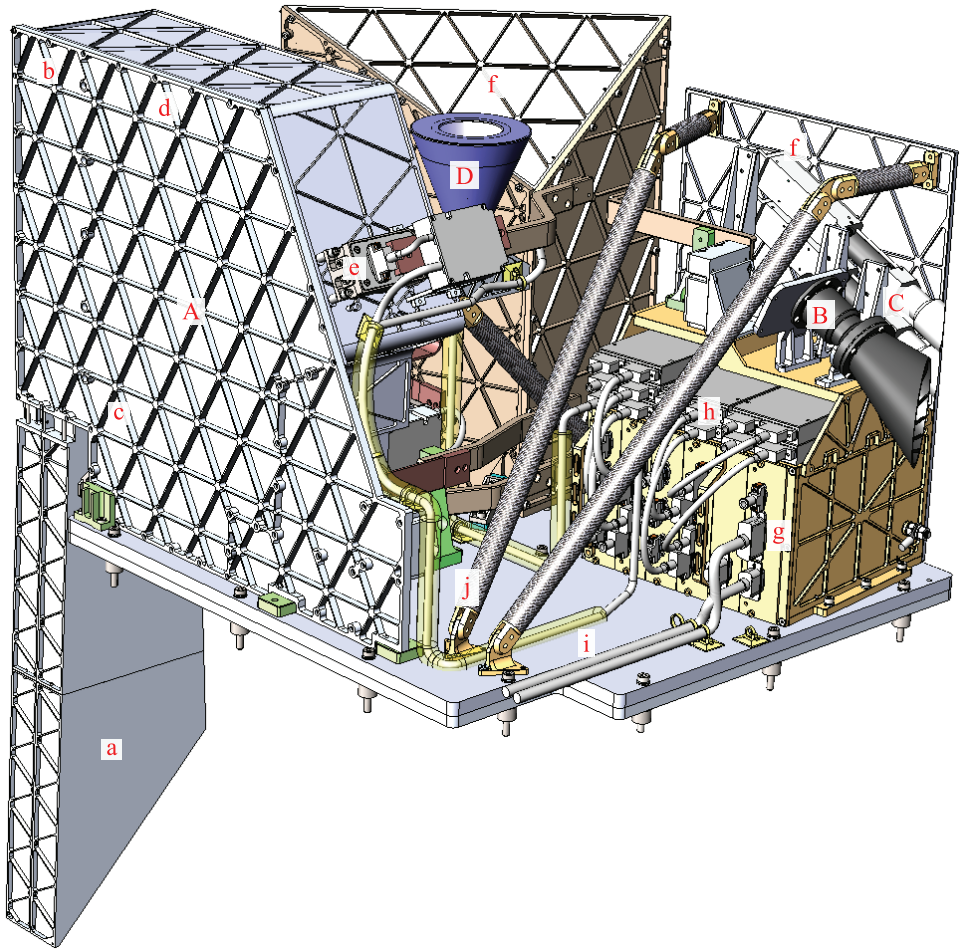

Figure 3.1: Overview of the MATS payload. Colors are not representative of the real hardware. A: limb instrument, B: nadir camera, C: photometers, D: star tracker, a: limb baffle, b: M1 location, c: M2 location, d: M3 location, e: CCD, f: radiators, g: on board computer, h: readout electronics, i: base plate/interface to platform, j: supporting struts.

altitude of approximately 100 km constituted a dividing line in terms of research interest. Understanding the atmosphere as a whole has become more and more important and since gravity waves travel across the different layers in the atmosphere, these become one way of erasing this dividing line.

MATS aims to measure gravitational waves at altitudes 70-110 km in the atmosphere by making observations in a limb-viewing configuration (c.f. Figure 1.1). It is not the first satellite-borne instrument used for similar purposes [82–85], but it will cover a gap [86] in the measured gravity wave spectra by observing wavelengths between 0.2-20 km vertically

channel	λ [nm]	ν [lp/mm]	FoV [°]	SNR [-]
UV1	270.0 ± 1.5	20.0	5.67 × 0.46	100
UV2	304.5 ± 1.5	20.0	5.67 × 0.46	100
IR1	762.0 ± 1.8	10.0	5.67 × 0.80	500
IR2	763.0 ± 4.0	10.0	5.67 × 0.80	500
IR3	754.0 ± 1.5	5.0	5.67 × 0.80	500
IR4	772.0 ± 1.5	5.0	5.67 × 0.80	500
nadir	763.0 ± 4.0	-	24.4 × 6.10	100

Table 3.1: Wavelength bands, vertical resolution requirements (given as the spatial frequency where the MTF should be at least 0.5), FoV and required SNR of the imaging channels of the limb and nadir instruments. The imaging requirement for the nadir camera is 80% encircled energy within a radius of 250 µm.

and 5-100 km horizontally. It will do so using two cameras on board, which are here referred to as the *limb instrument* and the *nadir camera* – see Figure 3.1. The main one of these is the limb instrument, which uses a total of six narrowband channels (3-8 nm) to observe the mesosphere in the wavelength bands covering 270-304.5 nm and 754-772 nm – see table 3.1. Emissions in these bands come from scattered light from high-altitude clouds known as noctilucent clouds [87] and O_2 atmospheric airglow [88]. The nadir camera has a single channel operating at 759-767 nm. When multiple images from different directions in the limb are combined, tomographic methods can be used to obtain three-dimensional wave patterns. With several wavelength channels available, spectroscopy methods can also be applied, which – when combined with tomography – can result in e.g. three-dimensional mapping of the temperature in the mesosphere [11].

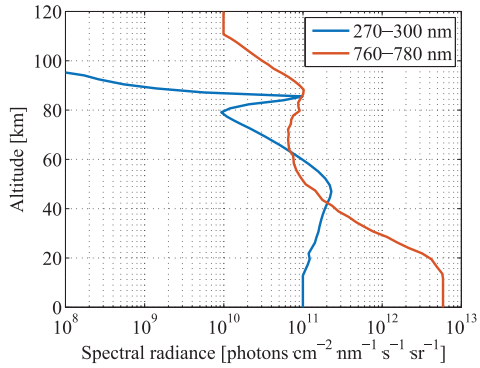

Figure 3.2: Altitude versus radiance in the detection bands of the limb instrument. Image from paper B.

Figure 3.2 shows the radiance from the atmospheric limb in the wavelength bands of the limb instrument. Signals from atmospheric airglow and noctilucent clouds are present at altitudes 70-110 km that cause bumps on the profiles, which are otherwise dominated by Rayleigh scattering. The radiance in this region is taken as input to equation 2.29, which

is used to calculate the required signal-to-noise ratio of the limb instrument. With back-illuminated CCDs operating at -20° C, it was concluded that an entrance pupil diameter of at least 32 mm was needed to provide the required signal-to-noise ratio in all channels. Since vertical resolution is highly prioritized over horizontal resolution, it is possible to apply on-chip binning to drastically increase the sensitivity. This is also beneficial when considering the limited downlink bandwidth used for downloading data from all channels. Exposure times between 3-5 s were assumed to avoid image smearing due to the changing scene during flight. To avoid risks associated with moving parts on the satellite platform, no mechanical shutter will be used to block the light during the readout. This implies that the an anti-smearing algorithm must be applied in the data post-processing.

MATS is the first in a series of payloads that use the Innosat platform [89], which is a general-purpose satellite platform for LEO satellite missions. With a relatively small size (70 cm×60 cm×85 cm) and a total mass of 40-50 kg, the satellite becomes compatible for a shared (”piggyback”) launch, which reduces the mission cost drastically. MATS will fly in a sun-synchronous dusk-dawn orbit with the sun always facing the same side of the spacecraft. This allows for a single fixed solar panel to be used.

3.2 ISMAR

The International Submillimetre Airborne Radiometer (ISMAR) is a multi-channel instrument at 118-874 GHz for measurements of ice clouds [90, 91]. It is operated by UK Met Office and is used as a precursor for the upcoming Ice Cloud Imager (ICI) instrument [92]. Ice clouds have been shown to play an important role in climate- and weather prediction, but has not been studied in much detail in previous missions, which are limited in terms of horizontal resolution due to their limb-viewing geometry [13, 93]. ICI will be one of the instruments on board the Metop-SG-B satellite [94], which is the second generation of Metop satellites with a planned launch in 2022. It is the first instrument ever that specializes in measuring ice clouds.

As a precursor to this mission, ISMAR’s seven channels are similar in frequency to the ICI and will be used to test retrieval algorithms as well as calibration/validation schemes [90]. The ISMAR instrument is housed inside an AAM BAe-146 aircraft, which has a rotating mirror mounted on its outside to enable sweeping of the instrument’s beams across the observation targets – see Figure 3.3. The instrument does not have any common focusing reflector, but instead uses individual lenses in front of the horn antennas of each receiver channel. Hence, the beam footprint on the observation target of each channel varies and depends on the operation wavelength and the size of the lenses. Schottky mixer receivers operating at room temperature are used for all channels, which are distributed in a cluster around the 118 GHz channel – see Figure 3.4.

The final addition to ISMAR were two identical and linearly polarized 874 GHz heterodyne receivers, which are oriented to enable detection of signals of orthogonal polarizations – see Figure 3.3. The requirements in terms of operational bandwidth, radiation pattern FWHM and DSB noise temperature are given in Table 3.2. To achieve beams with main lobes FWHM smaller than 5°, dielectric lenses were placed in front of the horns. These also

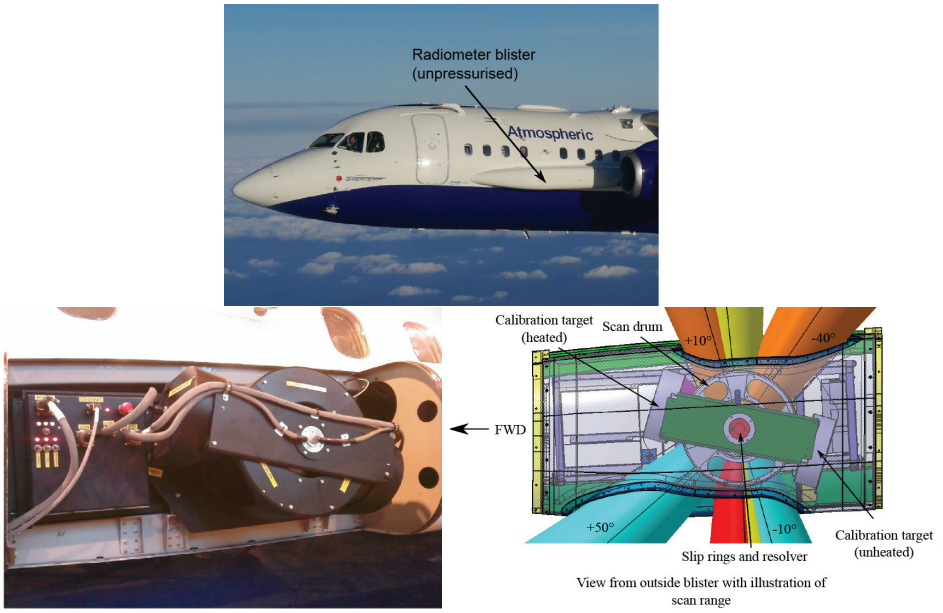

Figure 3.3: Overview of ISMAR. Top image: AAM BAe-146 aircraft. Bottom images: drum containing rotating mirror and calibration loads, sweep/calibration cycle of the instrument's beams. Pictures from [90].

channel	polarization [-]	ν [GHz]	FWHM [°]	$T_{rec,DSB}$ [K]
receiver 1	V	874 ± 5	5	4000
receiver 2	H	874 ± 5	5	4000

Table 3.2: Requirements for the 874 GHz receivers of ISMAR.

serve as protection from the external environment, c.f. Figure 3.4.

3.3 STEAMR

The Stratosphere-Troposphere Exchange And climate Monitor Radiometer (STEAMR) is a satellite-borne instrument for atmospheric research in the upper troposphere/lower stratosphere (UTLS, 5-25 km), which has been proposed as part of two separate missions: Process Exploration through Measurement of Infrared and millimeter-wave Emitted Radiation (PREMIER) [95, 96] and the Atmospheric Limb Sounding Satellite (ALISS) [97]. Focus in this thesis is on the version of STEAMR that was proposed for PREMIER, which had an optical system [98–101] that was more advanced than the one suggested for ALISS.

STEAMR was designed to measure molecular emissions from the UTLS. This region

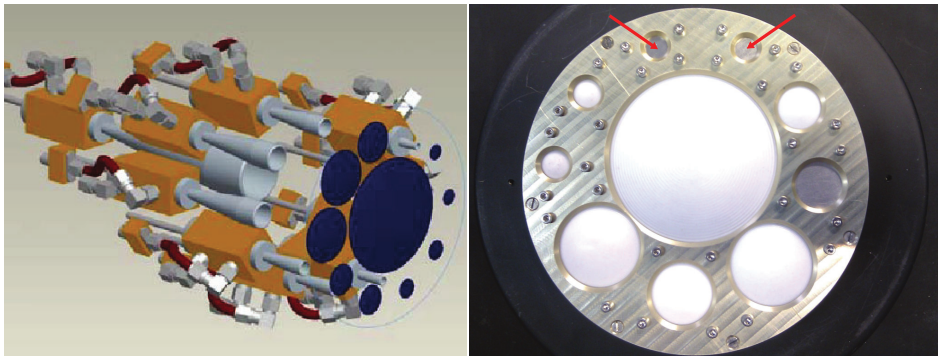

Figure 3.4: CAD model showing cluster of receivers for ISMAR (left) and mounting frame for the receiver lenses (right). The red arrows indicate the positions of the two channels at 874 GHz. Pictures from [91].

is important in terms of radiative balance (i.e. the amount of heat being trapped or escaping the atmosphere) and this is determined by the amount and distribution of various trace/greenhouse gases (e.g. H_2O, O_3, NO_2, etc.). This has an effect on temperatures and winds in the region, but also at the surface of the Earth. In fact, the chemical composition of the atmosphere in this region and the interaction with climate has been identified as an major uncertainty of climate change modeling [102]. More specifically, to refine current models, it is necessary to measure the distribution and transport of trace gases with higher resolution as these change rapidly in time and space. This is one of the main scientific goals of STEAMR.

The instrument uses 14 polarization-interleaved beams in a limb-viewing configuration to observe the atmosphere at altitudes 6-26 km. Detection is facilitated by 14 identical Schottky mixer receivers at 323-355 GHz and autocorrelator back-ends (10 MHz resolution). This choice of frequency makes it possible to see through clouds while still being able to study important trace gases in the atmosphere. The vertical resolution is prioritized over horizontal, which allows for a more compact elliptical off-axis Ritchey-Chrétien telescope (1.6× 0.8 m primary reflector) to be used – see Figure 3.5. Sampling density in the vertical direction is 1.5 km at altitudes below 16.5 km and 2.0 km above. Having this many beams greatly increases the spatial and resolution of STEAMR compared to its single-beam predecessors [93], which have to wobble up and down to cover the same atmospheric scene.

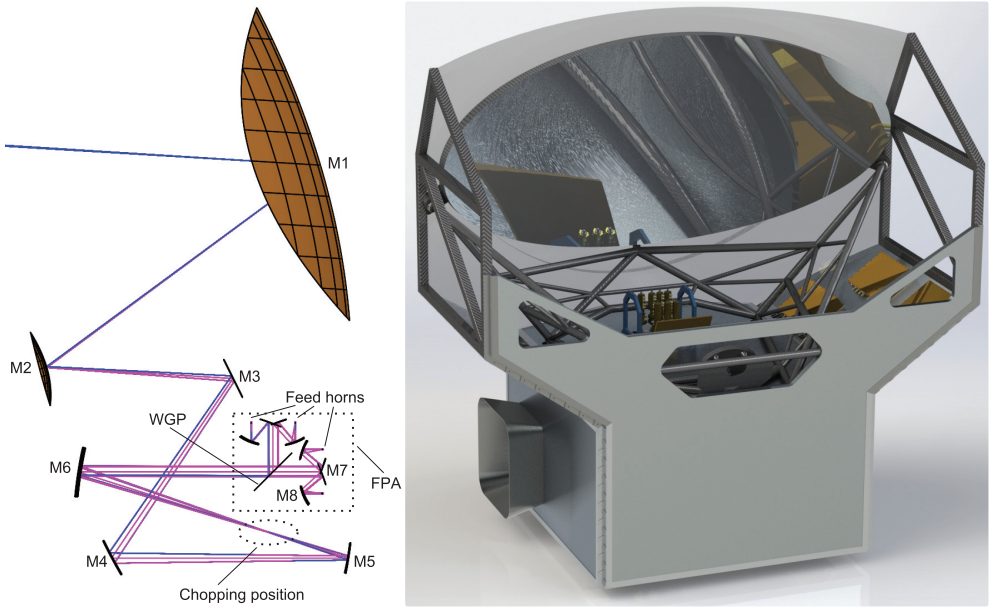

Figure 3.5: Optical system of STEAMR (left) and a CAD model of the complete STEAMR payload (right).

Chapter 4

Analysis methods

This chapter describes methods to design and analyze optical systems. The purpose is to give a theoretical background to the test methods that are used in Chapter 5. Several design examples related to papers A-F are given.

4.1 Geometrical optics

When the components of an optical system are large, the propagation of electromagnetic waves can be approximated with a geometrical wavefront. The shape and direction of the geometrical wavefront is described in terms of rays, which travel in a constant direction unless the refractive index n changes. In free space in the absence of charges and with an electric field $\mathbf{E}$ varying in time as $e^{-i\omega t}$, Maxwell's equations reduce to the Helmholtz equation:

$$\left(\nabla^2 + k^2\right)\mathbf{E} = 0, \tag{4.1}$$

where the wavenumber k is equal to $2\pi/\lambda$. In the geometrical optics approximation, the solutions to 4.1 are written

$$\mathbf{E} = u(x, y, z)e^{-ik_0 S(x,y,z)}, \tag{4.2}$$

where $S(x, y, z)$ is a scalar function known as the eikonal and represent the (geometrical) wavefront. In the limit $\lambda_0 \to 0$ and with a $n(x, y, z)$ varying slowly, the eikonal equation can be derived [103]:

$$S(x, y, z) = n(x, y, z), \tag{4.3}$$

which constitute the foundation for geometrical optics. Rays and wavefronts are used for analyzing optical systems in the geometrical optics approximation. Snell's law follows from the eikonal equation and describes how rays bend as the refractive index changes in the interface between two media:

$$n_1 \sin\theta_1 = n_2 \sin\theta_2, \tag{4.4}$$

where θ_1 and θ_2 are the angles of incidence measured from the surface normal. In the paraxial approximation, θ_1 and θ_2 are small and equation 4.4 becomes $n_1\theta_1 \approx n_2\theta_2$.

Axial lens system

The five third-order (Seidel) aberrations [24] – spherical aberration, coma, astigmatism, field curvature and distortion – are essential to any successful optical design with axial symmetry. The design for the MATS nadir camera was based on three co-axial spherical lenses that were optimized to minimize third-order aberrations. Such a design is often referred to as a Cooke triplet. Figure 4.1 shows the layout of the design with the design parameters R_1-R_6, x_{23}-x_{78} and r_3 (r_1,r_2, r_4 and x_{89} follow for a given set of design parameters), which are the radii for the spherical lenses, the lens thicknesses, the lens separation and the aperture radii. In addition to the geometrical parameters, the glass types of the three lenses are chosen to correct for chromatic aberrations (axial and lateral).

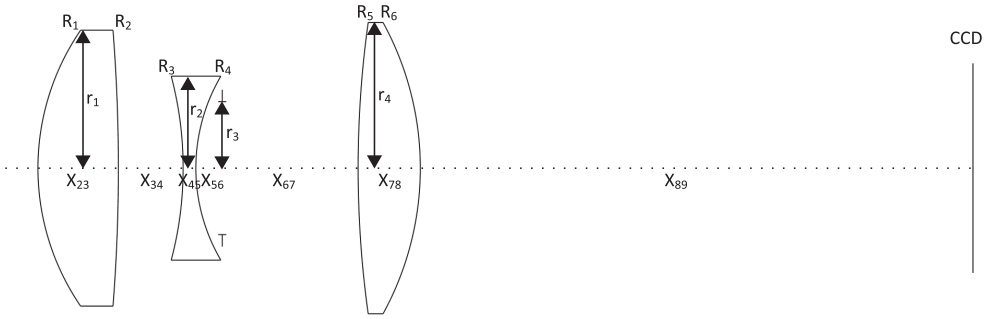

Figure 4.1: Layout of the three-lens design for the MATS nadir camera.

The design had an entrance pupil diameter of 15 mm and a FoV of 24.4° × 6.1°. The location of an imaged point source at infinity with field angle θ can be approximated by

$$h_i = f_{eff}\,\theta, \tag{4.5}$$

where f_{eff} is the effective focal length of the system. An effective focal length of f_{eff} = 50 mm was chosen, giving an f-number of 3.3.

By placing the aperture stop on the middle lens and tracing only the marginal- and chief rays, a thin-lens solution (assuming zero thickness for all lenses) that corrects for the Seidel aberrations was obtained. The middle lens used a Schott N-F2 glass (flint,low Abbe number [24]) whereas the remaining lenses used Schott N-SK16 glass (crown, high Abbe number). The thin-lens design was implemented in an optical simulation software (Zemax - Opticstudio [104]) where sequential ray tracing (light path determined by the user) is determined by the user. A manufacturable solution was obtained by imposing non-zero lens thicknesses and optimizing for all variables (including stop position) while minimizing the aforementioned aberrations. Optical performance was analyzed in terms of wavefront errors, which describes the optical path difference between the calculated geometrical wavefront in the image plane to a spherical wavefront [24].

Figure 4.2 shows the simulated encircled energy plot of the MATS nadir camera compared to that of an ideal $f/3.3$ optic. The FoV of 24.4° is rather large for a $f/3.3$ Cooke triplet, which limits the resolution considerably. However, with relatively modest resolution requirements

(80% encircled energy within a radius of ~250 µm – see chapter 3.1), the performance is still satisfactory.

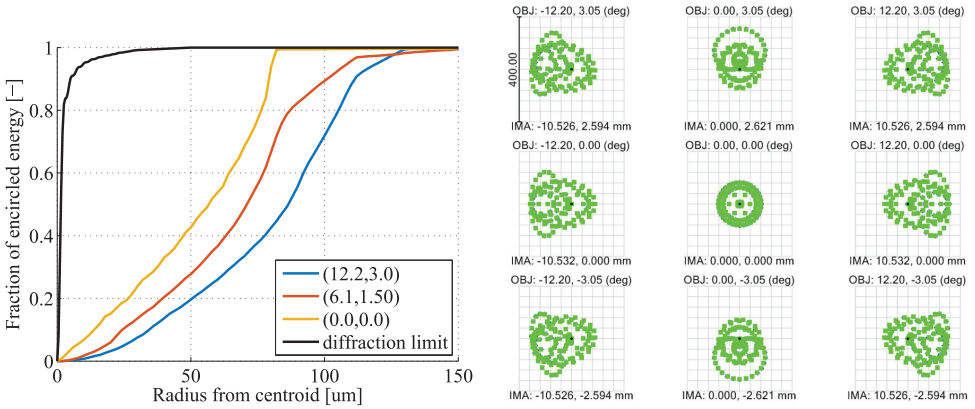

Figure 4.2: Encircled energy versus half width from the centroid (left) and spot diagrams across the FoV (right) for the MATS nadir camera.

Off-axis reflectors

The shape of mirrors in off-axis systems is often based on conic sections, which are generated from the section of a cone being cut by a plane at an angle. Depending on the angle, the sections are either circles, parabolas, ellipses or hyperbolas and can be expressed by the following expression:

$$y^2 = 2R - (K+1)z^2, \tag{4.6}$$

where R is the on-axis radius of curvature and K the conic constant [105]. The corresponding two-dimensional surfaces (spheres, paraboloids, ellipsoids and hyperboloids) are obtained by rotating the conic section about the z-axis and can be described by the following expression in cylindrical coordinates [106]:

$$z = \frac{Cr^2}{1 + \sqrt{1 - (1+K)C^2r^2}}, \tag{4.7}$$

where the curvature is defined by $C = 1/R$. Table 4.1 and Figure 4.3 summarize the conic sections with corresponding values of K and eccentricity e (defined as $e = -K^2$).

With typically just a few optical surfaces to correct for aberrations, reflective systems are often more limited in terms of FoV than refractive systems with corresponding f-numbers. A classical Cassegrain telescope consists of a parabolic primary mirror and a hyperbolic secondary mirror. It is corrected for spherical aberrations, but is limited by coma for large field angles. This problem is addressed in the Ritchey-Chrétien design, which uses two hyperbolic mirrors to correct for both spherical aberration and coma. However, if off-axis sections of the

Conic section	K	e	b	Equation
Circle	0	0	a	$z^2 + y^2 = a^2$
Ellipse	> -1	c/a	$\sqrt{a^2 - c^2}$	$(z/a)^2 + (y/b)^2 = 1$
Parabola	-1	1	∞	$z^2 = 4ay$
Hyperbola	< -1	c/a	$\sqrt{c^2 - a^2}$	$(z/a)^2 - (y/b)^2 = 1$

Table 4.1: Conic sections with conic constants K, eccentricity e, semiminor axis b and equation expressed in terms of the half-foci distance c and half-vertex separation a in a Cartesian frame.

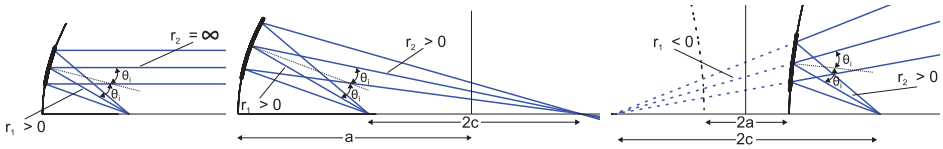

Figure 4.3: Off-axis conic sections. From left to right: parabola, ellipse, hyperbola.

mirrors are used to avoid the obscuration of the primary mirror, aberrations increase. Figure 4.4 shows on- and off-axis implementations for $f/7.3$ telescopes (same as for the MATS limb telescope, c.f. paper A) based on the classical confocal Cassegrain and Ritchey-Chrétien designs. The off-axis versions were generated by simply taking off-axis sections of the axially symmetric on-axis designs.

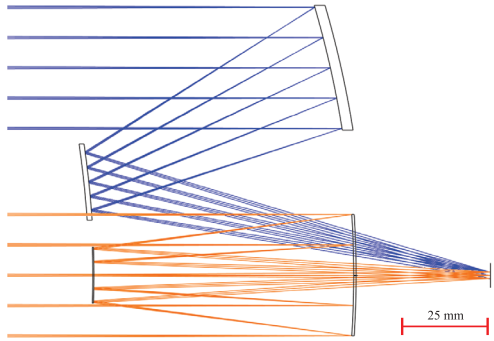

Figure 4.4: On- and off-axis $f/7.3$ (D = 35 mm) Cassegrain designs. There is no obvious visual difference between the Cassegrain and corresponding Ritchey-Chrétien design, wherefore the latter was omitted from the figure.

The optical performance of the Cassegrain and Ritchey-Chrétien designs are summarized in Figures 4.5-4.6, which show spot diagrams and modular transfer function (MTF) vs. spatial frequency [106]. As can be seen, the on-axis designs have excellent performance within 0.4° × 0.4°, but soon become drastically limited for larger field angles. The performance of the off-axis versions are seriously degraded within the same FoV.

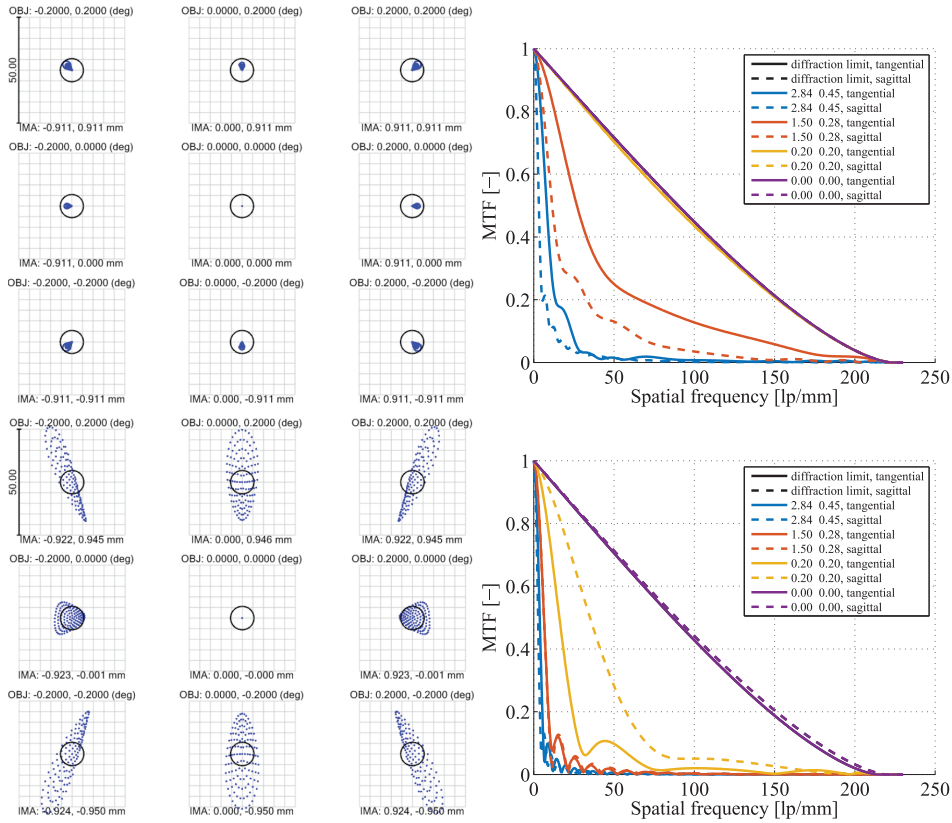

Figure 4.5: Performance of on- (first row) and off-axis (second row) $f/7.3$ (D = 35 mm) Cassegrain designs. Left column: spot diagrams over $0.4° \times 0.4°$ with Airy disk at 600 nm. Right column: MTF vs. spatial frequency for field angles (0-2.84°,0-0.45°).

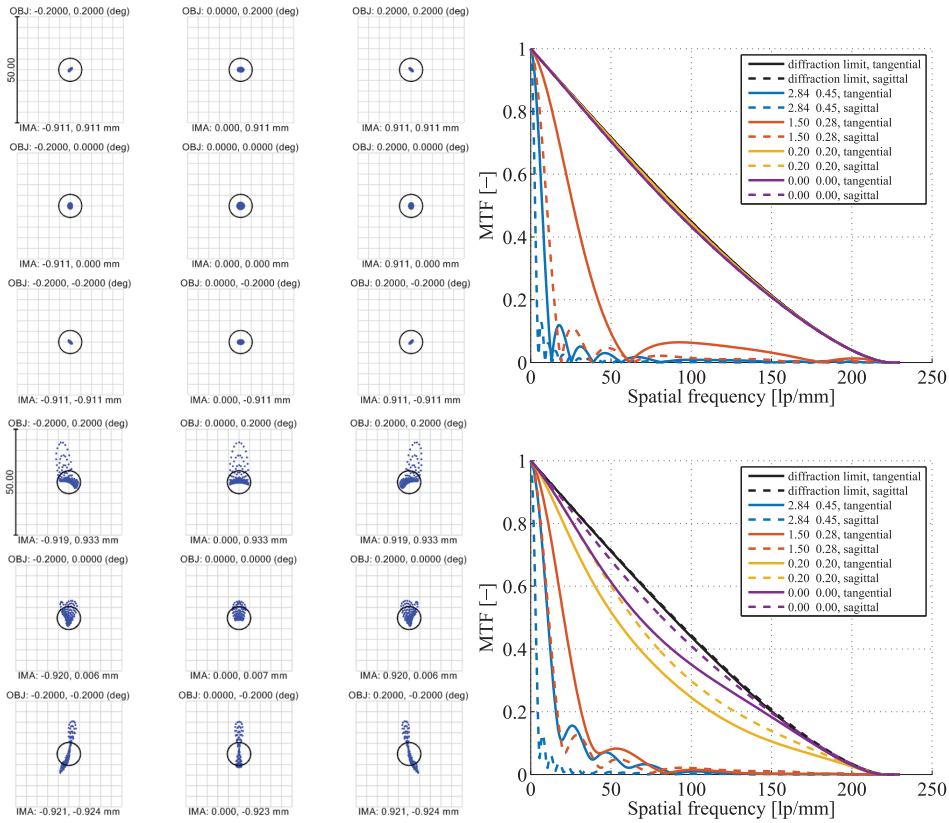

Figure 4.6: Performance of on- (first row) and off-axis (second row) $f/7.3$ (D = 35 mm) Ritchey-Chrétien. Left column: spot diagrams over 0.4° × 0.4° with Airy disk at 600 nm. Right column: MTF vs. spatial frequency for field angles (0-2.84°,0-0.45°).

Unless corrected for, an off-axis telescope has tilted tangential and sagittal image planes, which causes second-order linear astigmatism [107] that drastically limits the FoV – see Figure 4.7. It is possible to eliminate linear astigmatism by introducing the angle between the major axes of the conic sections as a design variable. For a confocal N-mirror system, the linear astigmatism can be eliminated by imposing the following condition [108]:

$$\sum_{p=1}^{N-1}\left[(1+m_p)\tan i_p \prod_{q=p+1}^{N} m_q)\right] + (1+m_N)\tan i_N = 0, \tag{4.8}$$

where m_p and i_p denote the focal length and reflection angle of mirror p. For a conic section mirror, the focal length is given by the ratio of r_1 and r_2 (c.f. Figure 4.3). For a two-mirror system, equation 4.8 is reduced to

$$(1+m_1)m_2\tan i_1 + (1+m_2)\tan i_2 = 0. \tag{4.9}$$

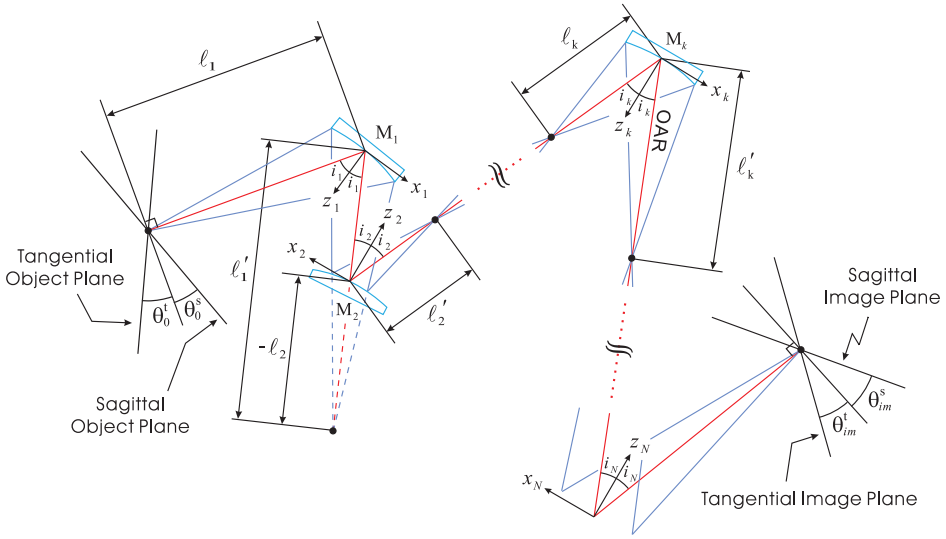

Figure 4.7: General off-axis N-mirror system with tilted tangential and sagittal image planes. Image from [108].

Figure 4.8 shows the design resulting after a tilt between the major axes of the parent conic sections was introduced to fulfill equation 4.9. Figure 4.9 shows the performance of the design. As can be seen, the performance is nearly identical – and slightly better at larger field angles – to that of the on-axis Cassegrain design.

Although linear astigmatism can be removed by employing equation 4.9, there are still higher-order aberrations left, which limit the performance at large field angles. These aberrations can be decreased substantially by replacing the conic section mirrors with free-form

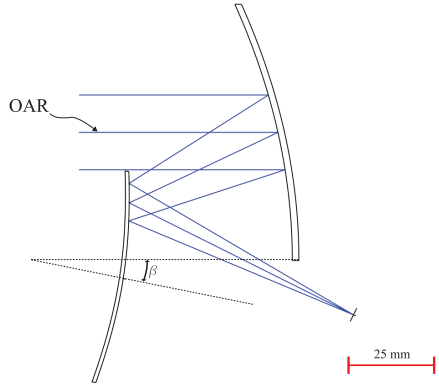

Figure 4.8: Confocal off-axis $f/7.3$ (D = 35 mm) design based on tilted conic section mirrors to correct for linear astigmatism. Mirrors sizes have been exaggerated to show the tilt angle β between the major axes of the parent bodies. The optical axis ray (OAR) is highlighted.

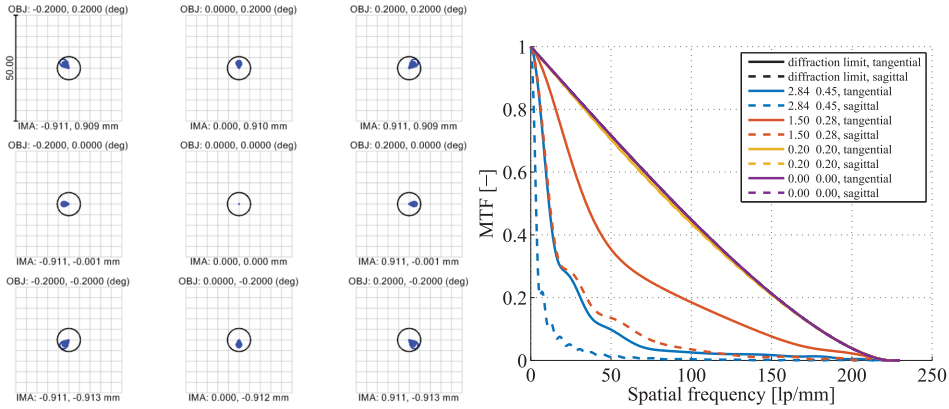

Figure 4.9: Performance of confocal off-axis $f/7.3$ (D = 35 mm) design based on tilted conic section mirrors to correct for linear astigmatism. Left figure: spot diagrams over $0.4° \times 0.4°$ with Airy disk at 600 nm. Right figure: MTF vs. spatial frequency for field angles (0-2.84°,0-0.45°).

mirrors that have an arbitrary number of parameters to describe their (non-symmetric) surfaces. This makes it possible to achieve optical performance that would otherwise require more mirrors. Advances in single point diamond turning (SPDT) technology have paved the way for free-form designs, which are therefore becoming increasingly popular for systems where the mirror diameter is below ~500 mm. Free-form systems are designed using numerical optimization in ray-tracing software. As a starting point for the optimization, the conic section mirrors can be expanded around the reflection points of the optical axis ray (OAR – see 4.8) and with the z-axis perpendicular to the surface [107]. The mirror surfaces are

expressed in the following polynomial basis:

$$z(x,y) = \sum_{i=1}^{N} A_i E_i(x,y), \tag{4.10}$$

where A_i are real coefficients and $E_1 = x$, $E_2 = y$, $E_3 = x^2$, $E_4 = xy$, $E_5 = y^2$, $E_6 = x^3$ ... $E_N = y^N$. Coefficients A_i with odd powers of x are nulled to preserve symmetry in the yz-plane. By optimizing the coefficients of the two mirror surfaces with respect to spot size diameter, an off-axis free-form design corrected for linear astigmatism is obtained – see Figure 4.10. Compared to the on-axis Cassegrain and off-axis conic section design, the off-axis free-form design has a much improved performance over large field angles – see Figure 4.11.

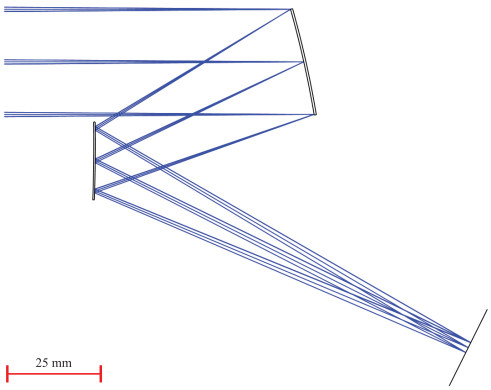

Figure 4.10: Off-axis $f/7.3$ (D = 35 mm) design based on free-form mirrors.

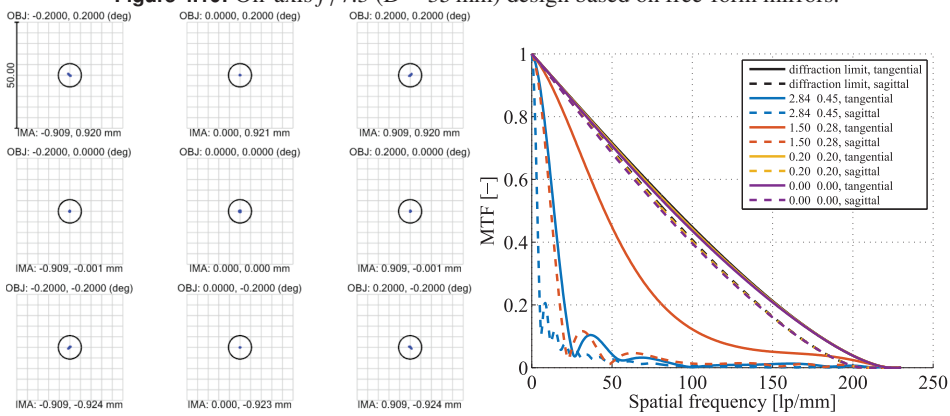

Figure 4.11: Performance of off-axis $f/7.3$ (D = 35 mm) design based on free-form mirrors. Left figure: spot diagrams over 0.4° × 0.4° with Airy disk at 600 nm. Right figure: MTF vs. spatial frequency for field angles (0-2.84°,0-0.45°).

The same process that was outlined above was used to design the free-form three-mirror

$f/7.3$ (D = 35 mm) telescope for MATS (see paper A). Using equation 4.8, the condition for eliminating linear astigmatism becomes:

$$(1 + m_1)m_2\, m_3\, \tan i_1 + (1 + m_2)\, m_3 \tan i_2 + (1 + m_3)\, \tan i_3 = 0. \tag{4.11}$$

Although a three-mirror system is generally more challenging to align, the extra design parameters could be used to achieve diffraction-limited performance over a much larger FoV while accommodating six CCD sensors and network of beamsplitters and filters. Figures 4.12 and 4.13 show the layout of the design and optical performance over a much larger FoV than the two-mirror designs.

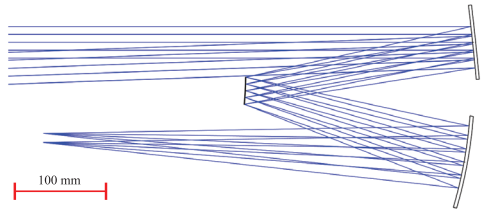

Figure 4.12: Off-axis $f/7.3$ (D = 35 mm) design for MATS based on free-form mirrors. The mirror apertures have been increased to allow for a FoV larger than what was required for the instrument.

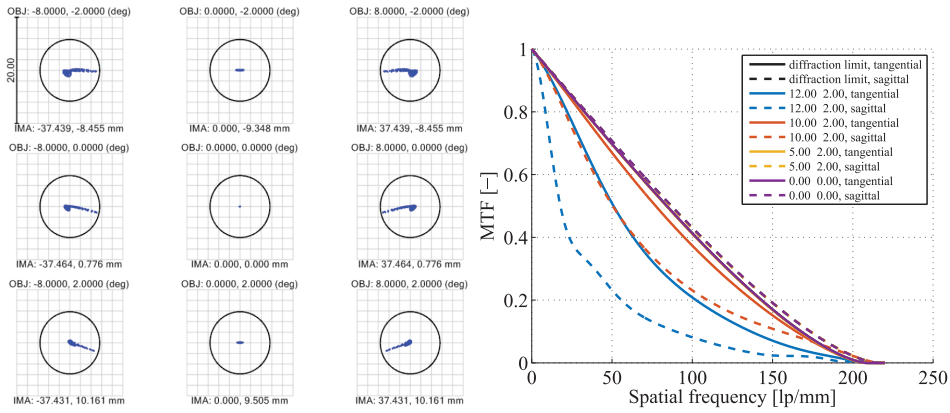

Figure 4.13: Performance of the MATS off-axis $f/7.3$ (D = 35 mm) design based on free-form mirrors. Left figure: spot diagrams over 16° × 4° with Airy disk at 600 nm. Right figure: MTF vs. spatial frequency for field angles (0-12°,0-2°).

Non-sequential ray tracing

In the previous examples, sequential ray tracing was used since the light path through the system was determined a-priori. This stands in stark contrast to non-sequential ray tracing, where rays are scattered and attenuated in a more realistic manner. Non-sequential ray tracing

was used in paper B to analyze the stray light rejection performance of the MATS limb instrument. The non-sequential stray light model was defined in Zemax - Opticstudio using CAD models to represent the main structures inside the instrument – see Figure 4.14. Every major aspect of the instrument, e.g. filter and beamsplitter transmission data, surface reflectance, surface scattering characteristics, were included to obtain accurate results. Computation time depends mainly on the number of rays that are traced, how little energy each ray is allowed to have before it is terminated and the complexity of the structures. To cover field angles across the entire forward hemisphere for several wavelengths in the sensitive region of the CCD sensors becomes a time-consuming process. However, even though the total simulation time for a given instrument configuration is several days, the effort is smaller than a corresponding measurement campaign and can provide insight into critical paths and regions inside the instrument.

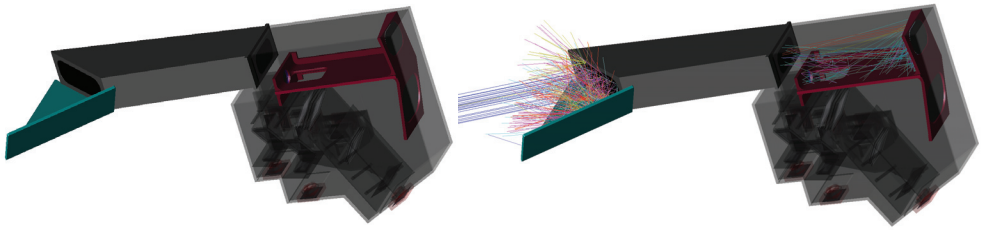

Figure 4.14: Stray light model showing the layout without (left) and with (right) scattered rays at 763 nm.

The front baffle was covered on the inside with a new type of extremely black coating (Vantablack S-VIS [109]). It consists of densely packed vertically aligned carbon nanotubes, which efficiently traps incident light, resulting in a reflectance of 0.2-0.6% between 270-776 nm. A set of measured BRDF data was used to model scattering of Vantablack inside the baffle. This means that each ray that hits the coated surface is split into several rays (typically 10) with less total energy than the original ray. The total energy and directions of the scattered rays follow a random distribution given by the BRDF data. The surface is highly Lambertian – see Figure 4.15.

Figure 4.15: Scattering from a surface coated with Vantablack S-VIS (left) and a surface coated with an ideal Lambertian scatterer (right).

4.2 Physical optics

This section describes design methods where the wave nature of light is factored in, but where approximations are made to avoid complex and computationally heavy full-wave solutions of Maxwell's equations such as the finite element method (FEM) and method of moments (MoM) [110].

Diffraction effects are often more significant for optical systems in the THz regime since components are small compared to the wavelengths. Unlike geometrical optics, where optical components are relatively large, it is no longer sufficient to represent the propagation of light in these systems using ray tracing. Gaussian beam mode analysis is a powerful tool, which can used to model beams that expand due to diffraction. The material presented here covers the essential aspects of Gaussian beam mode analysis and is largely based on material that can be found in [38, 111].

As for a plane wave, it is assumed that the electric and magnetic fields are mutually perpendicular and perpendicular to the axis of propagation, which is here chosen to be the z axis. Neglecting time dependence, the ansatz

$$E(x, y, z) = u(x, y, z)e^{-ikz} \tag{4.12}$$

can be inserted into equation 4.1 to yield the reduced wave equation:

$$\frac{\partial^2 u}{\partial x^2} + \frac{\partial^2 u}{\partial y^2} + \frac{\partial^2 u}{\partial z^2} - 2ik\frac{\partial u}{\partial z} = 0. \tag{4.13}$$

Assuming that the variation of the amplitude of u along the z axis is small over a distance similar to one wavelength and that the axial variation will be small compared to the variation transverse to z, the third term in equation 4.13 can be neglected. The fundamental Gaussian beam mode is axially symmetric and can conveniently be written in cylindrical coordinates:

$$E(r, z) = \left(\frac{2}{\pi w^2}\right)^{0.5} \exp\left(\frac{-r^2}{w^2} - ikz - \frac{i\pi r^2}{\lambda R} + i\phi_0\right). \tag{4.14}$$

The parameter w is called the beam width and corresponds to a beam radius where the amplitude of the E-field has dropped by a factor of $1/e$ from its maximum value. R is the radius of curvature of the equi-phase surface. In spherical coordinates, the electric field can be written as [112]:

$$E(R, \theta) = \sqrt{\frac{2\pi\omega_0^2}{R\lambda}} \cos\theta \exp\left(-(\pi\omega_0/\lambda)^2 \sin^2\theta + j\pi/2 - jkR\right) \tag{4.15}$$

As can be seen in Figure 4.16, w attains a minimum value referred to as the beam waist w_0. The parameter ϕ_0 represents a phase shift, which is often called the Gouy phase shift. Equations 4.16, 4.17 and 4.18 can be used to express w, R and ϕ_0 as a function of z, w_0 and λ:

$$R = z + \frac{1}{z}\left(\frac{\pi w_0^2}{\lambda}\right)^2 = z + \frac{z_c^2}{z} \tag{4.16}$$

$$w = w_0\left[1+\left(\frac{\lambda z}{\pi w_0^2}\right)^2\right]^{0.5} = w_0\left[1+\left(\frac{z}{w_c}\right)^2\right]^{0.5} \tag{4.17}$$

$$\phi_0 = \arctan\left(\frac{\lambda z}{\pi w_0^2}\right) = \arctan\left(\frac{z}{z_c}\right), \tag{4.18}$$

where $z_c = \frac{\pi w_0^2}{\lambda}$ is the confocal distance. These are the basic equations needed for analyzing an optical system using fundamental Gaussian beam modes. Although higher order modes might reveal more details about the performance of the analyzed system, it is often sufficient to only consider the fundamental mode for a first-order design that can later be analyzed using more sophisticated approaches. It is important to note that the approximation of Gaussian beam modes does not work for arbitrarily small beam waists. For values of w_0 below 0.9λ, the accuracy degrades gradually and comes to a complete failure at approximately 0.2λ or less [113].

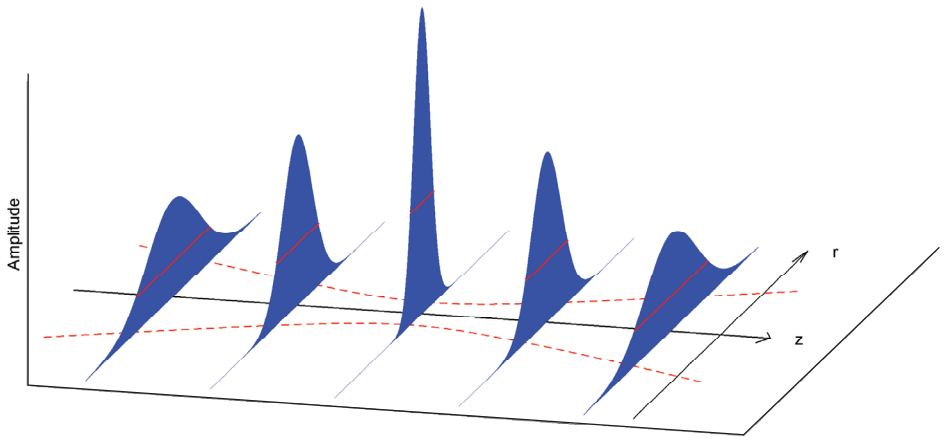

Figure 4.16: Illustration of a propagating Gaussian beam. The $1/e$ level of the electric field is highlighted in red.

A system consisting of an arbitrary number of optical components can be described using two-port theory. To do this, equation 4.15 is re-written as

$$E(r,z) = A(z)\exp\left[\frac{-ikr^2}{2q(z)}\right]\exp(-ikz). \tag{4.19}$$

The function $q(z)$ is called the complex beam parameter and is defined as

$$q(z) = \left(\frac{1}{R} - \frac{i\lambda}{\pi w^2}\right)^{-1}. \tag{4.20}$$

Equations 4.16, 4.17, and 4.18 can then be written as

$$w(z) = \left[\frac{\lambda}{\pi \mathrm{Im}(-1/q(z))}\right]^{0.5}, \tag{4.21}$$

$$R(z) = \left[\mathrm{Re}\left(\frac{1}{q(z)}\right)\right]^{-1}, \tag{4.22}$$

$$\phi_0(z) = \arctan\left[\frac{\mathrm{Re}(q(z))}{\mathrm{Im}(q(z))}\right]. \tag{4.23}$$

As the beam propagates through an optical system, $q(z)$ changes and transforms to

$$q_{out} = \frac{Aq_{in} + B}{Cq_{in} + D}, \tag{4.24}$$

where A, B, C and D are elements of a 2×2 matrix that is obtained by cascading an arbitrary number N of ray transfer matrices:

$$\begin{bmatrix} A & B \\ C & D \end{bmatrix} = \prod_{n=k}^{N} M_n. \tag{4.25}$$

The ray transfer matrices representing a thin lens and propagation of a distance L are given by

$$M_{\text{propagation}} = \begin{bmatrix} 1 & L \\ 0 & 1 \end{bmatrix}, \tag{4.26}$$

and

$$M_{\text{thin lens}} = \begin{bmatrix} 1 & 0 \\ -1/f & 1 \end{bmatrix}. \tag{4.27}$$

Ray transfer matrices were used in papers C-D. In the former, a setup with two focusing mirrors (modeled as thin lenses) was used to build a Y-factor measurement setup (see Figure 11, paper C). In order to minimize the impact on the measured signal from temperature gradients on the thermal loads, the system was designed to have a waist between the flat load selector and the loads in order to illuminate a larger part of the loads. The total ray transfer matrix from the waist of the feed horn to the plane in between the load selector and load becomes:

$$M_{tot} = \begin{bmatrix} 1 & d_4/2 \\ 0 & 1 \end{bmatrix}\begin{bmatrix} 1 & 0 \\ -1/f_3 & 1 \end{bmatrix}\begin{bmatrix} 1 & d_3 \\ 0 & 1 \end{bmatrix}\begin{bmatrix} 1 & 0 \\ -1/f_2 & 1 \end{bmatrix}\begin{bmatrix} 1 & d_2 \\ 0 & 1 \end{bmatrix}\begin{bmatrix} 1 & 0 \\ -1/f_1 & 1 \end{bmatrix}\begin{bmatrix} 1 & d_1 \\ 0 & 1 \end{bmatrix}, \tag{4.28}$$

where the distances d_{1-4} are shown in Figure 4.17. If $d_2 = f_1 + f_2$ and the load selector mirror is flat ($f_3 = \infty$), equation 4.28 is simplified to:

$$M_{tot} = \begin{bmatrix} -f_2/f_1 & 0 \\ 0 & -f_1/f_2 \end{bmatrix}, \tag{4.29}$$

where $d_3 + d_4/2 = f_2$ and $d_1 = f_1$ is assumed. At the location of the feed horn waist, the complex beam parameter is $q_{in} = \frac{i\pi w^2}{\lambda}$. Applying equation 4.24 gives

$$q_{out} = \frac{-f_2/f_1 q_{in} + 0}{0 - f_1/f_2} = \left(\frac{f_2}{f_1}\right)^2 q_{in}. \tag{4.30}$$

Hence, independent of frequency, the setup produces an output waist at a distance f_2 from the M2 mirror that has a beam width of $w_{out} = f_2/f_1 w_{in}$. The propagation of the -40 dB contour of Gaussian beams from horns at different frequencies are illustrated in Figure 4.17. The fraction of the total energy in the beam that is intercepted by an element of a given size is called the edge taper, which is defined as:

$$\begin{aligned} T_e &= \frac{P(r)}{P(0)} = e^{-2\left(\frac{r}{w}\right)^2} \\ T_{e,dB} &= -10\log_{10}(T_e). \end{aligned} \tag{4.31}$$

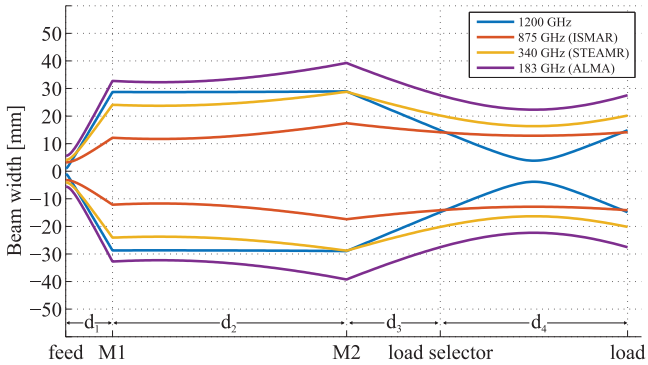

Figure 4.17: Propagation of fundamental Gaussian beams through a frequency-independent optical setup for Y-factor measurements. Distances and mirrors are denoted d_{1-4} and M_{1-3}. The lines indicate the -40 dB contour for different feed horns.

For a general system consisting of N reflectors, the condition frequency independence states that the element B in the total ray transfer matrix must equal zero [114]. This is equivalent with having a total phase shift equal to an integer number of π. This was used when designing the optics of STEAMR, where a total of 8 mirrors was used for each of the 14 feed horns (see paper F). This system employed astigmatic mirrors to correctly illuminate the 1.6 m × 0.8 m primary aperture. To achieve a frequency-independent illumination, two orthogonal Gaussian beams (that both had an accumulated phase shift equal to 2π) were analyzed in parallel [115] – see Figure 4.18

Although the methods outlined above work well to design these two systems, it should be noticed that the fundamental Gaussian beam modes assume axial symmetry, which is broken for off-axis systems. To investigate the performance in greater detail, the analysis software GRASP [116] was used to analyze nominal performance as well as mechanical tolerances of off-axis systems (see paper F). This software relies on physical optics methods where an incident field on a perfectly or partially conducting reflector induces surface currents, which are used to calculate the scattered field. The total electric field $\mathbf{E}$ around a reflector is written as

$$\mathbf{E} = \mathbf{E}^i + \mathbf{E}^s, \tag{4.32}$$

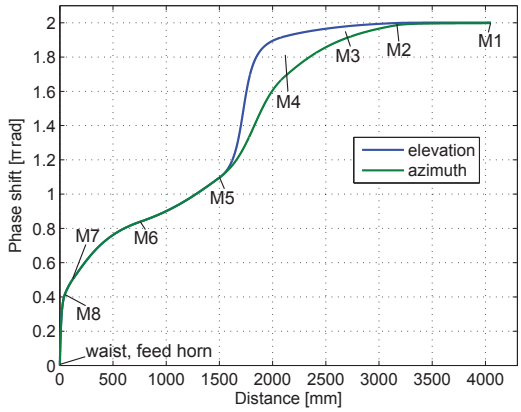

Figure 4.18: Phase shift for two perpendicular Gaussian beams (elevation and azimuth) propagating from the feed horn to the elliptical primary aperture. The reflector positions (M1-M8) are highlighted.

where $\mathbf{E}^i$ and $\mathbf{E}^s$ denote the incident and scattered fields, respectively [117]. The surface currents on a finite size curved reflector are calculated by dividing the reflector into several smaller parts where the currents on each part are approximated by the currents of a plane reflector of infinite size. The surface current $\mathbf{J}^e$ due to an incoming magnetic field $\mathbf{H}^i$ is given by

$$\mathbf{J}^e = 2\hat{\mathbf{n}} \times \mathbf{H}^i, \tag{4.33}$$

where $\hat{\mathbf{n}}$ is the surface normal unit vector. By numerically integrating over all surface currents, the electric and magnetic vector potentials $\mathbf{A^e}$ and $\mathbf{A^m}$ at an arbitrary point in space $\mathbf{r}$ can be calculated. These are then used to determine the electric and magnetic fields. In a system consisting of a series of consecutive reflectors, the calculated scattered field from a reflector is used as the incident field for the following reflector. The far fields are given by

$$\mathbf{E}(\mathbf{r})_{far} = \lim_{r\to\infty} \mathbf{E}(\mathbf{r})\, k\, r\, e^{ikr} \tag{4.34}$$

and

$$\mathbf{H}(\mathbf{r})_{far} = \lim_{r\to\infty} \mathbf{H}(\mathbf{r})\, k\, r\, e^{ikr}, \tag{4.35}$$

where $r = |\mathbf{r}|$. Near the edges of a reflector, numerical errors grow since the approximation of an infinitely large reflector becomes invalid. Therefore, GRASP models the region near a reflector edge as a semi-infinite surface (i.e. a surface extending to infinity in one direction) and applies a method called physical theory of diffraction (PTD) [117]. The electric field from the PTD calculations are subsequently added to that of the PO calculation to get a better approximation of the total scattered field:

$$\mathbf{E}^s = \mathbf{E}^s_{\mathrm{PO}} + \mathbf{E}^s_{\mathrm{PTD}}. \tag{4.36}$$

The accuracy increases as the number of sample points grows, but so does the computation time. To find a good trade-off, a convergence analysis is performed where the calculated field

is compared for a varying number of sample points. Although reflectors down to sizes of approximately 20λ can be successfully analyzed with these methods [100], full-wave methods such as FEM and MoM may be considered when the accuracy requirements are high.

These methods were used to verify the optical performance of STEAMR (see paper F) and the Y-factor setup discussed above. Figure 4.19 shows the power from the ISMAR and STEAMR horns at the plane of the aperture of the black body sources. Minor distortions of the beams in the horizontal directions can be seen, which can be attributed to the off-axis configuration of the setup. Ideal Gaussian beams were used in the simulation to represent the fields from the two horns.

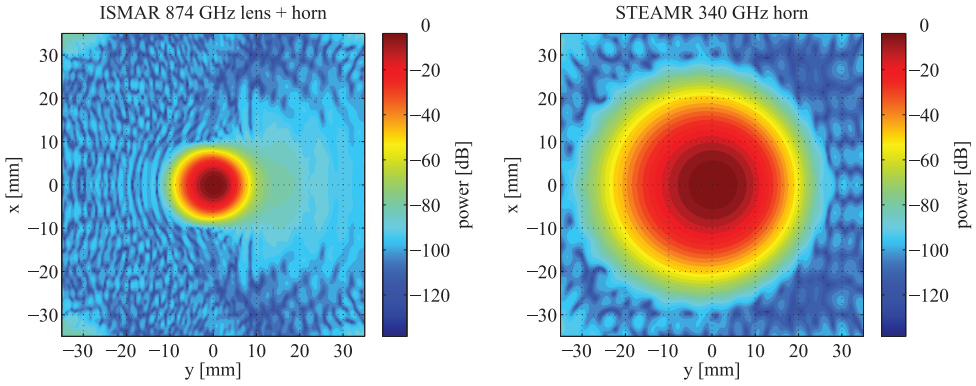

Figure 4.19: Simulated beams from the ISMAR horn at 874 GHz (left) and STEAMR horn at 340 GHz (right) in the load aperture plane of the Y-factor measurement setup (see paper C). Ideal Gaussian beam modes were used to represent the fields from the horns. The load aperture is 100 mm in diameter.

4.3 Mode matching in circular waveguides

Rotationally symmetric horn antennas can be accurately analyzed using full wave methods such as FEM, FDTD and MoM. Although the meshed volume can be decreased due to symmetry, these methods are often computationally heavy and time-consuming – especially when several iterations are needed to optimize the profile of a horn. Mode matching constitutes an efficient alternative, where the horn is modeled as a number of cascaded cylindrical waveguide sections [118]. Each section is represented with a scattering (S) matrix, which describes reflection and transmission of energy for each mode [43]. As the diameters of the horn increases, propagating and evanescent modes are added and the fields are matched at the section interfaces to ensure conservation of energy. This is done in a successive manner for all sections so that the entire horn can be characterized in terms of a scattering matrix. Finally, the modes at the aperture of the horn are propagated in free space so that the far field pattern can be calculated.

Many types of horn antennas have a coupling to the fundamental Gaussian beam mode

(Gaussicity) well above 90% (see – section 2.3). This is a desirable property since it implies a highly symmetrical radiation pattern with low side lobes and cross polarization. Given that the size and location of the corresponding beam waist are known, high Gaussicity horns can be directly incorporated into the two-port theory for Gaussian beam mode propagation (see section 4.2).

All spline horn designs in this thesis were optimized for maximized Gaussicity over the operating bandwidth (see papers D and E). A conical horn with an aperture diameter that provides the desired gain was used as a reasonable starting guess. The length and input diameter were fixed for each design, whereas the spline profile was defined using seventh order Bezier polynomials [119]. A Matlab script was used to randomly generate the spline shapes while controlling a commercial mode-matching code (CORRUG [120]) that calculated the far field pattern at selected frequencies across the operating bandwidth. The same script was also used to calculate the Gaussicity, which was input to a penalty function for the Matlab optimization routine (*fminsearch*).

Although mode matching is a highly efficient method for optimizing horn profiles, the analysis does not take into account packaging and features around the horn that can influence the radiation pattern. Furthermore, since rotational symmetry is assumed, it is not possible to analyze imperfections that break the rotational symmetry or the rectangular-to-circular waveguide transitions at the input of the horn. Hence, when a successful design has been found, it is important to verify the entire design using a full-wave solver based on e.g. FEM, FDTD or MoM. Figure 4.20 shows a comparison between the far field radiation patterns obtained using mode matching and FEM.

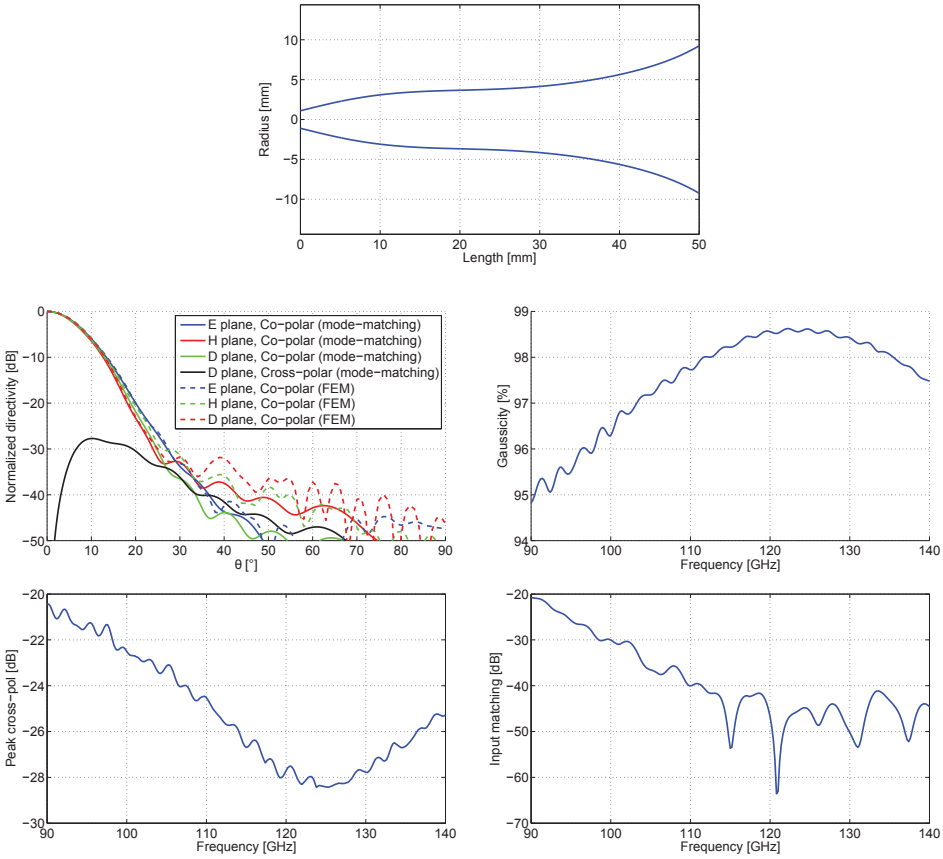

Figure 4.20: Profile (top) and simulation results for a broadband 120 GHz spline horn. The top left figure shows a comparison of normalized radiation pattern at 120 GHz calculated using mode matching and FEM. The remaning figures show Gaussicity, peak cross-polarization level and input matching vs. frequency. Figures from paper E.

Chapter 5

Implementation and characterization

This chapter presents fabrication and testing of the hardware that was built for the MATS, ISMAR and STEAMR instruments. Important results as are highlighted and details about methods and measurement setups are presented.

5.1 MATS optics

5.1.1 Nadir camera

Figure 5.1 shows a CAD model of the flight hardware for the nadir camera of MATS. An aluminium structure to house the three lenses was fabricated using a high-precision lathing process. The three lenses were fixed into its correct positions using threaded retaining rings. Washers made of polyetherether ketone (PEEK) were placed between the housing and retaining rings to avoid damaging the lenses. The CCD was of the same type as for the limb instrument (e2V CCD42-10 [121]) and its position was made adjustable by mounting its housing with screws that run in 8 mm long slots.

An early prototype of the lens housing was fabricated to test the building concept and to verify the optical performance. Since neither the readout electronics nor the CCD housing were ready at the time, the lens housing was built with a Canon bayonet mount so that the optical performance could be evaluated using a standard full-frame camera house. Figure 5.2 shows the prototype lens house and a sample image taken of a cloudy sky. Testing the camera with a point source target (see section 5.1.2) confirmed that the requirement (80% encircled energy at a radius of 250 μm) could be satisfied with good margins – see Figure 5.3.

Optical testing for flight is limited to point source testing across the camera's FoV to ensure satisfactory resolution. To do this, the camera will be placed on a rotary table while illuminating it with light from a point source (see Section 5.1.2). Absolute radiometric sensitivity will be measured to an accuracy of 10% using a calibrated lamp that illuminates a

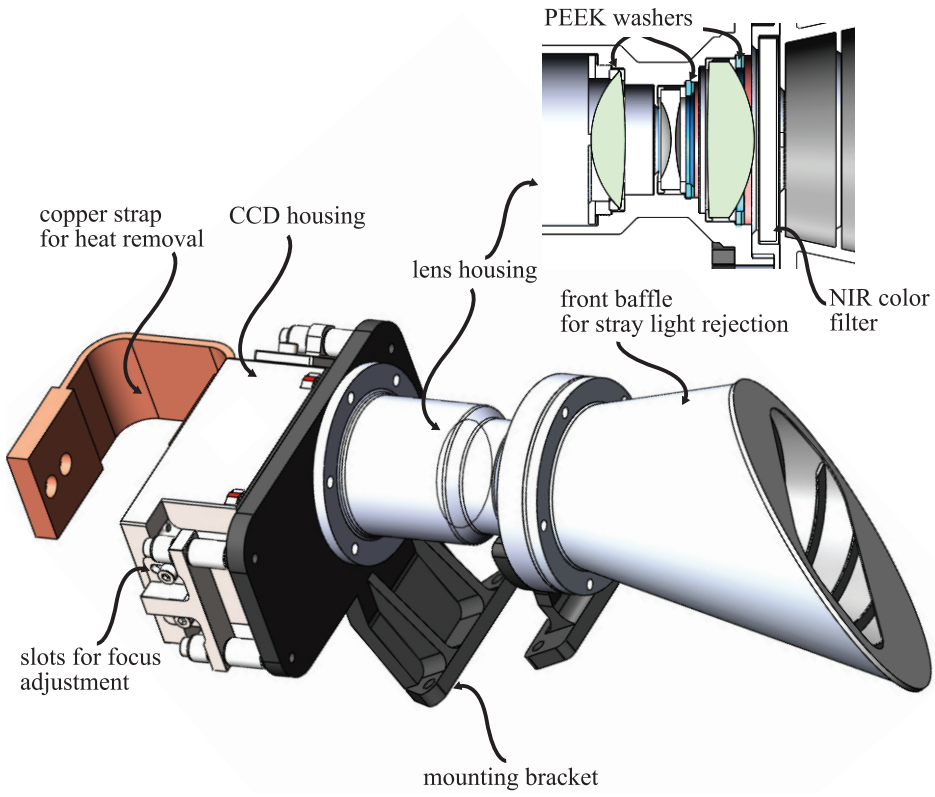

Figure 5.1: CAD model of the nadir camera for MATS.

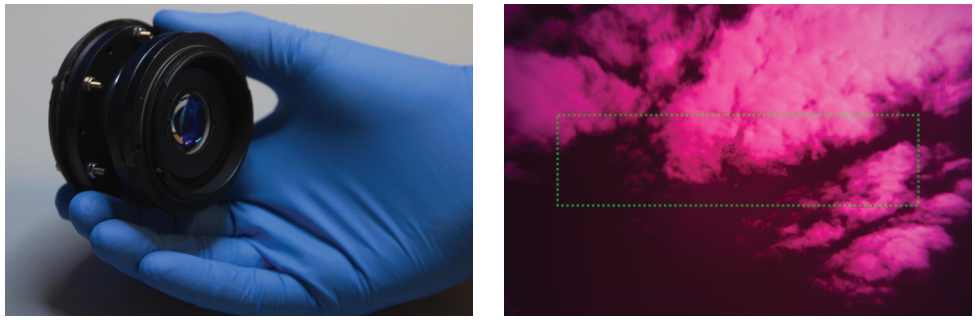

Figure 5.2: Prototype nadir camera objective with NIR color filter and Canon bayonet mount (left) and photograph taken with the same objective mounted on a Canon camera house with a 35 mm image sensor (right). The dashed green rectangle denotes the FoV as it will be with the 27.6 mm × 6.9 mm CCD image sensor for flight [121].

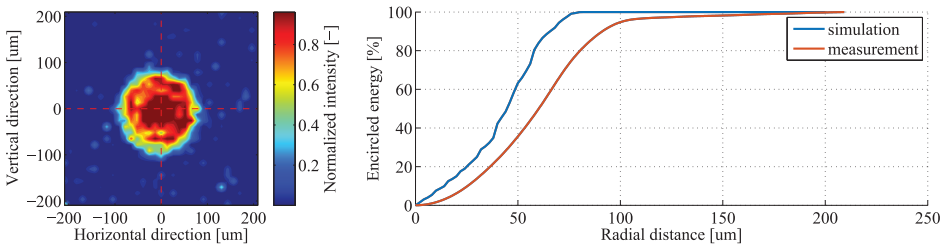

Figure 5.3: Left: image of a point source taken with the nadir camera prototype mounted on a Canon camera house with a full-frame sensor. Right: comparison of simulated and measured encircled energy.

white Lambertian screen in front of the nadir camera. This test will also be used to estimate illumination roll-off for larger field angles. After being integrated on the MATS payload platform (see Figure 3.1), pointing of the nadir camera will be measured with respect to the star tracker and the limb instrument using theodolites and a collimator source [122].

5.1.2 Limb telescope

Flight hardware

The flight hardware for the limb instrument consists of four main parts: limb house, telescope, and beamsplitter/filter assembly and front baffle – see Figure 5.4. A fabrication methodology was applied, where high-precision numerical milling in aluminium was combined with measurements using a coordinate measuring machine (CMM). This provides excellent mechanical accuracy, but implies that new parts need to be machined in order to trim positions of any optical components.

The limb house was milled out of a solid block of aluminium and defines the relative positions between the telescope, the beamsplitter/filter assembly and the six CCD housings. Hence, the geometry of the limb house influences the image location on the CCDs – but not the image quality. The mounting structure for the mirrors and the beamsplitter/filter assembly were also made of aluminium and fabricated using high-precision numerical milling. As for the prototyping and breadboarding test campaigns (see paper A), the geometry of these structures was measured using a CMM. Deviations from the nominal geometry were within ±0.2 mm for the beamsplitter/filter assembly – see Figure 5.5. Although the base plate was slightly bent, this was still well within tolerances to ensure good relative pointing between six channels of the instrument. All filters and beamsplitters were made of 3 mm thick glass (fused silica), which were positioned using Teflon tape as spacers to the baseplate and glue on the sides (see Figure 5.4)

The geometry of the mounting structure for the three mirrors was designed to optimize the imaging quality for the measured surface errors of the three diamond turned mirrors (see paper A). As can be seen in Figure 5.5, the deviations from nominal dimensions were small and could be corrected for by machining L-brackets and spherical washers with slightly adjusted geometries – see Figure 5.6.

All parts inside the limb instrument were coated with black nickel, which has a reflectivity of 2-6% across the operating wavelengths of MATS. Combined with structures that encapsulate the light path from the telescope to the image sensors, this helps to reduce the sensitivity to scattered light inside the instrument. Simulations made for the prototype hardware showed that unwanted reflections from the broadband filters lead to ghosting issues caused by too little distance to the beamsplitters (see paper B). Hence, the distance between beamsplitters and broadband filters was significantly increased for the flight hardware (see Figure 5.4) so that the unwanted reflections could no longer propagate directly to the image sensors.

The flight front baffle was fabricated from six separate parts that were made of aluminium. Each baffle vane was machined to have an edge thickness of 10 µm and light traps were made to avoid light leakage between the upper- and lower parts of the baffle. As with the baffle breadboard, the flight baffle was coated with Vantablack S-VIS, which has a reflectivity of 0.2-0.6% between 250-1400 nm [109].

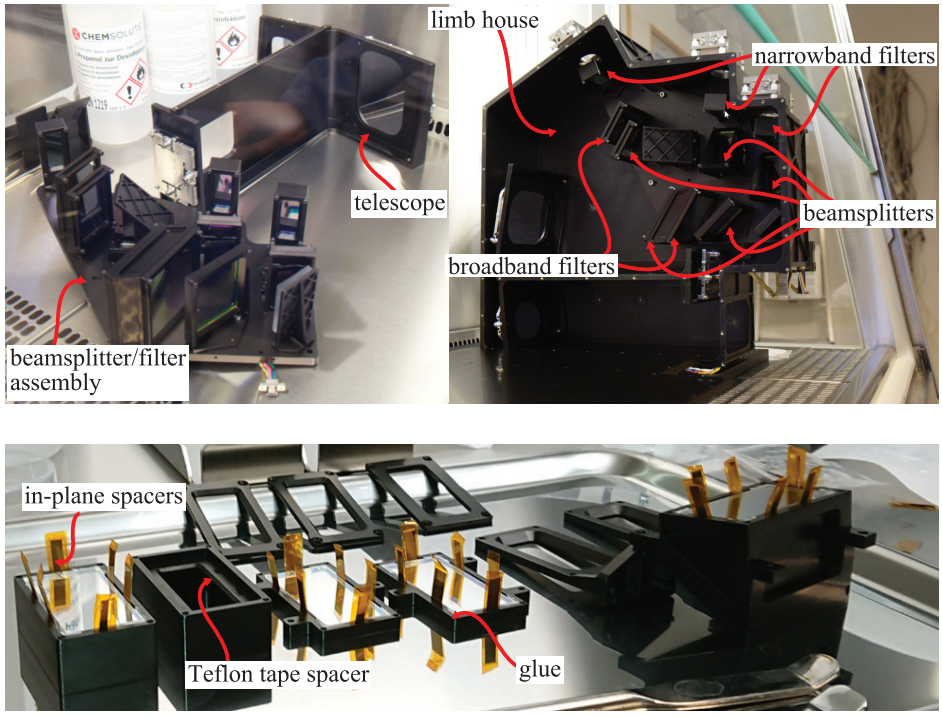

Figure 5.4: Mounting of flight hardware for the limb instrument in a clean environment inside a laminar flow cabinet. Top left: beamsplitter/filter assembly and telescope. Top right: limb house with mounted beamsplitter/filter assembly and telescope. Structures to block unwanted light paths (i.e. internal stray light) were not yet installed when the picture was taken. Bottom: gluing of narrowband filters into mounting fixtures.

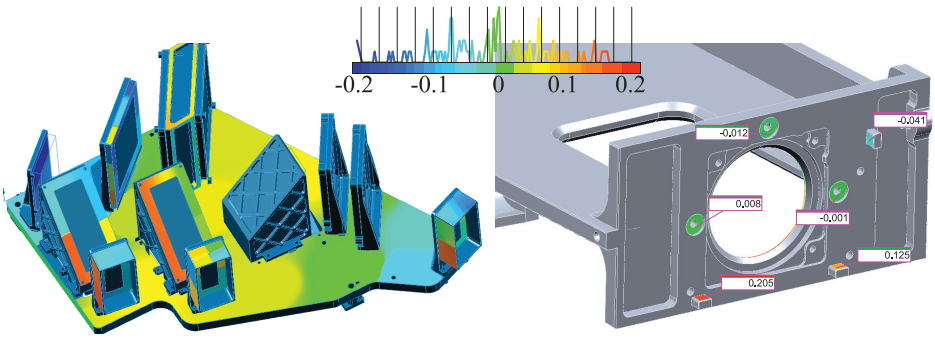

Figure 5.5: Results from CMM measurements of the beamsplitter/filter assembly (left) and telescope mounting structure (right) for flight. The deviation from nominal dimensions are given in mm.

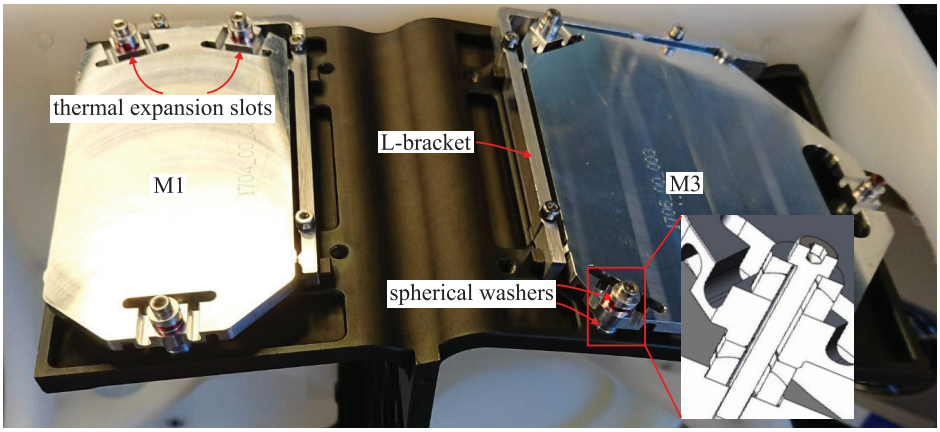

Figure 5.6: Limb telescope as seen from the backside of the M1 and M3 mirrors. The cross section of a mounting point with spherical washers on each side of the mirror is shown at the bottom. Image from paper A.

Imaging performance tests

A reflective collimator was used to characterize the quality of the images taken by the instrument. This system is essentially an $f/9$ (D = 110 mm) off-axis Newton telescope used in reverse – i.e. projecting images of test targets situated in the focal plane (see Figure 5.7). In terms of resolution, the collimator is capable of projecting targets details down to 100 lp/mm over a FoV of 3.3°. Diffuse background illumination of the test targets was achieved by using a 150 W Xe connected to an integrating cylinder. A USAF 1951 target was used for general testing and subjective assessment of the imaging quality. Each pair of horizontal and vertical bars on the target correspond to a spatial resolution given by $2^{n_g+(n_e-1)/6}$, where n_g is the group number (column) and n_e is the element number (row). The limb instrument should be capable of resolving features corresponding to n_g = 0-2 and n_e = 4 (c.f. Table 3.1) in the horizontal direction. For more detailed tests, a slanted edge target was used to calculate the MTF [123] and a ruler pattern target was used for FoV and distortion tests (see Figure 5.7).

A collimator system provides information about the resolution in a direct and tangible way, which makes it a highly useful device to evaluate the performance of the MATS optics. However, many other techniques can be applied to test an optic of this kind. Most notable is perhaps the field of interferometric testing [124], where the wavefront error produced by the optic is evaluated using an interferogram from an interferometer with an optical flat as a reference. Notable devices include the Mach-Zehnder and Fizeau interferometers [125]. Interferometric testing can be useful to provide direct insight into the types of aberrations present in the tested optic. Other classic methods for evaluating the optical performance of telescopes include the Focault [126] and Rhonci [127] tests.

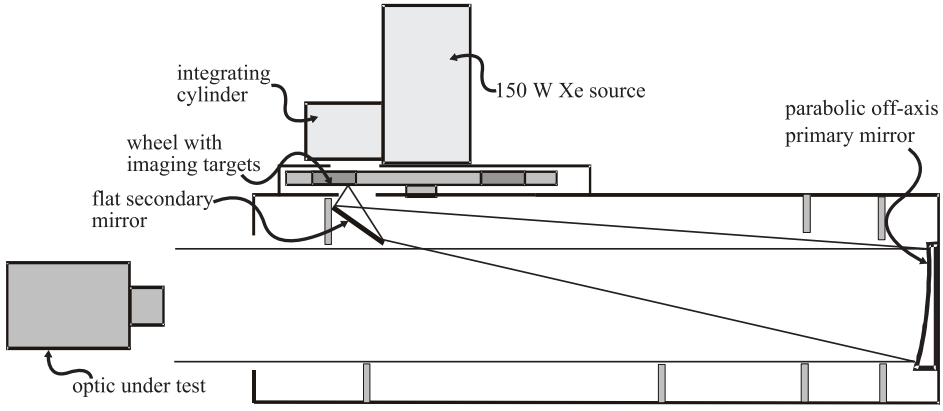

Figure 5.7: Sketch of the collimator system used for optical performance tests.

All tests were performed inside a newly built dark room lab, which provides an environment with low scattering completely protected from light leaks. A small room was built around the entrance to the lab, which served as an air lock and gowning area to minimize contamination from the outside. People working inside the lab wore clean room garments and performed daily sweeping of the floors to keep the environment as clean as possible (see

paper B). During testing, the limb instrument was placed on an optical test bench that in turn was placed on a rotary stage to cover the entire horizontal FoV of the limb instrument – see Figure 5.8. To minimize contamination from residual dust in the room, the setup was placed under a 2 m × 2 m × 2 m movable clean room tent with a HEPA fan creating a laminar flow of clean air around the instrument.

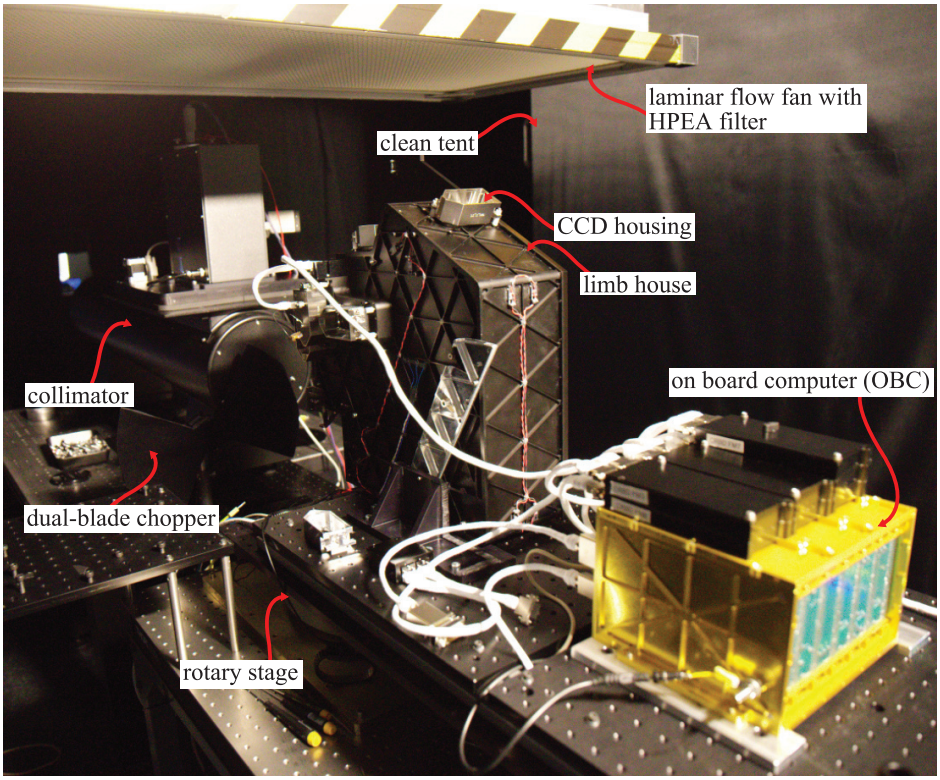

Figure 5.8: Imaging performance test setup inside a clean tent with filtrated air.

The full characterization of the optics of the limb instrument includes testing of resolution (using MTF, point source and USAF 1951 targets), relative pointing between the six channels (using a point source target) as well as FoV and distortion tests (using the FoV/distortion target). As part of the absolute radiometric calibration preceding the optical testing, broadband extended targets will be used for flat fielding tests where deterministic imperfections (e.g. non-uniformities of the CCDs and illumination roll off in the optics) will be measured so that these can be corrected for, during operation in orbit.

The test campaign for the flight hardware is ongoing at the time of writing. Setbacks were discovered during the prototyping activities, which influenced the optical performance of the limb instrument. Resolution tests showed that the M3 mirror intended for flight was not up to specifications. Although the form error of the surface was better than the one

used for prototype tests (see paper A), the imaging performance proved to be significantly degraded with the new mirror – see Figure 5.9. Possible explanations for this could be an incorrectly performed stress release during fabrication or a tilt between the three mounting points and the mirror surface. Moreover, vibration tests to launch qualification levels showed that the suspension around the mounting points were too weak (see Figure 5.6), which led to a complete mechanical failure. Hence, a new and more robust mirror was fabricated for flight. In addition to the problems with M3, it was discovered at a late stage that the measured form errors of the mirrors had been provided in an inverted coordinate system. This resulted in a mirror mounting structure with dimensions that were compensated incorrectly (see paper A). Hence, greatly improved results could be obtained by reverting to the mounting structure used for prototype hardware – see Figure 5.10-5.11.

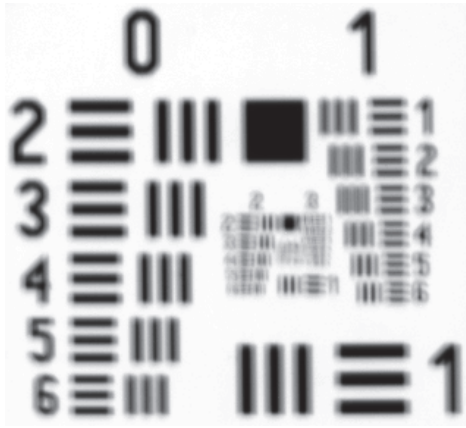

Figure 5.9: Test image taken with the IR2 channel of the flight instrument using flawed M3 mirror and mirror mounting structure with incorrectly compensated geometry.

Each CCD image sensor was positioned manually using a focusing jig with a micrometer stage – see Figure 5.12. In this process, a series of images was taken for different distances between the CCDs and the limb house. Point source targets were used and the results were analyzed in terms of encircled energy. Edge targets were also used to calculate the MTF as a complementing measurement. To ensure that readout smearing would not influence the vertical resolution, a dual-blade chopper was placed in front of the collimator to serve as a mechanical shutter. This proved to be an easier way to remove readout smearing than data post-processing, which requires a correct row shifting time as input to work correctly.

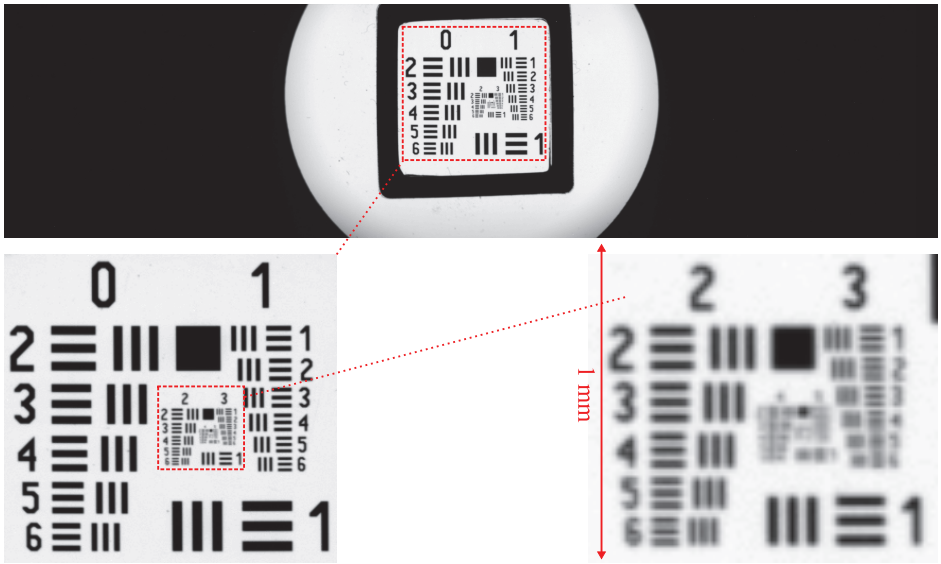

Figure 5.10: Test image taken with the IR2 channel of the flight instrument using the updated M3 mirror and prototype mirror mounting structure. The top image shows the full image from the 2048 × 512 pixels CCD. Magnified versions of the same image are shown at the bottom.

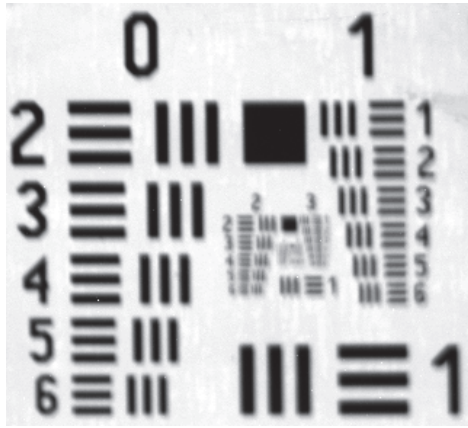

Figure 5.11: Test image taken with the UV2 channel of the flight instrument using the updated M3 mirror and prototype mirror mounting structure.

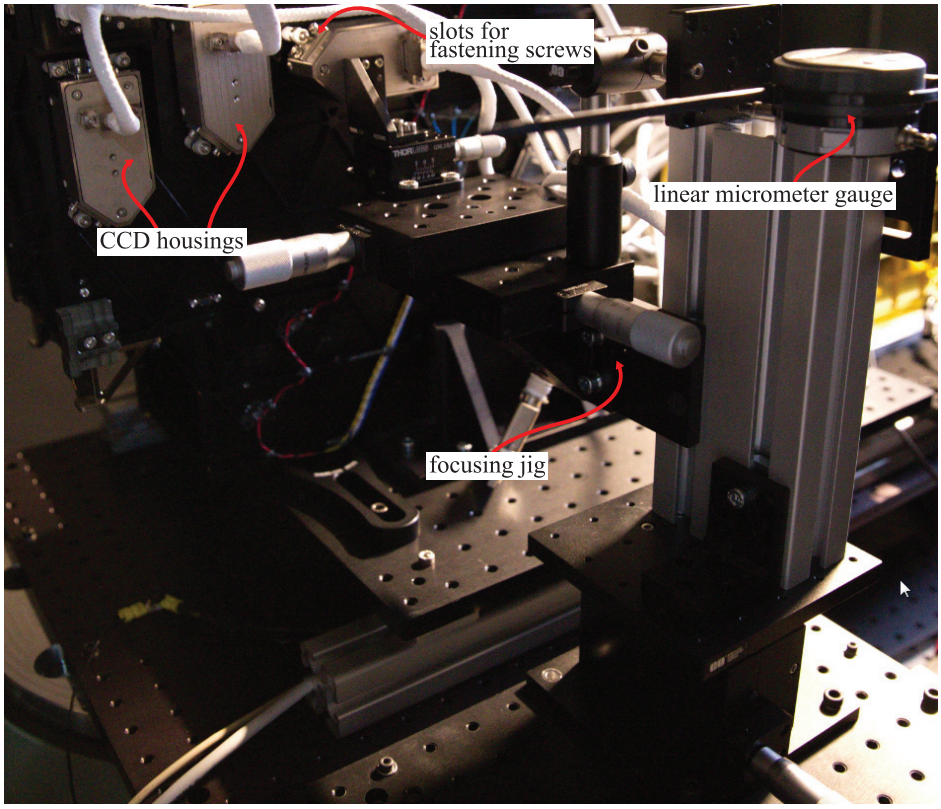

Figure 5.12: Focusing of the UV2 channel using translation stages and a digital micrometer linear gauge.

5.1.3 Stray light rejection

The same room used for imaging performance tests was also used for stray light measurements. A source consisting of a 1 kW Xe lamp with a focusing lens and a parabolic mirror was used in lieu of the collimator for imaging performance tests. The source was placed at the opposite side of the room, which was separated into three sections using two blackout curtains that reach across the room, from the ceiling to the floor – see Figure 5.13. This provided better collimation while ensuring that unwanted light paths from the source to the test object were blocked.

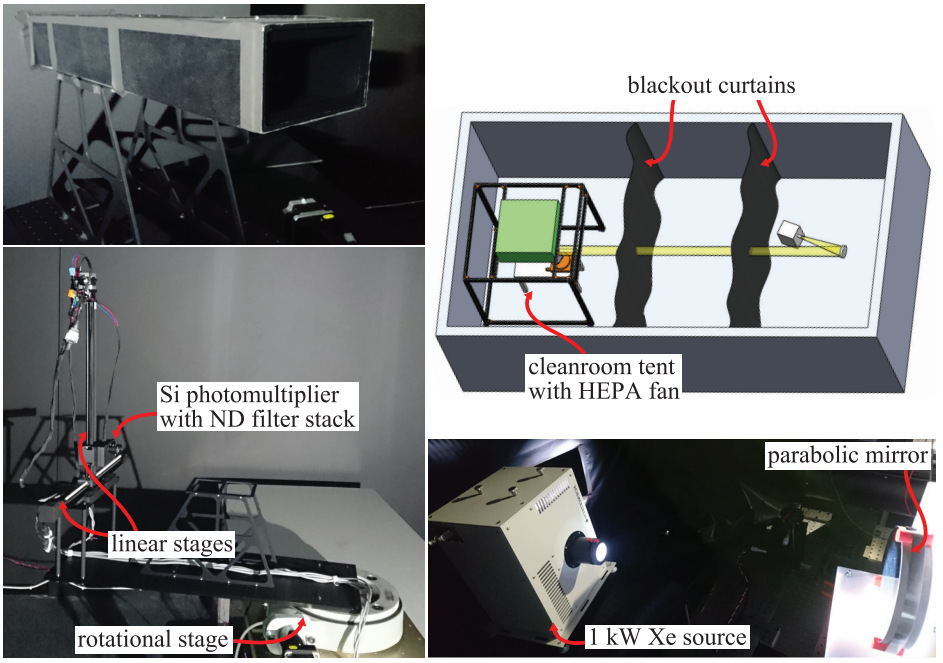

Figure 5.13: Stray light testing facility. Top left: baffle breadboard. Top right: layout of the lab. Bottom left: baffle mounting structure on rotary stage and silicon photomultiplier detector mounted on XY stages. Bottom right: source setup with a 1 kW source being focused using a fused silica achromatic lens and parabolic mirror.

This setup was initially used to measure the PST as a function of incidence angle for a baffle prototype coated with Vantablack S-VIS (see paper B). A silicon photomultiplier (Hamamatsu, S13360-6050CS) was used in this case to detect the low levels of light making through the baffle. Since the actual detector was only 6 mm × 6 mm, it was mounted on a XY linear stage setup and scanned across the rear aperture to cover it completely. Black plastic cardboard was mounted around the detector (not behind) to further block any unwanted light paths from the source to the detector. The detector circuit board was mounted inside a custom-made aluminium housing. A plastic lid covered with a low-reflectance foil (Acktar, Metal

Velvet [128]) and with a configurable stack of ND filters was attached to the housing to minimize scattering and adjusting the amount of light to appropriate levels.

Results from this effort showed that the facility was capable of measuring a PST down to at least 10^{-6}, which meets instrument requirements (see Chapter 3.1). Moreover, the results also showed a close agreement between measurements and the non-sequential ray tracing simulations where the Vantablack S-VIS coating was represented using empirical BRDF data – see Figure 5.14.

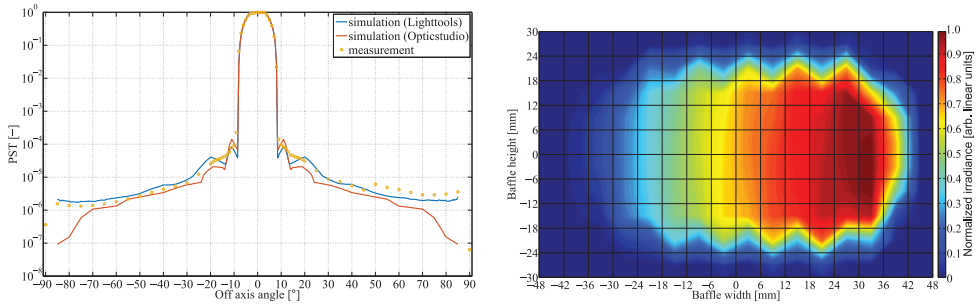

Figure 5.14: Simulated and measured PST as a function of angle of incidence (left). Intensity of light transmitted through the test baffle at an incidence angle of 40°. Figures from paper B.

At the time of writing, the stray light rejection measurements for the flight hardware have not yet been started. The method that will be used is analogous to that of the baffle breadboard, i.e. the instrument will be mounted on the same rotary stage and illuminated with the same source. A full characterization, where the stray light rejection is measured from all angles of incidence, will not be performed due to time constraints. Instead, a single sweep in the vertical direction will be performed to cross-check the measured PST with simulations (see paper B).

5.2 Horn antennas

5.2.1 Manufacturing methods

Fabricating corrugated horns poses a major challenge compared to the designs that lack corrugations, especially at high frequencies. One method to fabricate corrugated horns is to start with a mandrel with the shape of the corrugated horn, which is then used as a ”negative” in an electroplating process where metal is grown to form the horn [129]. The mandrel is dissolved in the final step to lay bare the horn. Although good results can be achieved this way, the method is relatively complicated. Other methods for manufacturing corrugated horns include precision milling in metallic split-blocks or stacking metallic ring-shaped shims of varying inner diameters to define the desired corrugated profile shape [130].

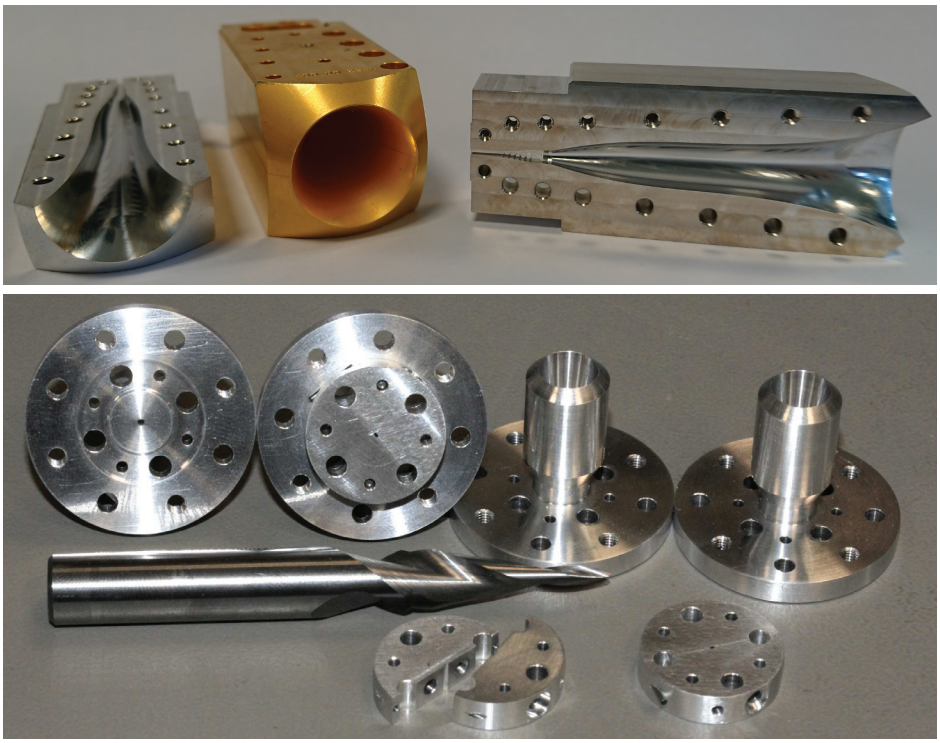

Figure 5.15: Images of horns made from aluminium using different manufacturing techniques. Top: Gold-plated and bare aluminium 120 GHz test horns for Y-factor measurements (c.f. paper E). Bottom: 340 GHz prototype horns for STEAMR, rectangular-to-quadratic waveguide transitions and a custom-made broach tool. Bottom image from paper d.

Less complicated methods were used to fabricate the spline horns presented in this thesis. Most horns were machined from two separate aluminium blocks using numerical milling,

although one 340 GHz prototype horn for STEAMR was made using a custom-made broach to define the spline shape (see paper E). Figure 5.15 shows examples of horns manufactured using these two techniques. These manufacturing techniques have different advantages and disadvantages. As was shown in paper C, integration of the horn into the metallic split block can be used to minimize losses and standing waves. The form accuracy of the spline shape was often in the order of a few micrometers (see Figure 5.16), which does not result in any major degradation in performance. However, simulations show that the cross-polar levels will increase as a result of lateral misalignment between the two block halves (see paper C). This is naturally avoided when using a monolithic fabrication method where the horns are drilled out of a single block of metal. Such methods can be advantageous when a large number of identical horns are needed. Multi-pixel array applications [131] are one example where this method has been applied, although split block milling has also been used for similar applications [132].

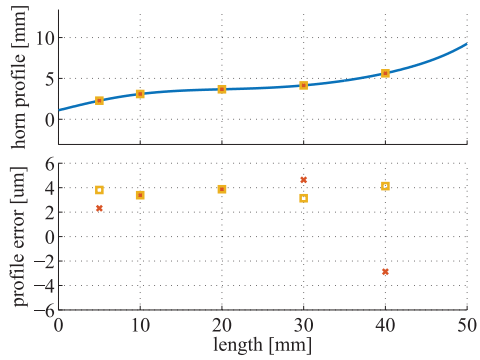

Figure 5.16: Measured form errors of two 120 GHz spline horn block halves, c.f. Figure 5.15 and paper E. The ideal spline shape is shown in blue, whereas points denote discrete profile measurements.

5.2.2 Radiation pattern measurements

Measuring the radiation pattern of an antenna in the far field has the advantage that no transformation from the near field is needed. Measuring a feed horn with an aperture of tens of wavelengths can typically be made directly in the far field. However, the situation becomes very different for reflector antennas that can be orders of magnitude larger. For example, a 1 m reflector at 300 GHz has a far field located 2 km away from the aperture (c.f. equation 2.9). For such large antennas, it is therefore common to measure amplitude and phase in the near field region and use the results to calculate the far field radiation pattern [133]. Alternatively, compact antenna test ranges (CATR) [134], holographic methods [135–137] or complex field mapping [138] can be employed.

A basic scheme and photo of the antenna measurement setup are shown in Figures 5.17-5.18. Two phase-locked synthesizers with YIG oscillators were connected to cascaded Schottky diode multiplier stages to reach the correct transmitter and LO frequencies. The AUT was

connected to a Schottky mixer receiver where the IF signal was amplified using two LNAs. A reference signal was generated by mixing the fundamental signals from the synthesizers and up-converting using the same multiplication factor as was used for the transmitter in order to compensate for relative phase drifts. Both signals were finally down-converted using a common source to match the bandwidth of a fast Fourier transform (FFT) spectrometer (0-2.5 GHz). A regular desktop computer was used to control the motion of the linear stages and collecting data from the FFT spectrometer. Radio absorbing material (TKRAM [139]) with a return loss of < -40 dB was used around the probe and the AUT to minimize unwanted effects of multi-path propagation/standing waves. The probes (corrugated horns and open-ended waveguides for spherical and planar measurements, respectively) had chamfered aperture edges for the same reason.

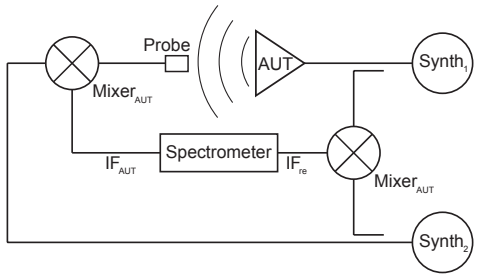

Figure 5.17: Basic setup for antenna measurements.

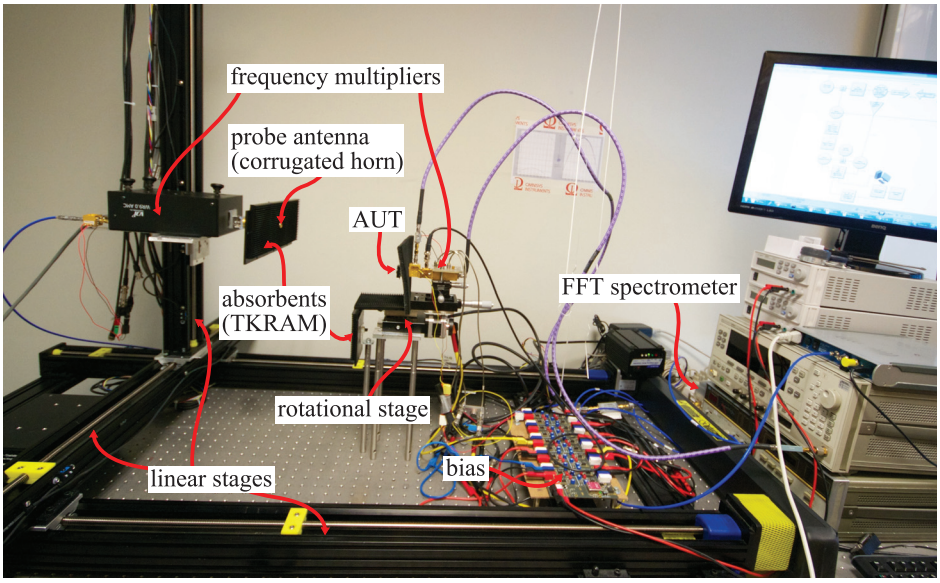

Figure 5.18: Setup used for measuring horn antennas in spherical and planar geometries.

Short-term phase drifts were minimized by carefully choosing stable working points for the electronics (frequency, bias voltages etc.). Long-term phase drifts correlated strongly with the ambient temperature, cf. Figure 5.19. Lengthy measurements (2-3 hours) were therefore performed nighttime when the house ventilation was turned off so that the temperature varied relatively slowly. The probe was moved to the center every 15th minute to record the signal, which was used as a phase reference. Assuming a linear phase variation between each reference measurement, a post-processing compensation could be used to even out phase drifts. Cable lengths to the transmitter and receivers were also matched in length to minimize phase drifts due to temperature variations. Bending of coaxial cables during the scanning also affects the phase. Highly phase stable cables (Gore, Phaseflex) were therefore used and attached to the ceiling so that bending was minimized (see Figure 5.18).

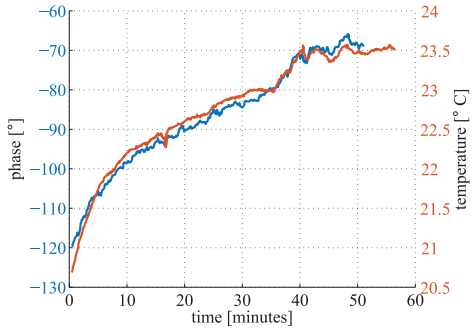

Figure 5.19: Phase drifts of the antenna measurement setup compared to ambient temperature drifts.

For the planar scanning geometry, additional phase variations can occur due to skewness in the linear stages that cause an additional change in the AUT-probe distance. However, since this error is deterministic, it can be measured and used to correct the data in the post-processing. A digital linear micrometer gauge was mounted on the vertical linear stage and swept on a flat diabase datum to measure the flatness of the measurement plane. Within the 6 cm × 6 cm scanning area, a peak-valley deviation of 7.2 µm ($\sim \lambda/140$ at 300 GHz) was measured. For a 32 cm × 32 cm area, the peak-valley error was below 70 µm ($\sim \lambda/14$ at 300 GHz). Since the quadratic scanning plane for horn antennas was typically 5-10 cm wide, no correction skewness of the linear stages was needed when measuring horn antennas.

The setup was used to characterize horns at 175-874 GHz, although different RF configurations were used for each antenna. Prototype horns for STEAMR (see paper E) were measured using both spherical and planar geometries. Figures 5.20-5.21 summarize the results. As can be seen, the setup could resolve features down to 40 dB below the peak. The phase pattern was obtained by compensating for linear drifts in the system. Combining amplitude and phase data, the Gaussicity could be calculated – see Table 5.1. A large truncation of the measured field tends to lead to an over-estimated Gaussicity calculation as the irregularities seen far away from the main peak are simply omitted. Hence, a scan area covering a portion of the beam down to below −40 dB was used.

Besides having excellent consistency with simulations, the results from figure 5.20 also

show that the dynamic range of the setup is better than 40 dB and that a highly symmetric phase pattern can be obtained after corrections for linear drifts. Since the signal source used for the transmitting side of the setup had a strong frequency-dependence of the output power, it was only possible to perform the beam measurements at 329 and 338 GHz where the signal was strong and stable. At frequencies ≥340 GHz, the output power dropped to essentially zero. This signal source was later replaced for the far field θ-cuts measurement shown in Figure 5.21.

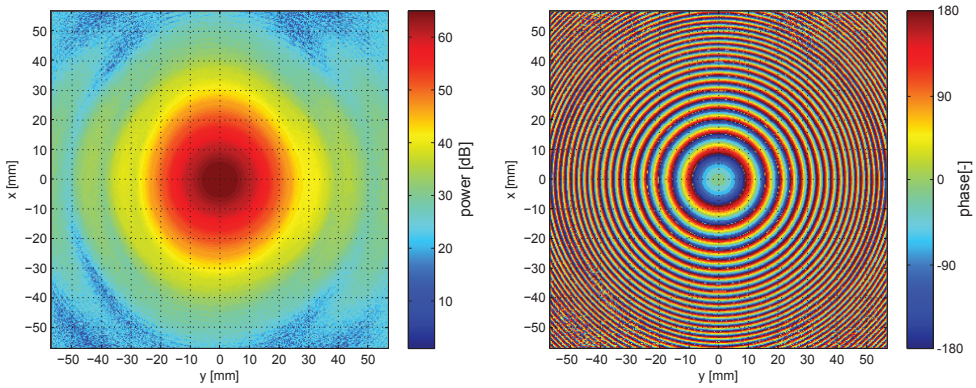

Figure 5.20: Measured power (left) and phase (right) contour plots of broached STEAMR prototype spline horn. The H plane is aligned with the vertical x-axis and, consequently, the E plane is aligned with the horizontal y-axis.

Frequency [GHz]	Gaussicity [%]	Waist radius [mm]	Aperture-waist distance [mm]
329	97.7/98.1	1.86/1.92	12.67/11.7
338	97.8/98.1	1.94/1.91	12.70/11.6

Table 5.1: Gaussian beam parameters (simulated/measured) for the broached STEAMR prototype spline horn.

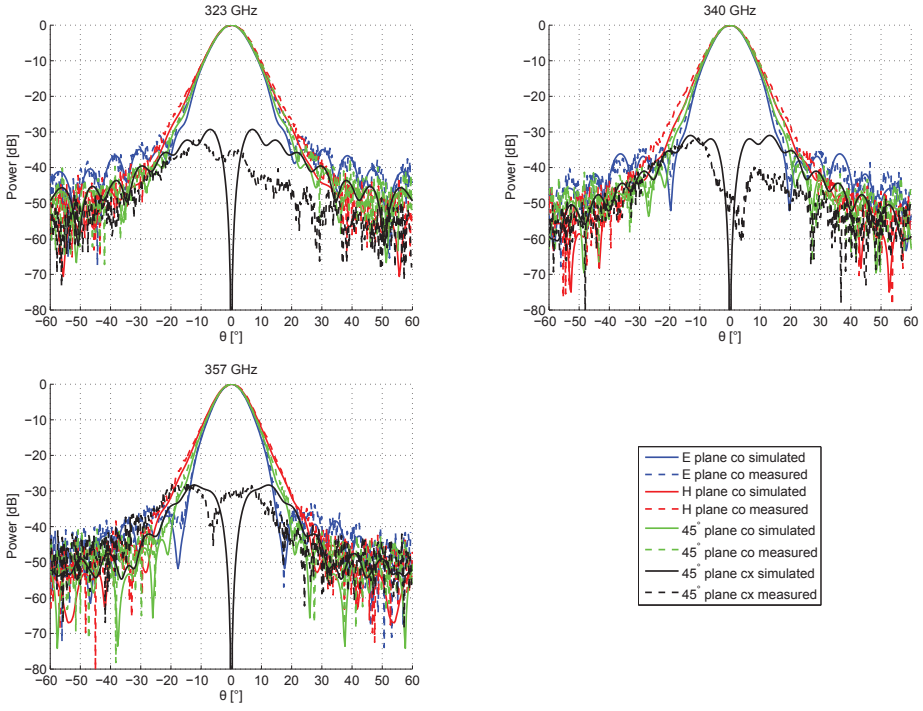

Figure 5.21: Far field, co-polar power cuts in the E, H and 45° planes and cross-polar cut in the 45° plane of the 340 GHz horn. Top right image from paper E.

5.3 Noise temperature measurements

A common method to determine the noise temperature of a heterodyne receiver is the so-called Y-factor technique. By detecting the power from black body sources at well-defined temperatures, it is possible to estimate the amount of noise produced by the receiver itself. The most basic configuration includes two sources at temperatures T_H and T_C ($T_H > T_C$) and the noise temperature is simply calculated using linear extrapolation, c.f. Figure 5.22. More complex schemes that involve more black body sources can be used in order to account for non-linearities of the receiver. The Y-factor for the basic two-load case is defined as the ratio of detected power from the two loads. Using equation 2.23, this becomes

$$Y(\nu) \equiv \frac{k_\mathrm{B}\, B\, T_2\, G_{rec}}{k_\mathrm{B}\, B\, T_1\, G_{rec}} = \frac{k_\mathrm{B}\, B\, (T_H + T_{rec})\, G_{rec}}{k_\mathrm{B}\, B\, (T_C + T_{rec})\, G_{rec}} = \frac{T_H + T_{rec}}{T_C + T_{rec}}. \tag{5.1}$$

From this, the SSB- and DSB noise temperatures can be written as:

$$\begin{aligned} T_{rec,DSB}(\nu) &= \frac{T_H - Y(\nu) T_C}{Y(\nu) - 1} \\ T_{rec,SSB}(\nu) &= \frac{2(T_H - Y(\nu) T_C)}{Y(\nu) - 1}, \end{aligned} \tag{5.2}$$

where the excess factor of 2 in the second expression comes from the fact that a SSB receiver only accepts power from one sideband.

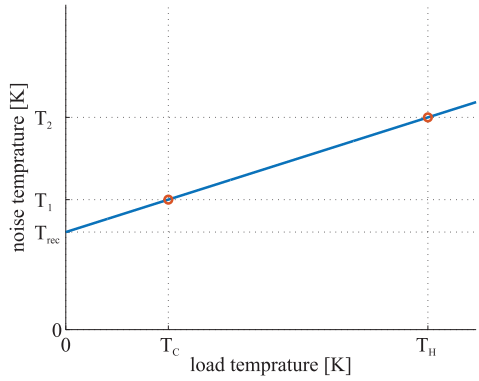

Figure 5.22: Noise temperature versus load temperature for an ideal linear receiver.

For the Y-factor measurement to be accurate, it is important to take into consideration losses in the setup itself as these manifest themselves as additional noise. As discussed in paper C, Ohmic losses, absorption in the transmission medium and scattering losses should be carefully investigated and corrected for to accurately estimate the receiver noise temperature. Performing the measurements in vacuum removes uncertainties associated with transmission losses in air, which have a strong frequency dependency in the THz band, c.f. Figure 2.2. Standing waves between the source and the receiver can also contribute to a frequency and

distance-dependent disturbance to the measurements. One simple way to circumvent this problem is therefore to vary the path length between the source and receiver so that the standing-wave pattern can be measured [140] and corrected for. This was also done for the Y-factor setup used to measure the noise temperature of the 874 GHz receivers for ISMAR by simply stepping the receiver chain using the focusing slide – see Figure 5.23. However, with low return loss of the loads [141], no standing-wave pattern could be observed.

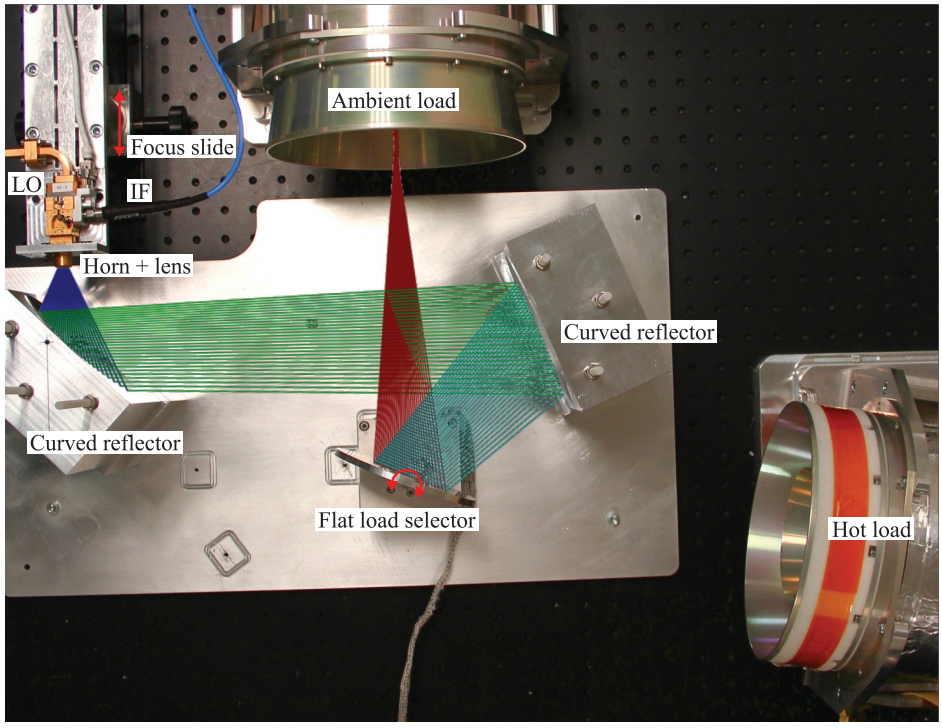

Figure 5.23: Y-factor setup with frequency-independent optics used to measure noise temperature of THz receivers. Photo from paper C.

Chapter 6

Conclusion

This thesis summarizes contributions to the optical systems of three Earth observation instruments: Mesospheric Airglow/Aerosol Tomography Spectroscopy (MATS), International Submillimetre Airborne Radiometer (ISMAR) and Stratosphere-Troposphere Exchange And climate Monitor Radiometer (STEAMR).

An off-axis $f/7.3$ (D = 35 mm) reflective telescope with three free-form mirrors was developed for the limb viewing instrument of MATS. This is the first realization of a design methodology where linear astigmatism is eliminated to achieve a relatively large FoV (5.67° × 0.91°). The instrument was designed with six CCD image sensors, which operate over wavelengths between 270-772 nm. Imaging performance tests resulted in an MTF of 0.45 at 20 lp/mm, which is satisfactory from the perspective of instrument requirements, although increased resolution was predicted with realigned mirrors based on the modeling of the fabricated mirror surface figure errors.

Stray light analysis was also performed for the limb instrument of MATS. A non-sequential ray tracing model that includes all critical parts of the instrument was made and used to calculate the expected stray light suppression of the instrument. The results show a predicted stray light suppression of 10^{-10}-10^{-4} for light sources at altitudes just below the nominal FoV. In connection to the simulations, a simplified model of the front baffle was produced and simulated in terms of stray light. This was coated with a new type of extremely black coating based on vertically aligned carbon nanotubes, which will also be used for flight. A facility for stray light measurements was built, where the baffle was tested. Results showed excellent agreement simulations. In addition, it was verified that the facility is able to measure a point source transmittance down to at least 10^{-6}.

An integrated horn antenna and low-loss dielectric lens were developed for the two 874 GHz Schottky mixer receivers for ISMAR. Combined with state-of-the-art Schottky mixer diode circuits and integrated LNA circuits, the receiver exhibited record-low DSB noise temperatures of 2770 K and 2260 K with and without the lens, respectively. Far field radiation patterns from horns and lenses were measured at 868.7-880 GHz, which confirmed that the FWHM of the main lobe was well below the required 5°. Time-domain measurements performed with a separate horn and lens connected to a 750-1100 GHz frequency extender

showed that reflections from the waveguide interface dominate over reflections from the horn itself and the lens.

The same design methodology was also applied to make spline horns at frequencies 120-340 GHz. Gaussicity values of 98% were obtained over bandwidths up to 19% using an optimization algorithm based on mode matching in circular waveguides. Amplitude and phase patterns from the horns were measured using a setup, which allowed for both spherical and planar scanning geometries. Depending on frequency, the setup was capable of resolving features 30-40 dB below the main peak of the beam.

The 340 GHz multi-pixel optical system of STEAMR was designed using a combination of methods from ray-tracing, Gaussian beam mode analysis and physical optics. A new type of complex optical system with a total of six off-axis reflectors and a dual-reflector focal plane array with faceted surfaces for each channel motivated a detailed study on mechanical tolerances. Optical modeling based on ray-tracing and physical optics methods were combined to evaluate mounting tolerances, distortions of the $1.6\,\mathrm{m} \times 0.8\,\mathrm{m}$ primary reflector and identify what parts of the optical systems were the most sensitive. It was determined that overall tolerances of $100\,\mu\mathrm{m}$ from manufacturing were needed to ensure satisfactory performance, while the corresponding requirement for stability in orbit was $30\,\mu\mathrm{m}$. Primary reflector distortions should be kept below $10\,\mu\mathrm{m}$. To connect the tolerances to manufacturing techniques, a demonstrator for three off-axis mirrors and the focal plane was built and measured mechanically. The results showed that mirror mounting accuracies of $50\,\mu\mathrm{m}$ were obtained.

Off-axis telescopes that are corrected for linear astigmatism have excellent imaging performance over a large FoV and can operate over a wide range of wavelengths. Advances in the fabrication of off-axis free-form mirrors enable larger apertures and smoother surfaces. This type of optic is therefore highly applicable in several fields besides Earth observation, e.g. astronomy, monitoring applications and possibly even consumer-market products. With a large focal plane, several different detector technologies can be accommodated simultaneously to achieve multi-band operation with the same telescope.

It has been shown that spline horns can be designed with a performance equivalent to corrugated horns. The absence of corrugations opens up for new manufacturing methods, which makes it possible to integrate horns and receivers. This concept is scalable to frequencies beyond 1 THz and provides more compact and light-weight receiver packaging. Spline horns are also suitable for future array applications, where broaching makes it possible to efficiently fabricate many identical horns in monolithic receiver blocks or as individual components. One interesting topic for future investigations is how losses vary for different spline horn designs and how this can be traded off against performance parameters such as bandwidth, Gaussicity and return loss.

Chapter 7

Summary of appended papers

Paper A

Wide-field off-axis telescope for the Mesospheric Airglow/Aerosol Tomography Spectroscopy satellite

The development of the three-mirror off-axis limb telescope for the MATS satellite is presented in this paper. This includes design, manufacturing and testing of the telescope.

My contributions include a breakdown/interpretation of scientific goals to define optical/instrument performance requirements, suggesting a general design layout (a common three-mirror telescope for all six channels with a network of beamsplitters and filters), optimization of free-form mirror shapes and position, running and analyzing optical tolerances, definition of optical test methods and construction of the optical test facility, performing optical resolution tests and writing the paper. I also initiated a collaboration with a South Korean research group, which resulted in the first iteration of the optical design based on methods developed by the group.

Paper B

Stray Light Suppression of a Compact Off-Axis Telescope for a Satellite-Borne Instrument for Atmospheric Research

Stray light of the MATS telescope is investigated in detail in this paper. A combination of measurements and software simulations were performed to predict the instrument's ability to suppress stray light from any direction. The results were used as input for an instrument software model that takes into account the most significant aspects of the six channels of the optic (image resolution, wavelength and temperature dependencies, detector noise, signal strength, integration time, read-out smearing, stray light suppression etc.). Simulated atmospheric scenes were then used as input to the model in order to get an accurate prediction of the instrument performance.

My contributions include stray light simulations, design of the baffle system, layout of optical components for minimized stray light throughput, definition of stray light test methods and construction of the test facility, performing stray light tests, analyzing test results, coding of the instrument model and writing the paper.

Paper C

Low noise 874 GHz receivers for the international submillimetre airborne radiometer (ISMAR)

This paper focuses on the development of the two 874 GHz receivers developed for ISMAR, which includes a dielectric lens, spline horn, front-end mixer and IF LNA, LO system and a total power back-end. Special attention was given to the front-end and in particular to the performance in terms of intrinsic noise and radiation pattern.

My contributions include design, construction and code writing for the test setup for radiation pattern measurements, development of the Gaussian beam mode code used in the lens design, radiation pattern measurements, optical design of the setup used for Y-factor measurements, compilation and analysis of measured data as well as writing the paper.

Paper D

A 874 GHz mixer block integrated spline horn and lens antenna for the ISMAR instrument

In this paper, the compact smooth-walled spline horn at 874 GHz for the ISMAR instrument is presented. The design process for the spline horn and dielectric lens are explained in detail.

My foremost contribution was to write the code used for the design of the dielectric lens as well as contributing to discussions and writing of the paper.

Paper E

THz Smooth-Walled Spline Horn Antennas: Design, Manufacturing and Measurements

In this paper, measurement results and manufacturing techniques of three smooth-walled spline horns at frequencies 183-874 GHz are presented. A design example of a broadband spline horn at 120 GHz is also given.

For this paper, I contributed with the design and simulations of the 120 GHz spline horn, construction and coding for the test setup for radiation pattern measurements, data analysis and writing the paper.

Paper F

Optical Tolerance Analysis of the Multi-Beam Limb Viewing Instrument STEAMR

This paper deals with a mechanical tolerance analysis for the STEAMR instrument. Methods of ray-tracing and physical optics were used to investigate the impact of reflector misalignment, both from a statistical point of view and by means of single element perturbations. Distortions of the 1.6 m $\times$ 0.8 m primary reflector surface were also investigated. A demonstrator representing a full-sized sub-system of the optical chain was manufactured and measured mechanically. The results from these measurements were input into the software used for simulation to confirm that the manufacturing methods were accurate enough.

My contributions included setting up optical models in two separate software programs, running simulations, compiling and analyzing the simulation data and writing the article.

Acknowledgements

It is 10.30 p.m. on March 9th, 2019 according to the Gregorian calendar and I am about to finish this thesis. Thinking back on my time as an industrial PhD student at Omnisys and Chalmers, I realize that I have crossed paths with many good people before getting to this point. This is where some of these people are acknowledged.

First, I would like to thank Jan Stake and Anders Emrich who initiated this PhD project and who have been my supervisors since the beginning. Thank you for your support and for the many discussions we have had over the years.

I am very grateful to Soojong Pak and his group at Kyung Hee University for the fruitful collaboration we have had in the MATS project. It was a great experience to visit you in Suwon and I hope to have the opportunity to come back. I am equally grateful to Seunghyuk Chang for his invaluable help with the telescope design. My fellow PhD student Woojin Park also deserves a big thanks for his hard work and many contributions. It was fun to work together in the lab and discuss all possible (and impossible) problems that we encountered.

Many colleagues have helped with big and small things throughout the years and made sure to create an enjoyable work environment. First, a medal of honor goes to Peter Sobis for always being the most supportive since day one. Do not despair – that moose dinner is on its way. Thank you Terese Ekebrand for always helping out and for turning the MATS project in the right direction during your time as a project leader. A big thanks goes to the other members (past and present) of the hard-working MATS team: Jordan Rouse, Mikael Krus, Anders Hörsell, Steven McCallion, David Stomilovic and Jesper Bank. How many engineers does it take to build a complete satellite payload? Apparently not that many.

My gratitude also goes to Sergey Cherednichenko and Vladimir Drakinskiy, who introduced me to the field of THz technology when I worked towards my MSc degree and who have been helpful ever since. In the early years of my studies, I worked with Mark Whale, Yogesh Karandikar and Per Forsberg, who generously shared their knowledge on reflector optics, horn antennas, mechanical engineering and other topics. I also want to thank my friends Johanna Hanning, Robin Dahlbäck, Erik Ryman, Daniel Nyberg, William Hallberg, Oscar Tropp and Fredrik Kjörk for making sure that coming to work was fun.

During the MATS project, I have had the privilege to work directly with some of the researchers at Stockholm University and Chalmers, who will be the end users of the instrument. Thank you Ole Martin Christensen, Donal Murtagh, Linda Megner, Jacek Stegman and Jörg Gumbel for a good collaboration.

Finally, I want to thank my girlfriend Nicole, my family and friends for all your support.

References

[1] J. M. Wallace and P. V. Hobbs, *Atmospheric science: an introductory survey*. Elsevier, 2006, vol. 92.

[2] E. Chuvieco, *Earth observation of global change: The role of satellite remote sensing in monitoring the global environment*. Springer, 2008.

[3] D. Solimini, *Understanding Earth Observation*. Springer, 2016.

[4] R. Sandau, H.-P. Röser, and A. Valenzuela, *Small Satellites for Earth Observation: Selected Contributions*. Springer Science & Business Media, 2008.

[5] "Satellite monitoring of atmospheric composition," http://kejian1.cmatc.cn/vod/comet/EUMETSAT/atmos_comp/print.htm, Accessed 11th March 2019.

[6] M. Drusch, U. D. Bello, S. Carlier, O. Colin, V. Fernandez, F. Gascon, B. Hoersch, C. Isola, P. Laberinti, P. Martimort, A. Meygret, F. Spoto, O. Sy, F. Marchese, and P. Bargellini, "Sentinel-2: ESA's Optical High-Resolution Mission for GMES Operational Services," *Remote Sensing of Environment*, vol. 120, pp. 25 – 36, 2012, the Sentinel Missions - New Opportunities for Science. [Online]. Available: http://www.sciencedirect.com/science/article/pii/S0034425712000636

[7] W. Dierckx, S. Sterckx, I. Benhadj, S. Livens, G. Duhoux, T. V. Achteren, M. Francois, K. Mellab, and G. Saint, "PROBA-V mission for global vegetation monitoring: standard products and image quality," *International Journal of Remote Sensing*, vol. 35, no. 7, pp. 2589–2614, 2014. [Online]. Available: 10.1080/01431161.2014.883097

[8] R. M. D. Thomas S. Pagano, "Moderate Resolution Imaging Spectroradiometer (MODIS)," *Proc. SPIE*, vol. 1939, pp. 1939 – 1939 – 16, 1993. [Online]. Available: 10.1117/12.152835

[9] G. Dial, H. Bowen, F. Gerlach, J. Grodecki, and R. Oleszczuk, "Ikonos satellite, imagery, and products," *Remote Sensing of Environment*, vol. 88, no. 1, pp. 23 – 36, 2003, iKONOS Fine Spatial Resolution Land Observation. [Online]. Available: http://www.sciencedirect.com/science/article/pii/S0034425703002293

[10] F. Volpe and L. Rossi, "QuickBird high resolution satellite data for urban applications," in *Remote Sensing and Data Fusion over Urban Areas, 2003. 2nd GRSS/ISPRS Joint Workshop on*. IEEE, 2003, pp. 1–3.

[11] O. M. Christensen, P. Eriksson, J. Urban, D. Murtagh, K. Hultgren, and J. Gumbel, "Tomographic retrieval of water vapour and temperature around polar mesospheric clouds using Odin-SMR," *Atmospheric Measurement Techniques*, vol. 8, no. 5, pp. 1981–1999, 2015. [Online]. Available: https://www.atmos-meas-tech.net/8/1981/2015/

[12] P. H. Siegel, "Terahertz technology," *IEEE Transactions on microwave theory and techniques*, vol. 50, no. 3, pp. 910–928, 2002.

[13] J. W. Waters, W. G. Read, L. Froidevaux, R. Jarnot, R. Cofield, D. Flower, G. Lau, H. Pickett, M. Santee, D. Wu *et al.*, "The UARS and EOS microwave limb sounder (MLS) experiments," *Journal of the Atmospheric Sciences*, vol. 56, no. 2, pp. 194–218, 1999.

[14] F. Barath, M. Chavez, R. Cofield, D. Flower, M. Frerking, M. Gram, W. Harris, J. Holden, R. Jarnot, W. Kloezeman *et al.*, "The upper atmosphere research satellite microwave limb sounder instrument," *Journal of Geophysical Research: Atmospheres*, vol. 98, no. D6, pp. 10 751–10 762, 1993.

[15] C. L. Croskey, N. Kampfer, R. M. Belivacqua, G. K. Hartmann, K. F. Kunzi, P. R. Schwartz, J. J. Olivero, S. E. Puliafito, C. Aellig, G. Umlauft *et al.*, "The Millimeter Wave Atmospheric Sounder (MAS): A shuttle-based remote sensing experiment," *IEEE Transactions on microwave theory and techniques*, vol. 40, no. 6, pp. 1090–1100, 1992.

[16] G. L. Stephens, D. G. Vane, R. J. Boain, G. G. Mace, K. Sassen, Z. Wang, A. J. Illingworth, E. J. O'connor, W. B. Rossow, S. L. Durden *et al.*, "The CloudSat mission and the A-Train: A new dimension of space-based observations of clouds and precipitation," *Bulletin of the American Meteorological Society*, vol. 83, no. 12, pp. 1771–1790, 2002.

[17] Wikipedia, "Electromagnetic spectrum," *Online: https://en.wikipedia.org/wiki/Electromagnetic_spectrum*, Accessed: 11th March 2019.

[18] A. Wootten and A. R. Thompson, "The Atacama large millimeter/submillimeter array," *Proceedings of the IEEE*, vol. 97, no. 8, pp. 1463–1471, 2009.

[19] B. Lambrigtsen, W. Wilson, A. Tanner, T. Gaier, C. Ruf, and J. Piepmeier, "GeoSTAR-a microwave sounder for geostationary satellites," *Geoscience and Remote Sensing Symposium, 2004. IGARSS'04. Proceedings. 2004 IEEE International*, vol. 2, pp. 777–780, 2004.

[20] A. Emrich, J. Embretsén, K. Kempe, E. Ryman, and P. de Maagt, "54 and 183 GHz Interferometer in Geosynchronous Orbit," in *5th Workshop on Advanced RF Sensors and Remote Sensing Instruments (ARSI)*, 2017.

[21] B. G. Grant, "Field Guide to Radiometry." SPIE, 2011.

[22] S. Chandrasekhar, *Radiative transfer*. Courier Corporation, 2013.

[23] Y. Yang, A. Shutler, and D. Grischkowsky, "Measurement of the transmission of the atmosphere from 0.2 to 2 THz," *Optics express*, vol. 19, no. 9, pp. 8830–8838, 2011.

[24] J. E. Greivenkamp, *Field guide to geometrical optics*. SPIE Press Bellingham, WA, 2004, vol. 1.

[25] C. A. Balanis, *Antenna theory: analysis and design*. Wiley, 2005.

[26] M. Naftaly and R. Dudley, "Terahertz reflectivities of metal-coated mirrors," *Applied optics*, vol. 50, no. 19, pp. 3201–3204, 2011.

[27] J. C. Stover, *Optical scattering: measurement and analysis*. SPIE optical engineering press Bellingham, 1995, vol. 2.

[28] R. N. Pfisterer, "Approximated scatter models for stray light analysis," *Optics & Photonics News*, vol. 22, no. 10, pp. 16–17, 2011.

[29] D. A. Kerr, "Derivation of the cosine fourth law for falloff of illuminance across a camera image," 2007.

[30] B. P. Breault, *Handbook of Optics*. New York: McGraw-Hill, 1995.

[31] S. Cherednichenko, V. Drakinskiy, T. Berg, P. Khosropanah, and E. Kollberg, "Hot-electron bolometer terahertz mixers for the Herschel Space Observatory," *Review of scientific instruments*, vol. 79, no. 3, p. 034501, 2008.

[32] P.-S. Kildal, *Foundations of antenna engineering: a unified approach for line-of-sight and multipath*. Artech House, 2015.

[33] P. D. Potter, "A new horn antenna with suppressed sidelobes and equal beam widths," *Microwave journal*, vol. 6, no. 6, pp. 71–78, 1961.

[34] J. F. Johansson, "A comparison of some feed types," *Multi-Feed Systems for Radio Telescopes*, vol. 75, pp. 82–89, 1995.

[35] P. Kittara, A. Jiralucksanawong, G. Yassin, S. Wangsuya, and J. Leech, "The design of potter horns for THz applications using a genetic algorithm," *International Journal of Infrared and Millimeter Waves*, vol. 28, no. 12, pp. 1103–1114, 2007.

[36] K. K. Davis, J. L. Kloosterman, C. Groppi, J. H. Kawamura, and M. Underhill, "Micromachined Integrated Waveguide Transformers in THz Pickett–Potter Feedhorn Blocks," *IEEE Transactions on Terahertz Science and Technology*, vol. 7, no. 6, pp. 649–656, 2017.

[37] M. Matsunaga, Y. Sekimoto, T. Matsunaga, and T. Sakai, "An experimental study of submillimeter-wave horn antennae for a submillimeter-wave array," *Publications of the Astronomical Society of Japan*, vol. 55, no. 5, pp. 1051–1057, 2003.

[38] P. Goldsmith, *Quasioptical Systems: Gaussian Beam Quasioptical Propogation and Applications*, ser. IEEE Press Series on RF and Microwave Technology. Wiley, 1998.

[39] C. Granet, G. L. James, R. Bolton, and G. Moorey, "A smooth-walled spline-profile horn as an alternative to the corrugated horn for wide band millimeter-wave applications," *IEEE Transactions on Antennas and Propagation*, vol. 52, no. 3, pp. 848–854, 2004.

[40] W. S. Boyle and G. E. Smith, "Charge coupled semiconductor devices," *Bell System Technical Journal*, vol. 49, no. 4, pp. 587–593, 1970.

[41] S. Mendis, S. E. Kemeny, and E. R. Fossum, "CMOS active pixel image sensor," *IEEE Transactions on Electron Devices*, vol. 41, no. 3, pp. 452–453, 1994.

[42] T. Mimura, "The early history of the high electron mobility transistor (HEMT)," *IEEE Transactions on microwave theory and techniques*, vol. 50, no. 3, pp. 780–782, 2002.

[43] R. E. Collin, *Foundations for microwave engineering*. John Wiley & Sons, 2007.

[44] G. P. Williams, "Filling the THz gap-high power sources and applications," *Reports on Progress in Physics*, vol. 69, no. 2, p. 301, 2005.

[45] A. Siegman, "The antenna properties of optical heterodyne receivers," *Applied optics*, vol. 5, no. 10, pp. 1588–1594, 1966.

[46] P. Lehikoinen, J. Mallat, P. Piironen, A. Lehto, J. Tuovinene, and A. V. Räisänen, "A 119 GHz planar Schottky diode mixer for a space application," *International journal of infrared and millimeter waves*, vol. 17, no. 5, pp. 807–818, 1996.

[47] P. H. Siegel, R. Dengler, I. Mehdi, W. Bishop, and T. Crowe, "A 200 GHz planar diode subharmonically pumped waveguide mixer with state-of-the-art performance," in *1992 IEEE MTT-S Microwave Symposium Digest*. IEEE, 1992, pp. 595–598.

[48] W. Y. Ali-Ahmad, W. L. Bishop, T. W. Crowe, and G. M. Rebeiz, "A 250 GHz planar low noise Schottky receiver," *International journal of infrared and millimeter waves*, vol. 14, no. 4, pp. 737–748, 1993.

[49] J. L. Hesler, K. Hui, S. He, and T. W. Crowe, "A fixed-tuned 400 GHz subharmonic mixer using planar Schottky diodes," *Tenth International Symposium on Space Terahertz Technology*, pp. 95–99, 1999.

[50] B. Thomas, A. Maestrini, and G. Beaudin, "A low-noise fixed-tuned 300-360-GHz sub-harmonic mixer using planar Schottky diodes," *IEEE Microwave and Wireless Components Letters*, vol. 15, no. 12, pp. 865–867, 2005.

[51] K. Hui, J. L. Hesler, D. S. Kurtz, W. L. Bishop, and T. W. Crowe, "A micromachined 585 GHz Schottky mixer," *IEEE Microwave and Guided Wave Letters*, vol. 10, no. 9, pp. 374–376, 2000.

[52] W. L. Bishop, K. Mckinney, R. J. Mattauch, T. W. Crowe, and G. Green, "A novel whiskerless Schottky diode for millimeter and submillimeter wave application," *1987 IEEE MTT-S International Microwave Symposium Digest*, vol. 2, pp. 607–610, 1975.

[53] S. D. Vogel, "Design and measurements of a novel subharmonically pumped millimeter-wave mixer using two single planar Schottky-barrier diodes," *IEEE Transactions on microwave theory and techniques*, vol. 44, no. 6, pp. 825–831, 1996.

[54] P. J. Sobis, A. Emrich, and J. Stake, "A low VSWR 2SB schottky receiver," *IEEE Transactions on Terahertz Science and Technology*, vol. 1, no. 2, pp. 403–411, 2011.

[55] H. Zhao, V. Drakinskiy, P. Sobis, J. Hanning, T. Bryllert, A.-Y. Tang, and J. Stake, "Development of a 557 GHz GaAs monolithic membrane-diode mixer," *2012 International Conference on Indium Phosphide and Related Materials*, pp. 102–105, 2012.

[56] P. Sobis, V. Drakinskiy, N. Wadefalk, Y. Karandikhar, A. Hammar, A. Emrich, H. Zhao, T. Bryllert, A.-Y. Tang, P. Nilsson *et al.*, "Low noise GaAs Schottky TMIC and InP Hemt MMIC based receivers for the ISMAR and SWI instruments," *Proc. ESAESTEC Micro-and Millimetre Wave Technol. Techn. Workshop*, pp. 25–27, 2014.

[57] B. Billade, O. Nystrom, D. Meledin, E. Sundin, I. Lapkin, M. Fredrixon, V. Desmaris, H. Rashid, M. Strandberg, S.-E. Ferm *et al.*, "Performance of the first ALMA band 5 production cartridge," *IEEE Transactions on Terahertz Science and Technology*, vol. 2, no. 2, pp. 208–214, 2012.

[58] S. Mahieu, D. Maier, B. Lazareff, A. Navarrini, G. Celestin, J. Chalain, D. Geoffroy, F. Laslaz, and G. Perrin, "The ALMA band-7 cartridge," *IEEE Transactions on Terahertz Science and Technology*, vol. 2, no. 1, pp. 29–39, 2012.

[59] T. Tamura, T. Noguchi, Y. Sekimoto, W. Shan, N. Sato, Y. Iizuka, K. Kumagai, Y. Nizeki, M. Iwakuni, and T. Ito, "Performance and uniformity of mass-produced SIS mixers for ALMA band 8 receiver cartridges," *IEEE Transactions on Applied Superconductivity*, vol. 25, no. 3, pp. 1–5, 2015.

[60] A. Khudchenko, A. M. Baryshev, K. I. Rudakov, P. M. Dmitriev, R. Hesper, L. de Jong, and V. P. Koshelets, "High-gap Nb-AlN-NbN SIS junctions for frequency band 790-950 GHz," *IEEE Transactions on Terahertz Science and Technology*, vol. 6, no. 1, pp. 127–132, 2016.

[61] S. Krause, D. Meledin, V. Desmaris, A. Pavolotsky, H. Rashid, and V. Belitsky, "Noise and IF gain bandwidth of a balanced waveguide NbN/GaN hot electron bolometer mixer operating at 1.3 THz," *IEEE Transactions on Terahertz Science and Technology*, vol. 8, no. 3, pp. 365–371, 2018.

[62] S. Bevilacqua, E. Novoselov, S. Cherednichenko, H. Shibata, and Y. Tokura, "MgB2 Hot-Electron Bolometer Mixers at Terahertz Frequencies," *IEEE Transactions on Applied Superconductivity*, vol. 25, no. 3, pp. 1–4, 2015.

[63] E. Novoselov, S. Bevilacqua, S. Cherednichenko, H. Shibata, and Y. Tokura, "Noise measurements of the low Tc MgB2 HEB mixer at 1.6 THz and 2.6 THz," in *Proc. 26th Int. Symp. Space THz Technol.*, 2015.

[64] S. Cherednichenko, V. Drakinskiy, T. Berg, P. Khosropanah, and E. Kollberg, "Hot-electron bolometer terahertz mixers for the Herschel Space Observatory," *Review of scientific instruments*, vol. 79, no. 3, p. 034501, 2008.

[65] P. Khosropanah, J. Gao, W. Laauwen, M. Hajenius, and T. Klapwijk, "Low noise NbN hot electron bolometer mixer at 4.3 THz," *Applied Physics Letters*, vol. 91, no. 22, p. 221111, 2007.

[66] Y. Irimajiri, A. Kawakami, I. Morohashi, N. Sekine, S. Ochiai, S. Tanaka, I. Hosako, and M. Yasui, "Development of a low noise heterodyne receiver at 3 THz," *2012 37th International Conference on Infrared, Millimeter, and Terahertz Waves*, pp. 1–2, 2012.

[67] K. M. Leong, X. Mei, W. H. Yoshida, A. Zamora, J. G. Padilla, B. S. Gorospe, K. Nguyen, and W. R. Deal, "850 GHz receiver and transmitter front-ends using InP HEMT," *IEEE Transactions on Terahertz Science and Technology*, vol. 7, no. 4, pp. 466–475, 2017.

[68] S. T. Brown, S. Desai, W. Lu, and A. Tanner, "On the long-term stability of microwave radiometers using noise diodes for calibration," *IEEE Transactions on Geoscience and Remote Sensing*, vol. 45, no. 7, pp. 1908–1920, 2007.

[69] M. Kotiranta, K. Jacob, H. Kim, P. Hartogh, and A. Murk, "Optical Design and Analysis of the Submillimeter-Wave Instrument on JUICE," *IEEE Transactions on Terahertz Science and Technology*, vol. 8, no. 6, pp. 588–595, 2018.

[70] H. T. Friis, "Noise figures of radio receivers," *Proceedings of the IRE*, vol. 32, no. 7, pp. 419–422, 1944.

[71] K. M. K. H. Leong, X. Mei, W. H. Yoshida, A. Zamora, J. G. Padilla, B. S. Gorospe, K. Nguyen, and W. R. Deal, "850 ghz receiver and transmitter front-ends using inp hemt," *IEEE Transactions on Terahertz Science and Technology*, vol. 7, no. 4, pp. 466–475, July 2017.

[72] J. L. Hesler and T. W. Crowe, "Responsivity and noise measurements of zero-bias Schottky diode detectors," *Proc. ISSTT*, pp. 89–92, 2007.

[73] A. Boukhayma, *Ultra low noise CMOS image sensors*. Springer, 2017.

[74] J. R. Janesick *et al.*, *Scientific charge-coupled devices*. SPIE press Bellingham, 2001, vol. 117.

[75] HORIBA optics website., *Online: https://www.horiba.com*, Accessed: 11th March 2019.

[76] R. Widenhorn, M. M. Blouke, A. Weber, A. Rest, and E. Bodegom, "Temperature dependence of dark current in a CCD," *Sensors and Camera Systems for Scientific, Industrial, and Digital Photography Applications III*, vol. 4669, pp. 193–202, 2002.

[77] J. Tansock, D. Bancroft, J. Butler, C. Cao, R. Datla, S. Hansen, D. Helder, R. Kacker, H. Latvakoski, M. Mylnczak *et al.*, "Guidelines for radiometric calibration of electro-optical instruments for remote sensing," 2015.

[78] J.-Q. Sun, X. Xiong, and W. L. Barnes, "MODIS solar diffuser stability monitor sun view modeling," *IEEE Transactions on geoscience and remote sensing*, vol. 43, no. 8, pp. 1845–1854, 2005.

[79] J. Gumbel, L. Megner, O. M. Christensen, S. Chang, J. Dillner, T. Ekebrand, G. Giono, A. Hammar, J. Hedin, N. Ivchenko, B. Karlsson, M. Kruse, A. Li, S. McCallion, D. P. Murtagh, G. Olentšenko, S. Pak, W. Park, J. Rouse, J. Stegman, and G. Witt, "The MATS Satellite Mission – Gravity Waves Studies by Mesospheric Airglow/Aerosol Tomography and Spectroscopy," *Atmospheric Chemistry and Physics Discussions*, vol. 2018, pp. 1–41, 2018. [Online]. Available: https://www.atmos-chem-phys-discuss.net/acp-2018-1162/

[80] A. Einstein and N. Rosen, "On gravitational waves," *Journal of the Franklin Institute*, vol. 223, no. 1, pp. 43–54, 1937.

[81] D. C. Fritts and M. J. Alexander, "Gravity wave dynamics and effects in the middle atmosphere," *Reviews of Geophysics*, vol. 41, no. 1, 2003. [Online]. Available: https://agupubs.onlinelibrary.wiley.com/doi/abs/10.1029/2001RG000106

[82] M. Krebsbach and P. Preusse, "Spectral analysis of gravity wave activity in SABER temperature data," *Geophysical Research Letters*, vol. 34, no. 3, 2007. [Online]. Available: https://agupubs.onlinelibrary.wiley.com/doi/abs/10.1029/2006GL028040

[83] H. Fischer, M. Birk, C. Blom, B. Carli, M. Carlotti, T. von Clarmann, L. Delbouille, A. Dudhia, D. Ehhalt, M. Endemann, J. M. Flaud, R. Gessner, A. Kleinert, R. Koopman, J. Langen, M. López-Puertas, P. Mosner, H. Nett, H. Oelhaf, G. Perron, J. Remedios, M. Ridolfi, G. Stiller, and R. Zander, "MIPAS: an instrument for atmospheric and climate research," *Atmospheric Chemistry and Physics*, vol. 8, no. 8, pp. 2151–2188, 2008. [Online]. Available: https://www.atmos-chem-phys.net/8/2151/2008/

[84] C. von Savigny, C. Robert, H. Bovensmann, J. P. Burrows, and M. Schwartz, "Satellite observations of the quasi 5-day wave in noctilucent clouds and mesopause temperatures," *Geophysical Research Letters*, vol. 34, no. 24, 2007. [Online]. Available: https://agupubs.onlinelibrary.wiley.com/doi/abs/10.1029/2007GL030987

[85] V. Limpasuvan, D. L. Wu, M. J. Schwartz, J. W. Waters, Q. Wu, and T. L. Killeen, "The two-day wave in EOS MLS temperature and wind measurements during 2004-2005 winter," *Geophysical Research Letters*, vol. 32, no. 17, 2005. [Online]. Available: https://agupubs.onlinelibrary.wiley.com/doi/abs/10.1029/2005GL023396

[86] P. Preusse, S. D. Eckermann, and M. Ern, "Transparency of the atmosphere to short horizontal wavelength gravity waves," *Journal of Geophysical Research: Atmospheres*, vol. 113, no. D24, 2008. [Online]. Available: https://agupubs.onlinelibrary.wiley.com/doi/abs/10.1029/2007JD009682

[87] M. Gadsden and W. Schröder, "Noctilucent clouds," *Noctilucent Clouds*, pp. 1–12, 1989.

[88] M. G. Mlynczak and D. S. Olander, "On the utility of the molecular oxygen dayglow emissions as proxies for middle atmospheric ozone," *Geophysical research letters*, vol. 22, no. 11, pp. 1377–1380, 1995.

[89] N. Larsson, R. Lilja, M. Örth, S. Söderholm, J. Köhler, R. Lindberg, and J. Gumbel, "InnoSat and MATS–An Ingenious Spacecraft Platform applied to Mesospheric Tomography and Spectroscopy," in *10th IAA Symposium for Earth Observation*, 2015, Accessed 11th March 2019. [Online]. Available: https://www.dlr.de/iaa.symp/Portaldata/49/Resources/dokumente/archiv10/pdf/1002.pdf

[90] S. Fox, C. Lee, B. Moyna, M. Philipp, I. Rule, S. Rogers, R. King, M. Oldfield, S. Rea, M. Henry *et al.*, "ISMAR: an airborne submillimetre radiometer," *Atmospheric Measurement Techniques*, vol. 10, no. 2, pp. 477–490, 2017.

[91] S. Fox, C. Lee, I. Rule, R. King, S. Rogers, C. Harlow, and A. Baran, "ISMAR: A new submillimeter airborne radiometer," *Microwave Radiometry and Remote Sensing of the Environment (MicroRad), 2014 13th Specialist Meeting on*, pp. 128–132, 2014.

[92] M. Bergadá, M. Labriola, R. González, M. Palacios, D. Marote, A. Andrés, J. García, D. Sánchez-Pascuala, L. Ordóñez, M. Rodríguez *et al.*, "The Ice Cloud Imager (ICI) preliminary design and performance," *Microwave Radiometry and Remote Sensing of the Environment (MicroRad), 2016 14th Specialist Meeting on*, pp. 27–31, 2016.

[93] D. Murtagh, U. Frisk, F. Merino, M. Ridal, A. Jonsson, J. Stegman, G. Witt, P. Eriksson, C. Jiménez, G. Megie *et al.*, "An overview of the Odin atmospheric mission," *Canadian Journal of Physics*, vol. 80, no. 4, pp. 309–319, 2002.

[94] V. Kangas, S. D'Addio, M. Betto, H. Barre, M. Loiselet, and G. Mason, "Metop Second Generation microwave sounding and microwave imaging missions," in *2012 EUMETSAT Meteorological Satellite Conference*, 2012, pp. 3–7.

[95] B. Carnicero Dominguez *et al.*, "ESA's PREMIER mission candidate: System and payload overview," *Geoscience and Remote Sensing Symposium (IGARSS), 2012 IEEE International*, pp. 5538–5541, 2012.

[96] "Earth explorers - an overview," http://www.esa.int/Our_Activities/Observing_the_Earth/Earth_Explorers_an_overview, Accessed 11th March 2019.

[97] C. Sioris, T. Piekutowski, C. Nilsson, D. Degenstein, D. Murtagh, B. Solheim, F. von Schéele, C. McLinden, Y. J. Rochon, G. Deblonde *et al.*, "THE ATMOSPHERIC

LIMB SOUNDING SATELLITE (ALISS)," in *G65th International Astronautical Congress 2014*, 2014.

[98] M. Whale, A. Murphy, A. Murk, M. Renker, U. Frisk, and O. Janson, "A Compensating Anastigmatic Submillimeter Array Imaging System for STEAMR," *IEEE Transactions on Terahertz Science and Technology*, vol. 3, no. 1, pp. 110–119, 2013.

[99] M. Whale, M. Renker, A. Murk, U. Frisk, O. Janson, L. Blecha, G. Paciotti, G. Bell, R. Wylde, and A. Muprhy, "The STEAMR instrument: Optical design, development and testing," *Proceedings, 23rd International Symposium on Space Terahertz Technology*, pp. 89–92, 2012.

[100] M. Renker, M. Whale, and A. Murk, "Antenna Simulations and Measurements of Focal Plane Array Facet Reflectors," *IEEE Transactions on Antennas and Propagation*, vol. 61, no. 4, pp. 1722–1732, 2013.

[101] M. Renker, "The Stratosphere-Troposphere Exchange And Climate Monitor Radiometer (STEAMR): Optical Design, Radiometric Tests and First Atmospheric Observations," PhD thesis, 2014.

[102] S. Menon, K. L. Denman, G. Brasseur, A. Chidthaisong, P. Ciais, P. M. Cox, R. E. Dickinson, D. Hauglustaine, C. Heinze, E. Holland *et al.*, "Couplings between changes in the climate system and biogeochemistry," Lawrence Berkeley National Lab.(LBNL), Berkeley, CA (United States), Tech. Rep., 2007.

[103] M. Born and E. Wolf, *Principles of Optics*, 7th ed. Cambridge University Press, 1999.

[104] Zemax, OpticStudio, *Online: https://www.zemax.com/products/opticstudio*, Accessed: 11th March 2019.

[105] D. J. Schroeder, *Astronomical optics*. Elsevier, 1999.

[106] R. E. Fischer, B. Tadic-Galeb, P. R. Yoder, R. Galeb, B. C. Kress, S. C. McClain, T. Baur, R. Plympton, B. Wiederhold, and B. G. A. J, *Optical system design*. Citeseer, 2000.

[107] S. Chang and A. Prata, "Geometrical theory of aberrations near the axis in classical off-axis reflecting telescopes," *JOSA A*, vol. 22, no. 11, pp. 2454–2464, 2005.

[108] S. Chang, J. H. Lee, S. P. Kim, H. Kim, W. J. Kim, I. Song, and Y. Park, "Linear astigmatism of confocal off-axis reflective imaging systems and its elimination," *Applied optics*, vol. 45, no. 3, pp. 484–488, 2006.

[109] Surrey Nanosystems, Vantablack S-VIS, *Online: https://www.surreynanosystems.com/super-black-coatings/vantablack-s-vis*, Accessed: 11th March 2019.

[110] A. Bondeson, T. Rylander, and P. Ingelstrom, *Computational electromagnetics*. New York; London: Springer, 2012, vol. 51; 51.

[111] E. Brundermann, H.-W. Hubers, and M. F. Kimmitt, "Terahertz techniques," vol. 151, 2012.

[112] Y. B. Karandikar, *Integration of Planar Antennas with MMIC Active Frontends for THz Imaging Applications*. Chalmers University of Technology, 2012.

[113] J. Tuovinen, "Accuracy of a gaussian beam," *IEEE Transactions on antennas and propagation*, vol. 40, no. 4, pp. 391–398, 1992.

[114] A. Gonzalez, "Frequency independent design of quasi-optical systems," *Journal of Infrared, Millimeter, and Terahertz Waves*, vol. 37, no. 2, pp. 147–159, 2016.

[115] M. Whale, A. Murphy, A. Murk, M. Renker, U. Frisk, and O. Janson, "A compensating anastigmatic submillimeter array imaging system for STEAMR," *IEEE Transactions on terahertz science and technology*, vol. 3, no. 1, pp. 110–119, 2013.

[116] TICRA, GRASP Version 10.0.1, *Online: http://www.ticra.com*, Accessed: 11th March 2019.

[117] K. Pontoppidan. GRASP, technical description. Copenhagen; Denmark.

[118] A. D. Olver and P. J. Clarricoats, *Microwave horns and feeds*. IET, 1994, vol. 39.

[119] M. E. Mortenson, *Mathematics for computer graphics applications*. Industrial Press Inc., 1999.

[120] SMT Consultancies Ltd., CORRUG Version 3.3.5, *Online: http://www.smtconsultancies.co.uk/products/corrug/corrug.php*, Accessed: 11th March 2019.

[121] Teledyne e2v, CCD42-10 datasheet, *Online: http://www.e2v.com/resources/account/download-datasheet/3747*, Accessed: 11th March 2019.

[122] C. Aviado, J. Gill, K. Redman, and R. Ohl, "Methods for correlating autocollimation of theodolites and coordinate metrology in spacecraft systems," *Optomechanical Technologies for Astronomy*, vol. 6273, p. 62733H, 2006.

[123] G. D. Boreman, *Modulation transfer function in optical and electro-optical systems*. SPIE press Bellingham, WA, 2001, vol. 21.

[124] E. P. Goodwin and J. C. Wyant, "Field guide to interferometric optical testing." SPIE Bellingham, WA, 2006.

[125] J. M. Geary, *Introduction to optical testing*. SPIE Press, 1993, vol. 15.

[126] D. Malacara, *Optical shop testing*. John Wiley & Sons, 2007.

[127] J. A. Anderson and R. W. Porter, "Ronchi's method of optical testing," *The Astrophysical Journal*, vol. 70, p. 175, 1929.

[128] J. L. Marshall, P. Williams, J.-P. Rheault, T. Prochaska, R. D. Allen, and D. DePoy, "Characterization of the reflectivity of various black materials," *Ground-based and Airborne Instrumentation for Astronomy V*, vol. 9147, p. 91474F, 2014.

[129] A. Gonzalez and Y. Uzawa, "Tolerance Analysis of ALMA Band 10 Corrugated Horns and Optics," *IEEE Transactions on Antennas and Propagation*, vol. 60, no. 7, pp. 3137–3145, July 2012.

[130] E. De Rijk, A. Macor, J.-P. Hogge, S. Alberti, and J.-P. Ansermet, "Note: Stacked rings for terahertz wave-guiding," *Review of Scientific Instruments*, vol. 82, no. 6, p. 066102, 2011.

[131] J. Leech, B. Tan, G. Yassin, P. Kittara, S. Wangsuya, J. Treuttel, M. Henry, M. Oldfield, and P. Huggard, "Multiple flare-angle horn feeds for sub-mm astronomy and cosmic microwave background experiments," *Astronomy & Astrophysics*, vol. 532, p. A61, 2011.

[132] C. Groppi, C. Walker, C. Kulesa, D. Golish, J. Kloosterman, S. Weinreb, G. Jones, J. Bardin, H. Mani, T. Kuiper *et al.*, "Test and integration results from SuperCam: a 64-pixel array receiver for the 350 GHz atmospheric window," *Millimeter, Submillimeter, and Far-Infrared Detectors and Instrumentation for Astronomy V*, vol. 7741, p. 77410X, 2010.

[133] R. C. Johnson, H. A. Ecker, and J. S. Hollis, "Determination of far-field antenna patterns from near-field measurements," *Proceedings of the IEEE*, vol. 61, no. 12, pp. 1668–1694, 1973.

[134] A. Olver, "Compact antenna test ranges," *1991 Seventh International Conference on Antennas and Propagation, ICAP 91 (IEE)*, pp. 99–108, 1991.

[135] T. Hirvonen, J. Ala-Laurinaho, J. Tuovinen, and A. Raisanen, "A compact antenna test range based on a hologram," *IEEE Transactions on Antennas and Propagation*, vol. 45, no. 8, pp. 1270–1276, Aug 1997.

[136] J. Ala-Laurinaho, T. Hirvonen, P. Piironen, A. Lehto, J. Tuovinen, A. Raisanen, and U. Frisk, "Measurement of the Odin telescope at 119 GHz with a hologram-type CATR," *IEEE Transactions on Antennas and Propagation*, vol. 49, no. 9, pp. 1264–1270, Sep 2001.

[137] A. Karttunen, J. Ala-Laurinaho, M. Vaaja, T. Koskinen, J. Hakli, A. Lonnqvist, J. Mallat, A. Tamminen, V. Viikari, and A. Raisanen, "Antenna Tests With a Hologram-Based CATR at 650 GHz," *IEEE Transactions on Antennas and Propagation*, vol. 57, no. 3, pp. 711–720, March 2009.

[138] K. K. Davis, S. J. Yates, W. Jellema, C. E. Groppi, J. J. Baselmans, K. Kohno, and A. M. Baryshev, "Complex Field Mapping of Large Direct Detector Focal Plane Arrays," *IEEE Transactions on Terahertz Science and Technology*, vol. 9, no. 1, pp. 67–77, 2019.

[139] J. Säily and A. V. Räisänen, "Characterization of submillimeter wave absorbers from 200–600 GHz," *International Journal of Infrared and Millimeter Waves*, vol. 25, no. 1, pp. 71–88, 2004.

[140] A. Emrich, S. Andersson, M. Wannerbratt, P. Sobis, S. Cherednichenko, D. Runesson, T. Ekebrand, M. Krus, C. Tegnader, and U. Krus, "Water vapor radiometer for ALMA," *Twentieth International Symposium on Space Terahertz Technology*, pp. 174–177, 2009.

[141] P. Yagoubov, A. Murk, R. Wylde, G. Bell, and G. Tan, "Calibration loads for ALMA," *2011 International Conference on Infrared, Millimeter, and Terahertz Waves*, pp. 1–2, 2011.